THERMAL PERFORMANCE OF DOUBLE-SKIN FAÇADE WITH THERMAL MASS

Ali Fallahi

A Thesis

in

The department

of

Building, Civil and Environmental Engineering

Presented in Partial Fulfillment of the Requirements for the

Degree of Doctor of Philosophy (Building Engineering)

at

Concordia University

Montreal, Quebec, Canada

June 2009

Your file Votre référence
ISBN: 978-0-494-63349-6
Our file Notre référence
ISBN: 978-0-494-63349-6

ABSTRACT

Thermal Performance of Double-Skin Façade with Thermal Mass

Ali Fallahi, Ph.D.
Concordia University, 2009

In order to mitigate the overheating problem in the warmer seasons, and thereby to improve thermal performance and energy efficiency of the Double-Skin Façade (DSF) system, this study introduced an innovative design approach involving the integration of thermal mass with the air channel of the conventional DSF. Then it proposed a numerical procedure to assess the thermal performance of DSF, and finally investigated the effect of thermal mass on the energy efficiency of such system.

The initial step in the assessment procedure proposed the development of base-case models, which were able to predict temperature distribution in the DSF with a venetian blind. So too were the base-case models able to determine heating/cooling loads of the perimeter room for both the mechanically and naturally ventilated DSFs. In this procedure, building energy simulation software was used for base-case development; two distinct models were generated: an airflow model and a thermal model. The nodal, uni-directional airflow network method was applied in the case of the naturally ventilated DSF. The thermal model was a transient control volume method which found temperature distribution in discretized air-channel.

The base-cases were verified at two levels: inter-model verification and verification relying on measurements from mechanically and naturally ventilated outdoor test-cells. At both levels, a generally fair agreement was obtained. After this, parametric studies pertaining to the energy performance of the system were conducted on the effect of thermal mass in unison with different air-channel configurations.

Considerable energy load reductions were found when thermal mass was used in the air-channel, replacing venetian blind slats for mechanically ventilated DSFs; this held true during both summer and winter. In this configuration depending on the airflow path direction, energy savings from 21% to 26% in summer and from 41% to 59% in winter are achievable in compared with conventional DSF with aluminum venetian blind. The savings were found higher in sunny days than cloudy days. On the other hand, naturally ventilated DSFs combined with thermal mass were not found to be energy efficient in winter due to stack effect and airflow rate increase within the air channel.

ACKNOWLEDGEMENTS

I would like to extend my gratitude to my supervisor Professor Haghighat whose wisdom and advice was always constructive and forthcoming. Without the help of him it may not be possible for me to finish my research work.

I am indebted to my co-supervisor, Dr. El-Sadi, first and foremost for creating an environment in which I was encouraged coming to work and her guidance; the last two years.

I would also like to extend my gratitude to Prof. Athenities who I relied on for numerous guidance, encouragement and inspiration over the past few years.

I also wish to thank Prof. Perino and my friend Nicolas Artmann for providing me with the experimental data of ventilated double-skin façade. I also thank Prof. De Silvia and his research group for their hospitality they exhibited during my stay in Portugal for ANNEX 44 meeting.

Moreover, my thanks go to all my friends and fellow students in our research group for their unreserved cooperation. I frankly appreciate their genuine friendship, generous support and constant help.

I am also grateful to all parties that have been afforded to me throughout my graduate degree at Concordia University.

Finally, I wish to express my appreciation to all my family members for their support, patience and understanding.

TABLE OF CONTENTS

LIST OF FIGURES

LIST OF TABLES

LIST OF SYMBOLS

Roman Symbols

ach	air change rate [1/hr]
a′, a″	first and second absorption [W/m^2]
C_a	specific heat capacity of air [J/(kg.K)]
d	thickness [m]
d_o	terrain displacement length [m]
f	slat thickness correction factor [-]
g	gravitational acceleration [m/s^2]
h_c	convection coefficient [W/(m^2.K)]
m	mass flow rate [m^3/s]
p	pressure [Pa]
q_c	convection heat transfer [W]
q_v	advection heat transfer [W]
q_L	long-wave energy exchange [W]
q_r	causal heat gain [W]
q_I	internal heat generation [W]
q_s	short-wave energy exchange [W]
r_o	equivalent reflectance [-]
r′, r″	first and second absorption [W/m^2]
t	time [hr]
v	velocity [m/s]
v*	atmospheric friction speed [m/s]
v_m	free speed wind speed [m/s]
v_i	wind speed at specific height [m/s]
v_r	wind speed [m/s]
x,y, z	cartesian coordinates [m]
z_o	terrain dependent roughness [m]
A	aspect ratio [-]
A	absorbed radiation fraction [-]
A,B	coefficient matrix for future time-row and present time-row [-]
C	column matrix of known boundary conditions [-]
C_d	discharge coefficient [-]
C_p	surface wind pressure coefficient [-]
D_h	hydraulic diameter [m]
F	view factor [-]
H	height [m]
I	solar radiation [W/m^2]
K	thermal conductivity [W/(m.K)]
L	depth [m]

P	permeability [-]
P	pressure [Pa]
P_s	stack pressure [Pa]
P_w	wind pressure [Pa]
Pa	ambient pressure [Pa]
P_{mech}	pressurization/depressurization due to mechanical systems [Pa]
P_m , P_n	static pressure at nodes m and n [Pa]
P_k	static pressure in front of damper [Pa]
$Q"_i$	transmission gains/losses through interior pane of DSF [W/m^2]
$Q"_o$	transmission gains/losses through exterior pane of DSF [W/m^2]
$Q"_{solar\ trans.}$	short-wave radiation passing directly through interior pane [W/m^2]
$Q"_{solar}$	short-wave radiation incident on exterior pane [W/m^2]
$Q"_{vent\text{-}in}$	enthalpy of supply air [W/m^2]
$\Delta P_{i,a}$	pressure difference across inlet/outlet damper [Pa]
R	thermal resistance [m^2.k/W]
R	reflected radiation fraction [-]
R	absorbed solar radiation [kW]
S	surrounding thermal node [-]
T	temperature [K], [C]
T	transmitted radiation fraction [-]
T_m	cross-section averaged mean temperature [K], [C]
T*	dimensionless temperature [-]
T_{gap}	gap temperature [C]
$T_{inner\ glazing}$	inner glazing temperature [C]
T_{bld}	blind temperature [C]
$T_{outer\ glazing}$	outer glazing temperature [C]
T_{inlet}	inlet temperature [C]
T_{room}	room temperature [C]
V	volume [m^3]
V*	atmospheric friction speed [m/s]
X	hydraulic entrance length [m]
X_T	thermal entrance length [m]
Z	height above around [m]
Z_m , Z_n	local reference height[m]

Dimensionless numbers

Gr	Grashof number [-]
Nu	Nusselt number [-]
Pr	Prandtl number [-]
Ra	Rayleigh number [-]

Greek symbols

α	absorption coefficient [-]
α	thermal diffusivity [m^2/s]
β	coefficient of volumetric thermal expansion [1/k]
β	sun altitude [deg]
ε	emissivity [-]
μ	dynamic viscosity [s.Pa]
ν	kinematic viscosity [m^2/s]
φ	tilt angle [deg]
ρ	reflection coefficient [-]
ρ	density [kg/m^3]
ρ_m , ρ_n	air density [kg/m^3]
τ	transmission coefficient [-]

Subscripts

a	air
ae	exterior cavity air
ai	interior cavity air
av	average
bl	laminar boundary layer
buoy	buoyancy
con	convection
ct	conduction
cr	critical
D	direct solar radiation
D	diameter of cylinder
d	diffuse solar radiation
db	drybulb
dp	dewpoint
e	exterior
for	forced
fd	fully developed
g	glazing
H	height of air channel
L	depth of air channel
LW	long-wave radiation
na	natural
s	surface
sky	sky
sur	surrounding
SW	short –wave radiation
x	local

∞	free stream

Superscriptsct

ct	conduction
l	laminar flow
t	turbulent

Abbreviations

AL	aluminum thermal mass
EA	exhaust air DSF
IAC	indoor air circulation DSF
OAC	outdoor air circulation DSF
TM	concrete thermal mass replacing venetian blind of DSF
TMi	concrete thermal mass replacing inner skin of DSF
TMo	concrete thermal mass replacing outer skin of DSF
SA	supply air DSF

CHAPTER 1
INTRODUCTION

1.1 Background

Highly glazed façades are one of the indispensable features of many modern buildings. Before the energy crisis of 1973, the use of highly glazed façades was concentrated on their aesthetical purposes without any concern about their thermal performance or energy conservation. Since energy was cheap and available, there was no real policy to apply glass so that it was responsive to environment; the inefficiency of fully glazed buildings, with large heat gains in summer and heat losses in winter, could be compensated by increased operation of the air-conditioning system (Allard et al., 1998).

After oil crisis of 1973, the inefficiency of fully glazed buildings was criticized, leading the building industry to develop new products such as photosensitive and photo-chromic glass, and new glass coatings such as reflective or selective (Low-E), anti-reflection, ceramic-enamel, and angular selective. Many of these new technologies have helped reduce energy consumption in buildings with large glass areas (Li, 2001).

Although many of these technologies have the potential to save energy, additional reductions may be possible for the fully glazed building. With this in mind, the DSF is

used frequently in Europe and North America. The main purpose of the double glass envelope is to balance the desire for daylight and outdoor view with the concerns for hat gain and loss. The air cavity can be heated by the sun to create a warm buffer zone that protects interior zones in winter, or can be configured to function as a thermal chimney in summer, utilizing the stack effect to remove excess heat. These systems are reported to be energy efficient, although little scientific evidence is available to support this claim (Li, 2001).

Double-skin façade essentially refers to a pair of glass "skins" separated by an air-corridor. The air space between the two skins acts as insulation against temperature extremes, wind and sound, and also normally contains a shading device, which may be controlled (Boake et al., 2001). The air channel may be ventilated naturally or mechanically.

The double-skin façade takes advantage of the potential of the façade as a major energy saving component to decrease running cost (cooling/heating load) and also to improve the indoor climate of a building. In addition to energy efficiency and indoor climate improvement, its transparent appearance attracts the attention of many designers and developers. Also the DSF system has other potential benefits such as acoustic control, water penetration resistance, and improved office atmosphere because of the view and utilization of daylight.

The double-skin façade has also been classified as an advanced integrated façade, which is a concept representing a dynamic building envelope in contrast to static behavior. The façade is then capable of adapting to changes in outdoor conditions in order to achieve indoor comfort requirements and reduce energy consumption. The advanced integrated façade itself is a part of larger classification called responsive building elements (IEA Annex 44, 2008).

1.2 Problem Statement

The sunspace effect of double-skin façade technology is associated with reduced energy needs for heating during cold weather, and is therefore considered an energy efficient technology. During warmer periods, however, the double-skin façade can cause overheating problems and/or increased energy needs for cooling, especially if the appropriate shading and the ventilation of double-skin façade is not considered at design stage (Marques da Silva et al., 2006). The overheating problem may escalate at higher floors due to higher temperature of the double skin façade (Perino et al., 2007).

1.3 Proposed Objective

In order to mitigate the overheating problem in the cooling season and therefore improve thermal performance and energy efficiency of the system, an innovative concept of integration of thermal mass with an air channel of the DSF was introduced. This integration is to replace conventional aluminum blind or glazing with thermal mass material. In general, the temperature of the blind and glazing is high due to absorbed

solar energy, which is a disadvantage in hot periods and may lead to overheating. Generally, utilizing thermal mass is a very effective way of reducing the wide outdoor temperature fluctuations and keeping the indoor temperature variation within a narrow comfortable range (Asan and Sancaktar, 1998). Therefore, this integration could be able to effectively reduce peak temperatures inside the air channel and lead to a heating load reduction, even in the heating season. It is believed that this integration not only provides all the advantages of the conventional DSF façade but also suggests potentials in thermal comfort and energy efficiency improvements.

The proposed thermal mass acts as a thermal storage by absorbing solar energy and releasing later, thus contributing to heat recovery and enthalpy gains of the DSF. On the other hand, by reducing heat transmission losses, it is believed that this thermal-mass replaced the blind is capable of decreasing cooling/heating loads and provides greater indoor climate comfort.

Here is a brief comparison of DSF with conventional shading device and DSF with proposed thermal mass and the potential of the latter to improve energy efficiency:

1) *Cooling/Heating load reduction:* In conventional DSF the insulating behavior of the air cavity causes the inner pane to have temperatures closer to those of the indoor air, and as a result a lower heat transfer rate across the inner pane leads to lower heating/cooling load. Installing thermal mass in the air channel means higher thermal storage of the whole façade, and at the

same time the temperature of inner pane becomes much closer to that of the indoors. This leads to additional heating/cooling load reduction.

2) *Peak cooling load delay:* based on the properties of thermal mass, it is able to delay the peak temperature of the inner pane and therefore to delay the peak heating load of perimeter zones. This may be especially useful in office buildings to delay peak loads to unoccupied periods.

3) *Pre-heating air at winter night:* Since thermal mass material is able to absorb solar energy due to its higher thermal storage (compared to conventional blinds) and then releases the absorbed heat over a longer period of time, there would be the possibility to heat up the air in the channel even after sunset in the heating season.

To obtain a comprehensive view of the behavior of thermal mass, a base-case modeling in two parts, airflow and thermal, will be developed for both mechanically and naturally ventilated DSF. These base-case models are able to predict temperature distribution in a DSF with shading device and the heat flux to the room attached to the DSF. In the next step, the base-case will be verified at two levels: inter-model verification and the verification with measurements of mechanically and naturally ventilated outdoor test-cells. Finally parametric studies will be conducted on new base-cases with thermal mass.

The parametric study investigates the effect of influential parameters on energy performance of integrated DSF with thermal mass. These influential parameters include location and thickness of thermal mass, and the direction and type of ventilation in the air channel of DSF.

Furthermore, this study helps to increase the understanding of the phenomena interacting in double-skin façade systems. In this study, thermal mass and its influence on the performance of the DSF system will be analyzed, a case which has been rarely looked at in previous studies of DSF systems. Although few studies have already been done about the effect of thermal mass of interior walls on the performance of the DSF, integration of thermal mass specifically with shading device is a new idea which offers larger surface area for heat transfer inside the air channel and more effective thermal storage and release.

In brief, this study seeks these two main objectives:

1) Propose a procedure to assess thermal performance of DSF. The assessment procedure proposes development of base-case models which are able to predict the temperature profile of DSF with shading device for both mechanically and naturally ventilated DSFs. The development of base-case models can be divided in two parts: airflow and thermal models. The airflow model is capable of estimating the airflow rate of the air channel, and the thermal model is able to determine:
    - Heat transfer rate through the interior and exterior surface of the double-skin façade when the air cavity is ventilated naturally or mechanically,

- The spatial and temporal temperature distribution profile of double-skin façade,
- The heating/cooling load of the adjacent zone to the double-skin façade.

2) To study the effect of thermal mass material (concrete) on the energy efficiency of the DSF system by varying the influential parameters, such as:
    - Configuration of air channel with concrete thermal mass,
    - Thickness of concrete thermal mass,
    - Direction of air flow path,
    - Ventilation type of air channel,
    - Season.

CHAPTER 2

LITERATURE REVIEW

This chapter presents the literature review on modeling of double-skin façade and performance of thermal mass in buildings. Section 2.1 discusses the common type of studies and applied methodologies for DSF. Section 2.2 is a review of main papers about DSF. There are numerous papers on DSF written both by architects and engineers. Some of them present superficial and opposing ideas from an engineering point of view, some are redundant works of previous studies and some are not in English, due to the fact that DSF is initially an European technology and many findings were documented in other languages than English; thus, it is beyond the scope of this study to review all the papers. Therefore, Section 2.2 covers the main studies available in the literature. Section 2.3 covers thermal mass and its impact on thermal performance. Section 2.4 reviews some studies of thermal mass performance in buildings. Finally, section 2.5 concludes and summarizes the findings of this literature review.

2.1 Type of Studies

Experimental approaches and modeling are two types of studies that have been used to investigate thermal and energy performance of double-skin façades. Experimental approaches provide reliable information regarding airflow, heat flux, solar radiation and temperature distribution in DSF. However, it is not an easy task and the results are highly dependent on procedure and accuracy of measurement. Moreover, experimental

approaches are very lengthy processes and they take a long time to record the performance of DSF under real conditions. In this regard, various mathematical models have been developed to study the behavior of DSF or to optimize its performance. The modeling varies from very complex numerical modeling like CFD to simplified and analytical models. The level of sophistication of modeling being applied to DSF depends on the question at hand. Although numerical modeling might apply to many cases envisaged, it needs to be validated with experimental data or analytical models before making any judgment based on the result of numerical modeling.

2.1.1 Experimental Studies

Some studies of DSF system were experimental, either in lab or field monitoring. Since the lab provides controlled boundary conditions, it has been the more popular method. Field monitoring, the other type of experimental study is challenging. Even, many available field monitoring studies have been conducted on buildings with mechanically ventilated rather than naturally ventilated DSFs. This is because accurately measuring of airflow through air channel under real conditions is not a straightforward task.

2.1.2 Simulation Studies

The modeling or simulation of double-skin façades has been done more frequently. However, modeling of DSF is a complicated task, since different elements interact with each other and influence the function of the air channel. Efforts to model the air channel are focused mostly on:

- Air flow simulations,
- Calculation of the temperature at different heights and heat transmission through DSF's layers.

Air flow modeling of the DSF's air channel is necessary if one wants to study the temperatures distribution in the cavity. Air flow modeling mostly tended to have some sort of simplification or ignored some influential phenomena such as wind and intermediate shading devices. Hensen et al. (2002) explains that although airflow is demonstrably an important aspect of building/plant performance assessment, the sophistication of its treatment in many modeling systems has tended to lag behind the treatment applied to the other important energy flow paths. The principal reason for this would appear to be the inherent computational difficulties and the lack of sufficient data.

The approaches for calculating the air flow and temperature gradient inside the cavity differ in literature. Djunaedy et al. (2002) categorize the main airflow modeling levels of resolution and complexity as:

- ***Computational fluid dynamics (CFD)***: Detailed studies have been conducted using CFD and experiment for mechanically ventilated façades (Manz et al. 2004), for naturally ventilated façades (Manz 2004; Zollner et al. 2002) and for naturally ventilated façades equipped with venetian blinds (Safer et al., 2005). The CFD method calculates the airflow by solving continuum and momentum equations. An optical model is required (in combination with solar irradiance) to calculate heat

sources in glass panes and opaque surfaces of shading devices and other building elements.

- ***The network method***: Tanimoto and Kimura (1997); Gratia and De Herde (2004a); Gratia and De Herde (2004b); Gratia and De Herde (2004c) and Stec and Van Paassen (2005) used the nodal network method to find the airflow inside the air channel of DSF. In this method the air channel and its adjacent room are discretized to well-mixed zones. The network method then finds the airflow rate between zones by calculating pressure differences between discretized zones.

The approaches for calculating the temperature distribution inside the air channel and heat transmission can be divided to:

- In ***Computational fluid dynamics (CFD)*** continuum, momentum and energy equations are solved simultaneously to find temperature distribution (Manz et al., 2005).

- ***Lumped method*** represents each façade and cavity by a single temperature. Haddad and Elmahdy (1998); Park et al. (2004a) ; Park et al. (2004b); Von Grabe (2002) and Balocco (2002) used lumped model for naturally ventilated DSF.

- In ***Control-volume method***, first the whole façade is discretized vertically to several control volumes, and at the extent of each control volume only one temperature and

one-dimensional flow in the vertical direction is assumed. The air temperature stratification in a ventilated façade is evaluated by setting the air mass flow rate for each control-volume equal to the inlet air mass flow rate (Saelens, 2002; Faggembauu et al. 2003a; Faggembauu et al. 2003b; Athienitis et al. 2006a; Athienitis et al. 2006b). The control-volume model is used only to find air temperature distribution; the airflow rate has to be known a priori and it is not part of the numerical solution.

- ***Analytical method:*** Holmes and Beausoleil-Morrison (1994) developed analytical methods for ventilated DSF, which assume a linear vertical temperature gradient.

2.2 Main Previous Studies

2.2.1 Mechanically Ventilated DSFs

Mechanically-ventilated double-skin façade* is defined as a type of DSF having ventilation with the aid of powered air movement components (Loncour, 2004). Mainly there are three common types of mechanically-ventilated DSFs in practice: Indoor air circulation, Supply- and Exhaust-air DSFs. The thermal behavior of each type is different and basically each DSF can be modified to have one of these types at a time, depending on the season and control strategy.

1- Indoor Air Circulation DSF (IAC): also known as "Return Airflow Window" or "Air flow window" is a type of DSF that the supply air is from indoor and the

*In some literature there is a difference between "double-skin façade" and "double-skin window". This difference refers to the size of the glazed opening in the wall. Here, double-skin façade, air-flow window, exhaust- and supply-window refer to whole-floor height transparent glazing.

exhaust according to the control strategy can either be directly to the indoor and recirculated, or be exhausted to the HVAC system and redistributed through the HVAC system. The driving force of airflow inside the cavity is fan power. The direction of airflow might be upward or downward. The interior pane is reinforced single glazing, but the exterior pane is a double-glazed unit to avoid condensation by providing thermal insulation against the cold outer glazing.

In the heating season, this type of DSF contributes to heating load reduction in two ways. First, the ventilation air extracted through the façade with room air temperature helps to keep the indoor glazing close to the temperature of the room; therefore, less heating energy is consumed to maintain the room at set point temperature. In the second way, the heat lost through indoor glazing to ventilation air can be recovered and returned back to room. Especially during winter daytime, a large part of the solar incident energy is absorbed by the shading device and glazing and the ventilation air extracted by the cavity removes a part of the heat absorbed to the room or HVAC system. These two ways can effectively reduce the heating load of an attached room while at the same time limiting discomfort problems like radiation of the cold surfaces. However, in spite of the reduction of heating consumption in winter, in summer the indirect solar gains (relating to the heating of the blind and glazings) as well as the reduction of the heat losses through the façade can entail an increase in the energy consumption for cooling of the room.

2- Supply-air DSF (window): the supply air is from outside and the exhaust is directly to the inside. The driving force of airflow inside the cavity is fan power. The direction of airflow is normally upward. The interior pane is a single reinforced glazing and exterior pane is a double-glazed unit to avoid condensation. Haddad et al. (1994) state that the ventilation airflow makes it possible to reduce the heating load since the collected energy by the ventilation air from the window finds its way back to the room air. In addition, the air flowing through the two panes and then is introduced to the room fulfils the outdoor ventilation demand of the room. On the other hand, in summer the collected energy from the window in a sunny day can increase the cooling load.

3- Exhaust-air DSF (window): the indoor air flows between two panes and then exhausts to the outdoors. The driving force of ventilation air is fan power, and due to condensation restrictions, the exterior pane is a double-glazed unit and interior pane is single reinforced glazing. In the heating season, the heat loss through the outer pane of the window comes mostly from the ventilation air that was supposed to exhaust and this reduces transmission losses through the whole DSF. In addition, the ventilation air coming from indoor air helps to maintain the inner pane temperature close to room temperature, leading to heating load reduction and thermal comfort. In the cooling season, energy is required to cool the attached room when the heat gained indirectly by glazing and shading device is discharged by exhaust air (Haddad et al., 1994).

Main studies on mechanically-ventilated DSFs are summerized below:

Marques da Silva et al. (2006) conducted a post-occupancy monitoring of a building and concluded that overheating can occur when high air cavity temperature and high solar radiation coincide and that an efficient way to remove heat could be improvising the possibility to increase the air channel ventilation rate. They also concluded a white blind would certainly contribute to more efficient energy use by lowering air channel and inner glass pane temperature.

Hadad and Elmahdy (1998-99) conducted studies on the thermal performance of supply- and exhaust-air windows and comparison with conventional windows. By comparing supply- and exhaust-air window, they found that exhaust-air window lead to higher monthly net heat gains, especially in cold season. This increase is mostly because of conductive heat loss reduction (thermal resistance increase) rather than solar heat gain increase. In the second study they found that the heat loss is always lower in the case of the exhaust-air window and this heat loss difference with supply-air is the highest when the outdoor temperature is lowest. The solar heat gain was found to be higher in the case of supply-air window; the difference increases as the incident solar radiation increases. As far as thermal comfort is concerned, the exhaust-air window is superior to the supply-air window since it is associated with an inner pane temperature that is always closer to room temperature regardless of the season. Between conventional and supply-air windows, both provide almost the same comfort level inside the room although the temperature on the room side of inner pane is slightly lower in the case of the supply-air window. The authors used a computer program to simulate the performance of the

double-skin façade. The whole height of each pane was lumped to one temperature and was presented with only one node. One dimensional heat transfer was applied. No information about how to determine the convective heat transfer coefficient was provided. No blind was considered in thermal analyses and it was assumed the airflow rate is laminar and fully developed.

Tanimoto and Kimura (1997) studied the thermal characteristics of a type of airflow window composed of outer glazing, a shading device and roller blind (in place of inner glazing). The air on either sides of shading device (inner and outer cavities) was supplied from room air and exhausted mechanically by a fan at the top. A calculation procedure based on both the thermal and airflow network method was developed and evaluated with measurement data. For thermal modeling along the height of the airflow window, several horizontal layers were assumed. At the level of each layer a one-dimensional thermal network was employed (perpendicular to the window) and the heat balance at every discrete node was solved iteratively. There was no information regarding the selected convection heat transfer coefficient. The two-dimensional airflow network method was applied between room air, inner and outer cavities. By mechanical ventilation, the vertical pressure difference was given and the network method was able to predict pressure difference between inner and outer cavity (through the blind), inner cavity and room air. However, to find air velocity, the flow coefficient was among unknowns and no specific way for its calculation was provided.

Park et al. (2004b) developed a procedure to optimize the performance of the system by rotating a motorized blind slat in the cavity and ventilation dampers at the top and bottom of exterior and interior glazing. One prominent feature of the system was the capability of dynamically reacting to the environmental input data through real-time optimization in terms of energy, visual comfort and thermal comfort. It was shown that lumped models for double-façade components could be easily constructed and augmented by parameter estimation. The calibrated parameters compensate for errors introduced by the space averaging and other model simplifications.

McEvoy et al. (2003) conducted an experimental and modeling study of supply-air windows (supply from outdoor and exhaust to indoor) in winter condition. No shading device was considered in this study. The experiment was intended to clarify the effect of ventilation rates, the position of the low-e coating within the window as well as to provide data for the validation of a simulation model. The case was simulated using ESP-r, and discretization of air cavity to small control volume was done to take into account thermal stratification. It was found that pre-heating of the incoming air via the window was reduced as ventilation rates increased and the effective U-value (which considers air ventilation) of the supply air window also decreased with increasing ventilation. The inner pane of the supply-air window was double-glazed. The effective U-value was halved when a low-e coating was placed on inner pane of double-glaze in compared with outer pane (the outer pane of double glazing was next to air cavity). ESP-r simulation program predicts the pre-heating very well but variation in the heat transfer coefficient at

different flow rates through the window increased the extent of error at low flow rate (5 l/s).

2.2.2 Naturally Ventilated DSFs

Naturally-ventilated DSF is defined as a type of ventilated DSF in which ventilation relies on two driving forces: stack effect and wind *.

In contrast to mechanically-ventilated façades, the naturally ventilated one is essentially characterized by variable performances linked to the meteorological conditions (wind and temperature difference). These variables significantly complicate the design of the façade as well as the estimation of the thermal or ventilation performances of façades of this type. Indeed, while it is possible to guarantee the performances of a mechanically ventilated system, this is not necessarily the case for naturally ventilated because, essentially, the performance of natural ventilation depends on meteorological conditions (Loncour, et al, 2004).

A naturally-ventilated DSF does not need fan power and provides a more tranquil environment; however, a mechanically-ventilated DSF has better performance in summer time. Li (2001) reported that a mechanically-ventilated DSF has 25% more cavity heat removal rate compared with naturally-ventilated DSF. Appendix H discusses in detail the influential parameters in thermal performance of naturally ventilated DSF.

*If there is an opening between the room and DSF, a third driving force can be the pressure produced by pressurization/depressurization of building mechanical system.

Main studies on naturally-ventilated DSF s are summarized below:

Manz (2004) studied an external air circulation (supply and exhaust both from and to outside), naturally-ventilated DSF with mid-pane shading device in summer. He aimed to find the influence of glazing layer sequence (location of solar protective layer, either interior or exterior pane) and ventilation properties of cavity (the mid-pane shading device either completely or partially closed) on total solar energy transmittance (g-value) of DSF. A procedure for modeling such façades, comprising a spectral optical and a computational fluid dynamic (CFD) model was described and simulation results were compared with measurements. It was found that having a solar protective layer on exterior glazing is superior to having this layer on interior glazing, due to less solar absorption in summer. Moreover, partially closed shading screen leads to more ventilation in the cavity and less g-value, which is beneficial in summer time. It was mentioned that windless condition was considered to have the worst case scenario for cooling load in summer.

In another study, Manz et al. (2005) developed a procedure for modeling DSF. The model was composed of a spectral optical and a computational fluid dynamic model; the CFD was not able to do radiation analysis. The simulated results were compared with experimental data of two mechanically ventilated DSFs built in an outdoor test facility. They concluded that a combination of experiment and simulation is considered the most reliable approach for analyzing DSFs.

The influence of the layer sequence and ventilation properties on the thermal behavior was also discussed by Manz (2004). It was shown that, for a given set of layers, total solar energy transmittance (g-value) can easily vary by a factor greater than five. It was shown that with a well-designed DSF element in naturally ventilated DSF, indirect heat gains can be reduced to values below 2%. Total solar energy transmittance values (g-value) lower than 10%, which was recommended for highly glazed buildings, can be readily achieved with such façades. Also, low indirect heat gains are obtained if:

- Total solar absorption is low and mainly in the external layer;
- Ventilation is efficient (large ventilation openings, etc.);
- Thermal transmittance (U-value) of glazing layers is low;
- Reflectance of shading device is high within the wavelength interval where the external layer is transparent.

For multistory buildings with DSF, an increase both in temperatures in the façade cavities and in total solar energy transmittance (g-value) is observed as a function of height. It was observed in the experimental investigations that short-term wind fluctuations can reverse the direction of airflow in the façade cavities by 180 degrees and these fluctuations vary the air change rate. Yet, provided they are limited to short periods, such changed airflow patterns are likely to have only a minor impact on energy flows. A windless situation should be assumed as a worst-case scenario for overheating (Manz et al., 2005).

Zollner et al. (2002) conducted numerical and experimental studies in an external air circulation (both supply and exhaust from and to outside), naturally-ventilated DSF at the Technical University of Munich. The purpose of the investigation was to determine the averaged overall heat transfer coefficients as a function of average mean Archimedes number for several air channel distances. The windless condition was considered for this study. To obtain this condition a pressure compensation method was applied. They found that air mass flow rate inside the cavity increases with temperature difference between panes and cavity air, and also with increase of inlet opening. The air mass flow had higher rates for deeper cavity at the same temperature difference for bigger opening. The average mean Nusselt number decreased with increase of average mean Archimedes number. This decrease was sharper for deeper cavity.

Balocco (2001) used the steady-state energy balance at each control volume to find the energy performance of different ventilated façades. Then she studied the effect of channel width on heat transfer rate and airflow velocity inside the ventilated façade. Results showed that both air mass flow rate and stack effect in the channel increased with cavity width, and it was possible to obtain cooling effect when the air cavity width of the chimney was wider than 7cm. This study has a simple and straightforward methodology; however, it is applicable only to a single channel (no blinds inside the cavity) and the façade layers are all opaque (no solar radiation passing through façade). These restrict its use in current study.

Balocco (2004) also proposed a method based on dimensional analysis to study naturally-ventilated DSF energy performance. The 14 non-dimensional numbers can be used to describe thermal and energy performance of different façade designs.

Artmann, et al. (2004) studied the effect of tilt angle and position of a shading device inside the air cavity on thermal behavior of naturally-ventilated DSF (air supply and exhaust both from and to the outside) in order to avoid overheating in summer. They used CFD analysis coupled with boundary conditions derived from an outdoor test cell at Technical University of Munich. CFD and measurement results showed interior façade temperature increases and airflow velocity decreases at a lower tilt angle. CFD and flow visualization showed that a lower tilt angle of venetian blind extends more turbulent airflow region through the cavity air. This means more homogenous temperature distribution through cavity air. Regarding the effect of position of shading device, the same trend can be mentioned if the venetian blind is located far from the interior or exterior pane (in the center of the cavity). Therefore for positions near one of the panes, high temperatures occur in the smaller cavity with pane, while the air on the opposite side of the venetian blind shows a thermal layering with relatively cool temperatures near the inlet and higher temperatures close to the outlet.

Yamada et al. (2005) studied a prototype building with a naturally-ventilated DSF and its ventilation rate, both experimentally and with the aid of CFD modeling. Compared with conventional DSF, a thermal storage space called the solar chimney was set up above the DSF space to strengthen stack effect occurring in the intermediate space, and thus to

ensure stable natural ventilation performance throughout the building even without encouragement of wind. Reduced scale model experiments and CFD analysis were conducted to unfold detail discussions. It was concluded that increasing the height of the solar chimney makes more ventilation rate. As there are always limitations on the acceptable height of the solar chimney, the solar chimney was recommended to be more than two floors high.

Saelens et al. (2003) reported that external air circulation double skin façades in heating seasons perform poorer than indoor exhaust and supply airflow windows; however in cooling seasons the external air circulation double skin façade is superior. Moreover, they reported that when the shading device is lowered in the façade's intermediate space, the airstream is divided into two parts. A major portion of the air is likely to be heated up by the shading device and rises directly to the air-extract opening at the top. The remainder of the air, at a greater distance from the shading device, will not be heated to the same extent and will ascend more slowly. Only where the cavity between the façade skins is relatively shallow (less than about 40 cm) there are significant pressure losses likely to occur. Otherwise, the intermediate space offers no major resistance to the airflow. In most double-skin façades, the greatest pressure losses occur when the air passes through the extract opening. The acceleration of the air through this comparatively small aperture is not basically different from that occurring at the air-intake opening at the base; but at the air-extract opening, the airstreams will be subject to greater deflections as passing around obstacles such as shading device or rainwater traps.

Hamza (2008) developed an analytical approach using dynamic simulation software (APACHE-Sim) to predict the performance of double skin façades, in hot arid areas. In this paper, a comparative analysis of cooling loads on a single skin base-case is compared with three possible changes to the physical properties of the external layer of the double skin façade. Simulation results indicate that a reflective double skin façade can achieve better energy savings than a single skin with reflective glazing.

In another study by Hamza et al. (2005) a CFD model was used to predict air flow rate and temperature within the channel of DSF for the case of an air-conditioned building in a hot arid climate. This case allowed a CFD model to be applied to the façade independent of the simulation of the main building and its plant. Results show appreciable flow rates and temperatures generated mainly by buoyancy flow over the outer façade skin.

Li (2001) proposes a protocol for experimentally determining the performance of a DSF system. The protocol was applied to an experimental study of a south-facing, single story DSF system. Two modular full-scale double glazed window models with naturally or mechanically assisted ventilation were constructed and monitored for a range of weather conditions. The goals of this investigation were to develop and apply the test protocol and to monitor and analyze the thermal performance of these two systems. Using this test protocol, preliminary results show the average cavity heat removal rate is approximately 25% higher for the active system as compared with the naturally ventilated system. Also,

the passive system has a higher temperature difference between the indoor glass surface and the indoor air than the active system.

Marques da Silva et al. (2008) performed a set of wind tunnel tests under a boundary layer velocity profile and different wind incidence angles in order to obtain inner façade pressure distributions for different DSF layouts and air channel depths. All tested layouts were of the multi-storey DSF type, open at the top and the base, allowing free air movement within the cavity. The experimental data for the building model showed a layout dependent inner wall pressure distribution that is considerably different from the unsheltered building. The pressure coefficients within the DSF air channel were found to be always negative regardless of the incident wind direction.

Pappas et al. (2008) have developed an integrated CFD and BESP (Building Energy Simulation Software) model to analyze the thermal performance of double skin façade with buoyancy-driven airflow. The model was validated using measured data. The study investigated the energy performance and potential influential factors of such a DSF. They developed a set of correlations for cavity airflow rate, air temperature stratification, and interior convection coefficient; these can provide BESP with a more accurate annual energy analysis of a naturally ventilated DSF than that is currently possible.

Gratia et al (2007) showed the influence that the position and the color of the blinds could have on the cooling load in an office building with a double-skin façade. They also highlighted the importance of the opening of the double-skin. Proper positioning of the

blinds makes it possible to save up to 14.1% of the cooling consumption of all the building during sunny summer day. Good color choice can save up to 3.5%. The impact of the damper's opening ratio is from 7.4% to 12.6% reduction of energy consumption. Another interesting factor is the impact of the blinds' characteristics on human comfort. The position and the color of the blinds have an influence on the temperature of the windows of the inside surface and eventually of the occupants' thermal comfort.

Gratia et al. (2007) also conducted a study to find if the greenhouse effect is favorable in DSF. In the study the DSF was composed of an external wall entirely glazed and an internal wall combined of glazing and opaque wall which is able to accumulate heat. Thus the solar radiation penetrating through external glazing and stroking the opaque wall is absorbed. This trapped heat in the double-skin façade is responsible for the greenhouse effect. For this study a constant wind speed was considered during all the day and the building was located in an open site. It was concluded if no natural strategy is implemented to try to decrease cooling consumption (the double-skin remains closed, solar protections are not used, the strategies of day and night natural ventilation are not used), the greenhouse effect must be decreased. If natural cooling strategies are used,

- the greenhouse effect is favorable if the double-skin is south oriented;
- the greenhouse effect has no impact if the double-skin is north oriented;
- the greenhouse effect is unfavorable if the double-skin is east or west oriented.

Temperature in the double-skin is always lower in a DSF with a higher proportion of glazed surfaces to opaque wall in the interior façade.

Gratia et al. (2007) also examined how natural ventilation can be provided during a sunny summer day in an office building with a naturally-ventilated DSF. They concentrated on the possibility of natural ventilation during the daytime in relation to the orientation of the double skin and the speed and orientation of the wind. It is a simulation study implemented in the thermal program TAS. They determined the way in which the double skin windows should be opened, and the size of the openings necessary to achieve a ventilation rate of 4 ach in each office under various wind conditions. They noted that the results cannot be generalized to other configurations of double-skin façade, and are insufficient for the technical design of a double skin.

Implementation of hybrid DSF as a design option on an east façade was evaluated by Høseggen et al. (2008). In this study, a planned office building in the city-centre is used as a case for considering whether a double-skin should be applied to the east façade in order to reduce the heating demand, thus making the double-skin façade a profitable investment. The building was modeled both with and without a DSF using the building energy simulation program ESP-r. The simulation results indicated that the energy demand for heating is about 20% higher for the single-skin façade with the basic window solution compared to the double-skin alternative. However, by switching to windows with an improved U-value in the single-skin alternative, the difference in energy demand is almost evened out. The number of hours with excessive temperatures is, in contrast to other studies on the subject, not significantly higher for DSF. However, the predicted energy savings are not sufficient to make the application of a DSF profitable. In this

study shading device was ignored and default correlations of ESP-r for convection coefficient were adopted.

Sun et al. (2008) examined DSF as a possible solution for energy efficiency in highly glazed buildings for China. In this paper, a comparative analysis of heating and cooling loads of a typical office cell with DSF was made against a single-skin façade and a traditional window-wall façade in the climatic conditions of Shanghai. The coupling of the spectral optical model GLSIM and the dynamic thermal model HTB2 was used as the simulation method. Simulation results indicated that both heating and cooling energy savings can be achieved using a reflective double-skin façade with the appropriate choice of ventilation method. However, the airflow modeling was oversimplified; information about shading device effect on insolation and the algorithm to calculate the convection coefficient was not provided.

In another study Heiselberg. et al. (2008) described the results of two different methods to measure the air flow in a full-scale outdoor test facility with a naturally-ventilated DSF. They reported that air flow rate in a naturally-ventilated double skin façade (DSF) was extremely difficult to measure due to the stochastic nature of wind, and as a consequence of non-uniform and dynamic flow conditions. Although both methods were difficult to use under such dynamic air flow conditions, they show reasonable agreement and the data can be used for experimental validation of numerical models of natural ventilation air flow in DSF. Simulations by the thermal simulation program, BSim, based on measured weather boundary conditions, were compared to the measured air

temperature, temperature gradient and mass flow rate in the DSF cavity. The results show that it is possible to predict the temperature distribution and airflow in the DSF with the aid of a building energy simulation program although some discrepancies are inevitable.

Perez-Grande et al., (2005) studied the influence of the glass properties on the performance of DSF. The total heat rate into the building has been calculated for ten different façades formed by different glass combinations. A CFD modeling was developed for this purpose. Focusing the attention only on the thermal balance (leaving apart other aspects like aesthetics or cost), it has been demonstrated that an appropriate selection of the glass forming the channel can reduce the thermal load into the building by fifth.

Zerefos (2007) compares the heating and cooling loads between a double skin façade and a single skin façade in different and contrasting climates. It was a simulation study implemented in ECOTECT combined with WINDOW. The DSF was naturally ventilated and venetian blinds were considered in the air channel between two glazings. The algorithm for airflow modeling and calculation of convection coefficient were approximated using software default value and/or CEN standard. The results showed that in sunny climates such as the Mediterranean due to U-value improvement and g-value reduction achieved by DSF, double skin façades are considered to be preferable during the cooling season (29%-35% annual saving in Mediterranean). In fact, the more sunshine days the site has, the less energy consumption DSF will have compared to a single skin façade. In contrast, in cold Continental climates, such as Moscow, as well as

temperate, such as London, the difference in performance of the double skin façade and single skin façade is generally reduced especially during the heating season. The use of DSF results in g-value reduction, which is undesirable in heating season. However, U-value improvement and preheating effects outweighs and contributes to some saving. In Moscow this saving is 8.3% annually.

A study by Von Grabe (2002) deals with the development and the testing of a simulation algorithm for the temperature behavior and the airflow characteristics of double façades. It has been developed in order to obtain a tool which enables the energy consultant to make quick design decisions without being required to use fairly complicated CFD tools. In order to determine the degree of accuracy of the algorithm, a double façade has been monitored under controlled conditions and the results have been compared against the predicted values for several design situations. They concluded that major errors may happen by assuming symmetric velocity profiles having the highest velocity at the centre (like pipes) for a naturally-ventilated DSF. This is because in a naturally-ventilated DSF the driving force is the reduction of the density due to the increase of air temperature. This increase is greater near the heat sources such as near the panes and the shading device.

Ismail and Henriquez (2004) used two dimensional transient model based on equations of mass, momentum and energy conservation (CFD analysis) to investigate the temperature and velocity field across and along the ventilated channel in different channel width and solar incident conditions. The results indicated that the air channel width has little effect

on the mean coefficient of solar heat gain and the shading coefficient, while the increase of the inlet fluid temperature is found to deteriorate the thermal performance. Although the modeling has a high resolution and is able to cover many thermal performance parameters, it does not consider the blind inside the channel.

2.3 Conclusion

The main points concluded from the above literature review are:

- Among different methods to find airflow and temperature distribution, CFD can provide detailed information. However, CFD itself is not able to take into account radiation analysis and needs to be coupled with Building Energy Simulation Program (BESP) in order to provide the boundary conditions. In addition to this dependency on BESP, CFD still needs validation with experimental measurements (Manz, 2004; Zollner et al. 2002). Using simpler methods like BESP thoroughly decreases the amount of calculation but it also needs some calibration with measurements for airflow parameters (Park et al., 2004a; Park et al., 2004b). In conditions that both CFD and simpler methods need measurements for verification, simpler methods with fewer details might be more appropriate depending on question at hand.

- It should be noted that the potential limitation of using steady-state CFD analysis over transient analysis is the inaccuracy in analyzing conductive heat transfer through massive materials, in which the thermal capacity creates a delay in heat transfer (Pappas, 2006). In spite of the fact that the CFD analyses applied in literature for DSF modeling were steady-state, it took a great deal of

computational time. For the condition wherein transient CFD analyses are needed, CFD might not be a very practical method (unlike glass, thermal capacity is not negligible in thermal mass).

- There are opposite ideas of how complex the modeling approach needs to be. Some researchers insist that the complex interactions that occur within the system necessitate the use of a model with sufficient level of complexity (Saelens. 2003). Others state that the simplicity of the numerical model and its input is necessary for users. Complex and time-consuming building simulation tools should be avoided, to encourage the use of modeling. However, Holmes et al. (2008) reported that in the case of global rather than spatially-resolved quantities, a generally good agreement between the two modeling approaches was obtained.

- Most of studies have been done while considering convection coefficient as a given variable (Hadad and Elmahdy, 1998-99; Balocco., 2001; Faggembauu et al. 2003). This can be a source of uncertainty in the case of naturally-ventilated DSF. Hence, there is a need to find the appropriate convection coefficient for each interacting surface.

- The majority of studies have ignored totally the existence of blind in modeling. Artmann et al. (2004) reported that there is no suitable publication on flow characteristics in the air cavity with a shading device. Many similar cases of

modeling referred to in literature have been roller blind (Saeleans 2001, Pappas., 2006) and metalized flat screen (Manz et al., 2003). There are just a few studies considering venetian blinds (Tanimoto and Kimura, 1997; Artmann et al, 2004), while in constructed DSF buildings, mainly venetian blinds are in use. Venetian blinds affect modeling in terms of absorbed and transmitted solar radiation, air cavity ventilation patterns, cavity enthalpy gains and total solar energy transmitted through the DSF.

- Evaluating the energy efficiency of DSF cannot be done simply by analyzing heat loss and gains through DSF. Enthalpy change of the cavity air also needs to be taken into account (Saelens et al, 2003). This means that the whole energy analysis of DSF and its attached room, together can give a fair judgment of DSF energy efficiency.

- The effect of ventilation rate and air channel width on thermal performance of DSF system have been the subject of many parametric studies in the literature (Zollne et al., 2002; Balocco, 2001 ; Ismail and Henriquez, 2004; Saelens et al, 2003). However, shading device as a main absorber and source of heat inside DSF has received limited attention although its importance in overheating was mentioned (Manz et al., 2003; Marques da Silva, et al., 2006). Therefore, there is a lack of comprehensive study on shading device itself and the possible solution of preventing the shading device from causing overheating.

- It appears that there has not been any consensus on thermal performance criteria of DSF since different studies used different parameters (Saelens, 2002; Corgnati et al., 2003; Faggembauu et al. 2003, Perino et al, 2005). Moreover, most of parameters are applicable only to steady-state study of DSF.

- Thermal mass and double skin façade have been two separate concepts used to make building more energy efficient, and there has been a lack of study on integration of these two concepts in order to come up with a more energy efficient technique. One drawback of double skin façade is the risk of overheating during cooling season which is inherent in highly glazed façades. Integration of thermal mass may decrease the overheating risk.

- Location, thickness and exposed surface area are among the influential parameters of thermal mass thermal performance. In the current study of integrating thermal mass with a DSF system, replacement of an inner, outer or shading device layer with thermal mass leads to different performances of DSF. Shading device replacement, for example, provides twice the surface area than inner or outer glazing replacement and stores heat more effectively while the interaction of thermal mass with room air is indirect, and energy releasing of thermal mass is not as effective as energy releasing of inner glazing replacement. Therefore, a parametric study on the replacement of proposed thermal mass (either with inner, outer or shading device) with a different thickness will show which option is more energy efficient.

- Diurnal variation of ambient temperature affects thermal performance of thermal mass. In the current study, by placing the thermal mass inside the air channel, in addition to ambient temperature, the air channel's diurnal variation of temperature affects the performance of thermal mass and the integrated system. Therefore, a parametric study on the type of ventilation (naturally, mechanically) and airflow path (Indoor air circulation, outdoor air circulation, exhaust air and supply air) is needed to find the most efficient option.

CHAPTER 3
METHODOLOGY

Following the discussions in previous chapters, numerical modeling is the study approach to investigate the thermal behavior of DSF. The main objective is to generate the performance data of concrete thermal mass and its contribution to the energy efficiency of the system by predicting thermal profiles in the double-skin façade, and to generate the resulting cooling/heating loads for the adjacent perimeter interior zones during extreme summer/winter conditions. Generally, the temperature in the cavity at different height is of interest for manufacturing and construction methods. The interior zone's cooling/heating loads are needed for sizing the HVAC systems and there is little interest in the flow field itself; however, it is required as a prerequisite to find the cavity's temperature distribution. Airflow modeling is not needed when it is ventilated mechanically since the airflow rate is a known parameter. This chapter addresses the methodology to determine airflow rate inside the channel, the temperature distribution of DSF and heating/cooling loads of the DSF perimeter zone. In chapters 3 and 4, base-cases are developed based on this methodology and then will be verified using measurement data obtained from naturally- and mechanically-ventilated outdoor test-cells.

3.1 Airflow Modeling

Although airflow is an important aspect of building/plant performance assessment, the sophistication of its treatment in many modeling system has tended to lag behind the

treatment applied to the other important energy flow paths. The principal reason for this would appear to be the inherent computational difficulties and the lack of sufficient data (Clarke. 2001). Nowadays, there are two airflow simulation approaches more common in the building domain: Computational Fluid Dynamics (CFD) and the Network method. The Network method is of course much faster but will only provide information about bulk flows. CFD on the other hand will provide details about the nature of the flow field.

In the case of a forced-ventilated double-skin façade, one-dimensional and vertical airflow is assumed for the whole air channel. Therefore, no airflow modeling is needed and the given airflow rate is directly applied to thermal modeling. However, a nodal, unidirectional airflow network method is applied in the case of naturally-ventilated double-skin façade. For sake of simplification, no airflow is considered through blind.

In the current study for the case of a naturally-ventilated DSF, the thermal side of the problem for performance evaluation is more important than the airflow pattern aspects, and the only output needing to be extracted from airflow modeling is the value of airflow rate at each time step. This value makes it possible for thermal modeling to calculate temperature distribution and heating/cooling loads.

Also, considering the details needed for proposed thermal modeling and the very detailed results generated by expense of time and computational power in CFD, the Network approach is more appropriate. Even if the CFD approach is applied, there are not enough

measurements to verify the very detailed results. Therefore, the bulk flow rate value calculated by the Network approach will be applied for this simulation study.

3.1.1 Nodal Airflow Network

In this method, the whole construction is simplified to one or multi well-mixed zones, any of which is represented by a node. These nodes may represent internal zones or be located in ambient air. Linkages are assumed between these nodes based on probable airflow between zones or with ambient air.

After linking the nodes, the next step is to find the pressure difference between them. Section 3.1.2 describes in detail how to find pressure difference based on airflow direction in a naturally ventilated double-skin façade.

After finding the pressure difference, like most airflow models the empirical power law equation (3.1) is then applied to approximate the relation between airflow and pressure difference across the opening.

$$\dot{Q} = C\,(\Delta P)^n \qquad (3.1)$$

The volumetric flow rate, Q (m^3/s), is a simple function of the pressure drop, ΔP (Pa), across the opening. Theoretically, the value of the flow exponent should lie between 0.5 and 1.0. Large openings are characterized by values very close to 0.5, while values near 0.65 have been found for small openings (Walton, 1994).

A common variation of the power law is related to the orifice equation:

$$m_{i,j} = C_d A\sqrt{\frac{2\,(\Delta P_{i,j})}{\rho}} \tag{3.2}$$

where

i,j = two linked pressure nodes;

C_d = discharge coefficient, commonly taken as 0.65;

A = orifice opening area.

Writing continuity equation for each node i we have,

$$\sum_{j=1}^{n} m_{i,j} = 0 \tag{3.3}$$

n = the total nodes linked to node i

if the pressure node $i=1$ *to* k

then,

$$\begin{cases} m_{1,2} + m_{1,3} + m_{1,4} + \ldots + m_{1,n} = 0 \\ m_{2,1} + m_{2,3} + m_{2,4} + \ldots + m_{2,n} = 0 \\ \cdot \\ \cdot \\ \cdot \\ m_{k,1} + m_{k,2} + m_{k,3} + m_{k,4} + \ldots + m_{k,n} = 0 \\ k \neq n; k > n \end{cases} \tag{3.4}$$

and,

$$\begin{cases} C_d A\sqrt{\frac{2\,(\Delta P_{1,2})}{\rho}}+C_d A\sqrt{\frac{2\,(\Delta P_{1,3})}{\rho}}+C_d A\sqrt{\frac{2\,(\Delta P_{1,4})}{\rho}}+\ldots+C_d A\sqrt{\frac{2\,(\Delta P_{1,n})}{\rho}}=0 \\ C_d A\sqrt{\frac{2\,(\Delta P_{2,1})}{\rho}}+C_d A\sqrt{\frac{2\,(\Delta P_{2,3})}{\rho}}+C_d A\sqrt{\frac{2\,(\Delta P_{2,4})}{\rho}}+\ldots+C_d A\sqrt{\frac{2\,(\Delta P_{2,n})}{\rho}}=0 \\ \cdot \\ \cdot \\ \cdot \\ C_d A\sqrt{\frac{2\,(\Delta P_{k,1})}{\rho}}+C_d A\sqrt{\frac{2\,(\Delta P_{k,2})}{\rho}}+C_d A\sqrt{\frac{2\,(\Delta P_{k,3})}{\rho}}+\ldots+C_d A\sqrt{\frac{2\,(\Delta P_{k,n})}{\rho}}=0 \\ k\neq n; k>n \end{cases} \tag{3.5}$$

(P_i , *i=1 to k* is the known pressure and ρ is known as a priori or can be determined at each time step simultaneously with the thermal model using ideal gas law)

If all nodes have known pressures applying equation (3.2) it is easy to find the airflow rate between each two nodes without solving a system of equations; however, normally there are some unknown pressure nodes at each time step, so there is a need for an iterative solution procedure at each time step to find *P*. Moreover, since the orifice equation is nonlinear (*m* respect to *P*), the iterative solution procedure should be able to solve simultaneous nonlinear algebraic equations.

It should be noted that in order to avoid insoluble flow network, two conditions need to be met all the time. First, the pressure of at least one node within the network must be a

priori known. Second, all unknown nodal pressure must be linkable, by some path, to a node whose pressure is known.

It is very common to use Newton-Raphson to solve this nonlinear problem in a system of equations. Based on the Newton-Raphson method, which is a root finding method and has been derived from first-order Teylor series expansion, the independent variable x_{i+1} is equal to (Chapra, et al. 2002):

$$\begin{cases} f\left(x^{i}\right)=0 \\ x^{i+1}=x^{i}-\dfrac{f(x^{i})}{f'(x^{i})} \end{cases} \tag{3.6}$$

a multi-variable version of above equation is:

$$X^{i+1}=X^{i}-\left[J(X^{i})\right]^{-1}F(X^{i}) \tag{3.7}$$

$$X=\begin{bmatrix} x_1 \\ x_2 \\ x_3 \\ . \\ . \\ . \\ x_k \end{bmatrix};\quad F(X^{i})=\begin{bmatrix} f_1(x^{i})=f_1 \\ f_2(x^{i})=f_2 \\ f_3(x^{i})=f_3 \\ . \\ . \\ . \\ f_k(x^{i})=f_k \end{bmatrix};\quad \left[J(X^{i})\right]=\begin{bmatrix} \frac{\partial f_1}{\partial x_1} & \frac{\partial f_1}{\partial x_2} & \frac{\partial f_1}{\partial x_3} & \cdots & \frac{\partial f_1}{\partial x_k} \\ \frac{\partial f_2}{\partial x_1} & \frac{\partial f_2}{\partial x_2} & \frac{\partial f_2}{\partial x_3} & \cdots & \frac{\partial f_2}{\partial x_k} \\ \frac{\partial f_3}{\partial x_1} & \frac{\partial f_3}{\partial x_2} & \frac{\partial f_3}{\partial x_3} & \cdots & \frac{\partial f_3}{\partial x_k} \\ . & & & & \\ . & & & & \\ . & & & & \\ \frac{\partial f_k}{\partial x_1} & \frac{\partial f_k}{\partial x_2} & \frac{\partial f_k}{\partial x_3} & \cdots & \frac{\partial f_k}{\partial x_k} \end{bmatrix}$$

$J(x^{i})$ in this equation is formally referred to as Jacobian matrix.

If there are three pressure nodes or k=3 then based on (3.3):

$$\begin{cases} \sum_{n=1}^{3} m_{1,n} = m_{1,2} + m_{1,3} = \mathrm{f}_1 = 0 \\ \sum_{n=1}^{3} m_{2,n} = m_{2,1} + m_{2,3} = \mathrm{f}_2 = 0 \\ \sum_{n=1}^{3} m_{3,n} = m_{3,1} + m_{3,2} = \mathrm{f}_3 = 0 \\ k > n ; k \neq n \end{cases} \tag{3.8-a}$$

After substituting f_1, f_2 and f_3 into equation (3.7), it is possible to estimate pressure at each node:

$$\begin{cases} p_1 = x_1 \\ p_2 = x_2 \\ p_3 = x_3 \end{cases} \tag{3.8-b}$$

For more information regarding the Newton-Raphson method and the inverse of Jacobian matrix refer to Chapra, et al. (2002).

3.1.2 Finding Pressure Difference between Nodes

In this study, the double-skin façade has been divided vertically from top to bottom to several pressure zones, according to resolution needed (here four divisions) and horizontally to two zones, one in front and the other at the back of the shading device (see Figure 3.1). These internal zones are represented by internal nodes (one per zone). In addition there is at least one ambient pressure node which represents the boundary condition node. Here the method is first to find the pressure difference between each two nodes and then to find the mass flow rate.

In the naturally-ventilated double-skin façade there are two driving forces: the force caused by (1) the pressure difference due to thermal buoyancy and (2) the difference in wind pressure across the lower/upper ventilation dampers. The former will mainly cause upward flows, as the cavity is ventilated with air entering to cavity from the inlet. The latter may cause either upward or downward flows, depending on wind speed and wind direction and its interaction with buoyancy force. Also, a third driving force may be considered, produced by building mechanical systems.

If the linkage is between interior zones, normally the driving force to create the pressure difference is due to buoyancy and pressure difference of the zones. If the linkage is between interior zones and ambient air, then in addition to buoyancy forces, wind pressure on the exterior surfaces is another driving force.

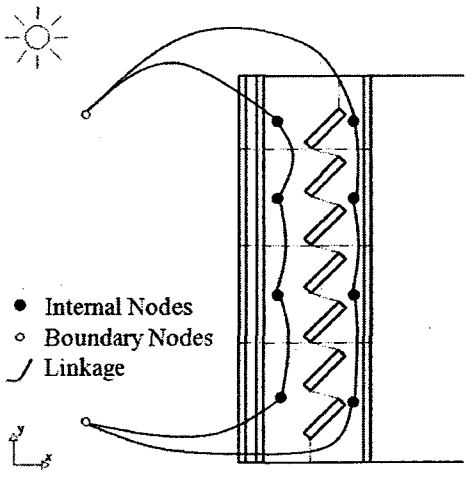

Figure 3.1: Discretization of DSF with imaginary surfaces to pressure zones. Here, the DSF has been divided to 8 internal zones and the pressure node is situated at the center of each zone. Two boundary nodes are located at the upper and lower end of the DSF. Linkage is for the case of outside circulation direction.

Based on airflow direction, three types of airflow regimes in naturally ventilated double-skin façades may occur:

1) Supply and exhaust are both from and to the room and there is no fan to circulate air through the air channel (figure 3.2a). In this case, temperature difference causes air density differences. This produces buoyancy force which moves the flow upward in the cavity. The effects of air density on the pressure can be considered as (figure 3.3):

$$P_i = P_m + \rho_m g (z_m - z_i) \tag{3.9}$$

$$P_j = P_n + \rho_n g (z_n - z_j) \tag{3.10}$$

Subscripts *i* and *j* refer to two adjacent nodes and Z_i and Z_j are global reference heights, while Z_m and Z_n are local reference heights. Local reference heights are chosen arbitrarily for convenient and physically meaningful representation. P_n and P_m can be absolute or gauge pressures since only pressure difference cause airflow.

The pressure difference across the opening is:

$$\begin{aligned} \Delta P_{i,j} &= P_i - P_j \\ &= P_m - P_n + \rho_m g (z_m - z_i) - \rho_n g (z_n - z_j) \\ &= P_m - P_n + Ps \end{aligned} \tag{3.11}$$

Then,

$$Ps = \rho_m g (z_m - z_i) - \rho_n g (z_n - z_j) \tag{3.12}$$

is the stack pressure (Walton, 1984).

Normally the difference between static pressures (P_m-P_n) is negligible and Ps is the main driving force. In other words, the temperature difference at different heights of DSF causes natural ventilation. The portion of pressure difference across upper/lower ventilation dampers which is due to mechanical system pressurization/depressurization can be cancelled out from inlet and outlet nodes in iterative solution.

2) Supply and exhaust are both from and to the ambient air and there is no fan to circulate air through the air channel (figure 3.2b). In this case, there are two driving forces for air movement. The first one, like case 1, is the temperature difference and buoyancy force. Another driving force is generated as a result of wind effect. To find the pressure of wind effect, known as wind pressure P_w, two parameters are needed, C_p and v_r, as well as surface pressure coefficient (N m^{-2}) and wind velocity (m s^{-1}) at direction of the surfaces . Appendix A explains how to derive v_r, knowing velocity and direction of wind at each time step.

$$P_w = C_p \cdot \frac{1}{2} \rho v_r^2 \tag{3.13}$$

Then the pressure difference across the inlet or outlet damper is:

$$\begin{aligned} \Delta P_{i,a} &= P_i - P_a + P_w \\ &= P_m - P_k + \rho_m g (z_m - z_i) - \rho_k g (z_k - z_a) + P_w \\ &= P_m - P_k + Ps + P_w \end{aligned} \tag{3.14}$$

where P_a is an ambient pressure node in front of an inlet/outlet damper and P_i is an interior pressure. Z_k is the local reference for the room pressure node. The difference between static pressures is negligible and Ps and P_w are the main driving forces. Ps causes upward flow, however interaction with wind pressure, which has higher magnitude, may cause upward or downward airflow inside the air channel. Pressure differences between interior pressure nodes ($\Delta P_{i,j}$) is obtained the same way as in case 1.

3) There is a diagonal flow between ambient and room air. Either the outside air is brought to the room or the air comes from inside of the room and is evacuated toward the outside (figure 3.2c). There is no fan to circulate air through the air channel. There is one additional driving force in this case and that is pressure caused by mechanical systems (P_{mech}) inside the room. The pressure difference across the inlet or outlet damper is then:

$$\Delta P_{i,a} = P_m - P_k + Ps + P_w + P_{mech} \tag{3.15}$$

where

P_{mech} is the pressurization or depressurization due to mechanical systems. Depending on magnitude of Ps, P_w and P_{mech}, the flow direction is either upward or downward.

The pressure differences producing air leakage arise from wind, buoyancy and pressurization by HVAC systems. It should be noted that when two or all three of these effects occur at the same time, the total pressure differences are found from the algebraic sum of pressure differences produced by each effect acting alone.

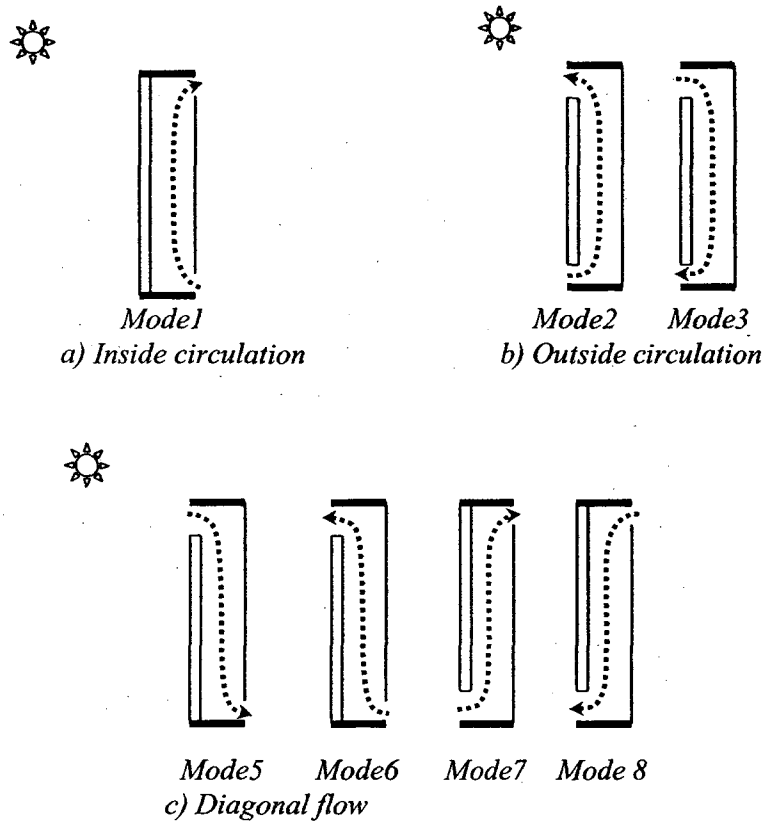

Figure 3.2: Eight possible airflow regimes (shading device is not drawn). Here it was assumed indoor and outdoor skins are airtight and the airflow is happening just through inlet and outlet openings.

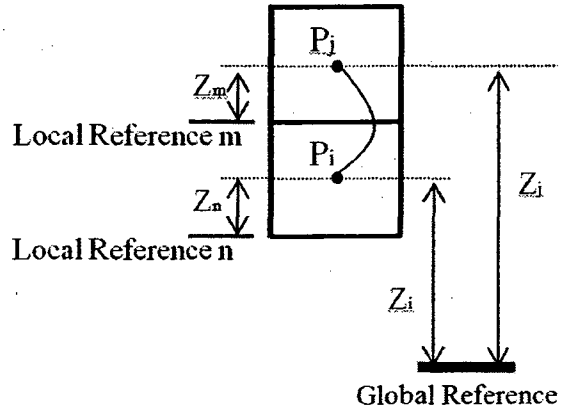

Figure 3.3: Two pressure zones and the relation with local and reference heights

3.2 Thermal Modeling

To handle the dynamic interactions occurring within the DSF system a numerical approach has been applied. This method is transient and takes into account the thermal mass of components. In this method, also called control-volume method, the DSF is assumed to be divided into a number of independent façades and each façade is in turn divided vertically into a number of zones, which are only coupled due to the presence of the air channel. One dimensional conduction heat transfer is assumed between these independent vertical façade layers. This approach, between a one-dimensional and a two-dimensional model, has proved to be a good compromise between accuracy (compared with the experimental results) and computing time (Faggembauu et al. 2003). More resolution may be obtained considering more discretization in vertical and horizontal directions.

In this study, for solid materials, all the thermo-physical dependencies were ignored; however, for air, dependencies of conductivity, density and heat capacity at each time step were considered but its hygro-thermal properties, e.g. moisture content, were ignored due to lack of measured data. Corner and thermal bridge effects were ignored as well.

3.2.1 Transient Heat Conduction within Single Layers of Façade

If we consider a homogeneous, isotropic element of façade with thickness defined by $0 < x < L$ then at time t, temperature T(x,t) and heat flux q(x,t) are defined as (Clarke, 2001):

$$\frac{\partial T(x,t)}{\partial x} = -\frac{1}{k} q(x,t) \tag{3.16}$$

$$\frac{\partial q(x,t)}{\partial x} = -\rho C \frac{\partial T(x,t)}{\partial x} \tag{3.17}$$

Applying conservation of energy along with above equations to an elemental volume of façade (figure 3.4) we have (Clarke, 2001):

$$\frac{\partial^2 T(x,t)}{\partial x^2} = \frac{1}{\alpha} \cdot \frac{\partial T(x,t)}{\partial t} - \frac{q_I}{k} \tag{3.18}$$

where α is the thermal diffusivity (m^2s^{-1}) and q_I is the internal heat generation (W). The above equation shows thermal distribution across the elemental volume of façade as function of time. To achieve this, first the partial differential equation needs to be solved. Two approaches to solve this second order partial differential equation are numerical and analytical solutions.

In this study, the approach to solve transient conduction is the Crank-Nicolson formulation. There are three general cases that can be written for transient conduction of an elemental volume of façade in terms of energy flow paths when preselecting thermal nodes.

1) Assume an elemental volume of façade and node I at the center of the layer (figure 3.4). The distance between I-n and I+n is the thickness of material (x). Applying Crank-Nicolson on node I to find temperature at time T (I , t+Δt) we have:

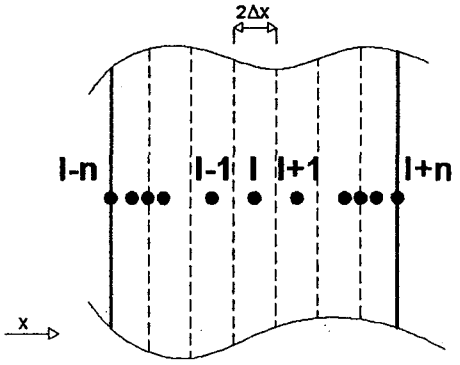

Figure 3.4: Elemental area of façade with nodes for transient conduction. Node I is located at the middle of façade.

(3.19)

$$\left[2\rho_I(t+\Delta t)C_I(t+\Delta t)+\frac{2\Delta t\,k(t+\Delta t)}{\Delta x_I^2}\right]T(I,t+\Delta t)-\left[\frac{\Delta t\,k(t+\Delta t)}{\Delta x_I^2}\right]T(I-1,t+\Delta t)-$$
$$\left[\frac{\Delta t\,k(t+\Delta t)}{\Delta x_I^2}\right]T(I+1,t+\Delta t)-\frac{\Delta t q_I(t+\Delta t)}{\Delta x_I A_I}=$$
$$\left[2\rho_I(t)\,C_I(t)-\frac{2\Delta t\,k(t)}{\Delta x_I^2}\right]T(I,t)+\left[\frac{\Delta t\,k(t)}{\Delta x_I^2}\right]T(I-1,t)+\left[\frac{\Delta t\,k(t)}{\Delta x_I^2}\right]T(I+1,t)+\frac{\Delta t q_I(t)}{\Delta x_I A_I}$$

Where q_I is the energy generation within control volume and equal to zero.

2) Now consider node I is located at the exposed surface of an elemental area of façade (figure 3.5). Applying conservation of energy along with equations (3.16-3.17) to node I and using Crank-Nicolson, we can find T(I , t+Δt):

Where,

q_I is the energy generation within control volume;

q_s is the short-wave energy absorption;

q_L is the long-wave energy exchange with surroundings (S1, …, Sn);

q_R is the casual heat gains;

q_C is the convection heat transfer.

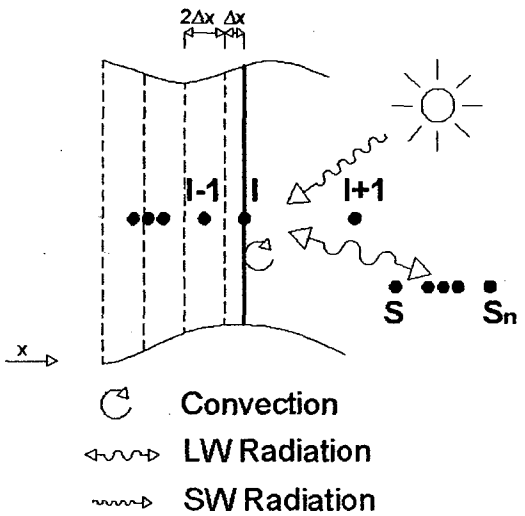

Figure 3.5: Elemental area of façade with nodes for transient conduction. Node I is located at the exposed surface of façade and it is interacting with other energy flow paths including convection, LW radiation and SW radiation.

$2\Delta x_I$ is the distance between nodes I-1 and I. h_{rs} is the long-wave radiation coefficient between node I and sky, ground and surroundings. A_I is the cross-section area at node I and for an elemental volume of façade A_I is equal to unity. q_i is zero.

$$\left[2\rho_I(t+\Delta t)\,C_I(t+\Delta t)+\frac{\Delta t\,k(t+\Delta t)}{\Delta x_I^2}+\frac{\Delta t\,h_c(t+\Delta t)}{\Delta x_I}+\frac{\Delta t\sum_{s=1}^{n}h_{r_s}(t+\Delta t)}{\Delta x_I}\right]T(I,t+\Delta t)-$$

$$\frac{\Delta t\,k(t+\Delta t)}{\Delta x_I^2}T(I-1,t+\Delta t)-\frac{\Delta t\,h_c(t+\Delta t)}{\Delta x_I}T(I+1,t+\Delta t)- \tag{3.21}$$

$$\frac{\Delta t\sum_{s=1}^{n}h_{r_s}(t+\Delta t)\,T(S,t+\Delta t)}{\Delta x_I}-\frac{\Delta t\left[q_I(t+\Delta t)+q_R(t+\Delta t)+q_S(t+\Delta t)\right]}{\Delta x_I A_I}=$$

$$\left[2\rho_I(t)\,C_I(t)-\frac{\Delta t\,k(t)}{\Delta x_I^2}-\frac{\Delta t\,h_c(t)}{\Delta x_I}-\frac{\Delta t\sum_{s=1}^{n}h_{r_s}(t)}{\Delta x_I}\right]T(I,t)+\frac{\Delta t\,k(t)}{\Delta x_I^2}T(I-1,t)+$$

$$\frac{\Delta t\,h_c(t)}{\Delta x_I}T(I+1,t)+\frac{\Delta t\sum_{s=1}^{n}h_{r_s}(t)\,T(S,t)}{\Delta x_I}+\frac{\Delta t\left[q_I(t)+q_R(t)+q_S(t)\right]}{\Delta x_I A_I}$$

3) As illustrated in figure 3.6, node I is located at the center plane of air channel, with nodes I-1 and I+1 located at the air channel boundaries. When the cavity is ventilated not only the convective heat flux between the surfaces has to be taken into account, but also the advective heat flux due to temperature differences between the air entering or leaving the domain. Then,

$$\begin{aligned}
q_V &= \rho(t)\dot{V}(t)C(t)[T(I,t)-T(I,t+\Delta t)] \\
q_{c,I-1} &= h_{c,I-1}A_{I-1}\,[T(I-1,t)-T(I,t)] \\
q_{c,I+1} &= h_{c,I+1}A_{I+1}\,[T(I+1,t)-T(I,t)] \\
q_V &= q_{c,I-1}+q_{c,I+1}
\end{aligned} \tag{3.22}$$

Where,

q_V is the advection heat transfer due to ventilation

q_c is the convection heat transfer with façade surfaces

h_c is the convection coefficient between air and exposed façade surface

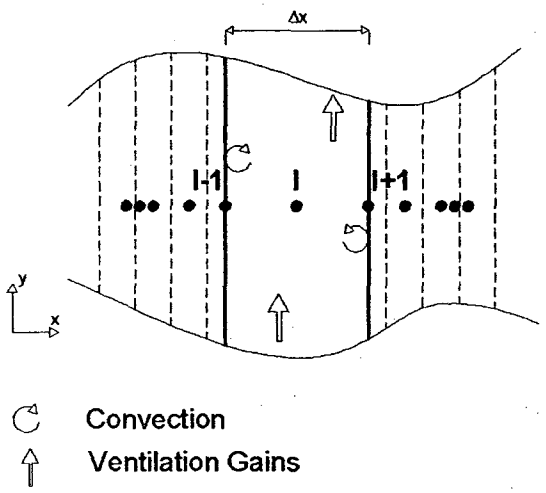

Figure 3.6: Elemental area of façade with nodes for transient conduction. Node I is located in the space between two elements of façade and it is interacting with other energy flow paths including convection, ventilation gains and casual Gains.

Again, applying Crank-Nicolson to solve above equation, we can find T(I , t+Δt),

(3.23)

$$\left[2\rho_I(t+\Delta t)\,C_I(t+\Delta t)+\frac{\Delta t\,h_{c,I-1}(t+\Delta t)}{\Delta x}+\frac{\Delta t\;h_{c,I+1}(t+\Delta t)}{\Delta x}\right]T(I,t+\Delta t)-$$

$$\left[\frac{\Delta t\,h_{c,I-1}(t+\Delta t)}{\Delta x}\right]T(I-1,t+\Delta t)-\left[\frac{\Delta t\;h_{c,I+1}(t+\Delta t)}{\Delta x}\right]T(I+1,t+\Delta t)-$$

$$\frac{\Delta t\left(q_V(t+\Delta t)\right)}{\Delta x}=$$

$$\left[2\rho_I(t+\Delta t)\,C_I(t+\Delta t)-\frac{\Delta t\,h_{c,I-1}(t)}{\Delta x}-\frac{\Delta t\;h_{c,I+1}(t)}{\Delta x}\right]T(I,t)+$$

$$\left[\frac{\Delta t\,h_{c,I-1}(t)}{\Delta x}\right]T(I-1,t)+\left[\frac{\Delta t\;h_{c,I+1}(t)}{\Delta x}\right]T(I+1,t)+\frac{\Delta t\left(q_V(t)\right)}{\Delta x}$$

3.2.2 Numerical Thermal Modeling of Façade Layers

To develop more precise numerical thermal modeling for all layers of DSF, we follow three stages:

A) System discretization,

B) Establishment of nodal equation sets,

C) Simultaneous solution for equation sets.

The degree of complexity increases as the system is discretized to smaller zones.

3.2.2.1 System Discretization

In this method, also called the control-volume method, the DSF is assumed to be divided into a number of independent façade layers (glazing1, glazing2, glazing3 & blind), and each façade is divided vertically into a number of zones, which are only coupled due to the presence of the air channel. One dimensional conduction heat transfer is assumed through these independent vertical façades. This approach that is between a one-dimensional and a two-dimensional model has proved be a good compromise between accuracy (compared with the experimental results) and computing time (Faggembauu et al., 2003). The more resolution may be obtained considering more discretization in vertical and horizontal directions.

It was assumed that each node represents a portion of the façade, attached room or air volume that is homogenous and isotropic. The thermo-physical property of the node was assumed the weighted volumetric properties of the region around the node.

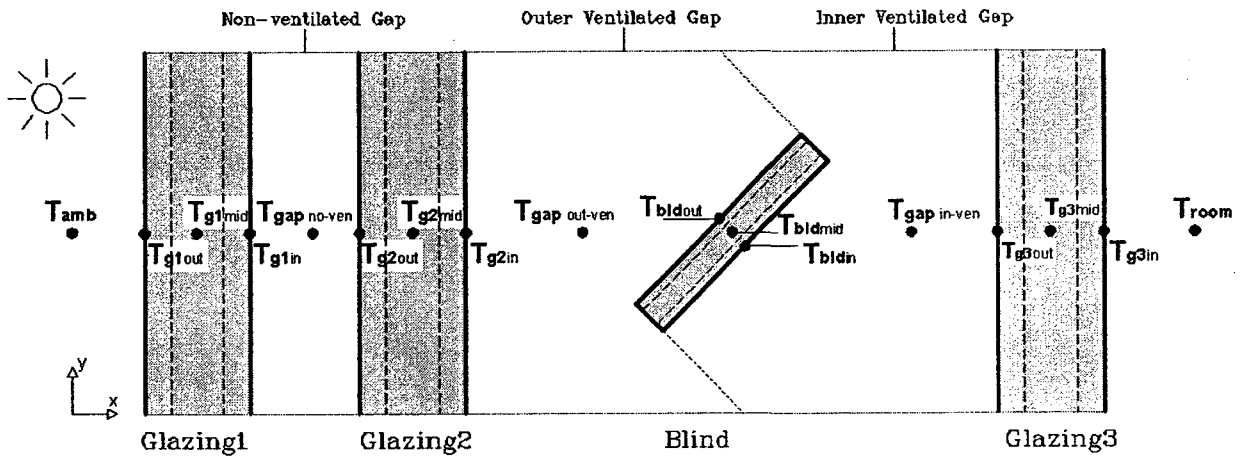

Figure 3.7: Section of façade layers showing numerical thermal nodes. The blind as a default has one internal node, based on material of blind more divisions and thermal nodes may be considered. The figure is not to scale.

3.2.2.2 Establishment of Nodal Equation Sets

For each node, in regard to surrounding nodes, one of the general cases already developed for transient conduction (equations 3.19, 3.21 or 3.23) is modified to represent the nodal condition and the inter-nodal transfer of energy. Appendix E includes the set of heat balance equations at each layer of DSF.

3.2.2.3 Simultaneous Solution of Airflow and Thermal Equations

The equation set developed in Appendix E was only for one of the vertical divisions of the double-skin façade (figure 3.7). The unidirectional transient conduction was defined with 17 nodes (12 material nodes, 3 enclosed air nodes and 2 ambient air nodes). The whole system of the double-skin façade, based on desired resolution, maybe represented

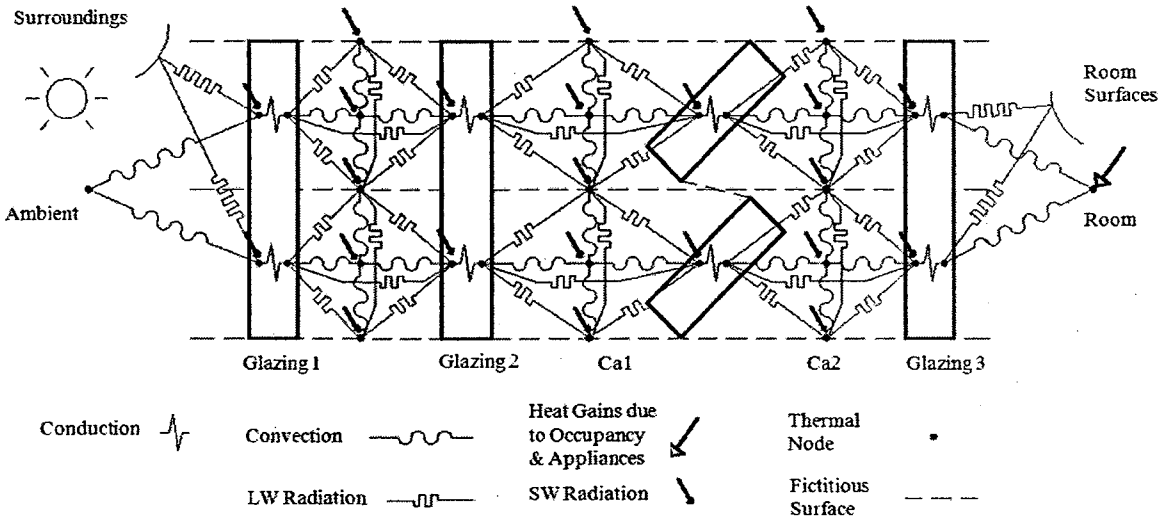

Figure 3.8: Two superimposed divisions of façade layers section showing energy paths between thermal nodes. As illustrated, the only coupling between the two superimposed divisions is through imaginary surfaces located in the air channel. For simplicity each material layer has been shown with one thermal node. For clarity energy paths interacting with imaginary surfaces between shading device slats are not shown and the figure is not to scale.

with n vertical divisions, superimposed on top of each other (then the thermal nodes representing the whole system will be $(n.15)+2$). Having only one division with 17 nodes meant solving 17 simultaneous equations, each comprising present and future time coefficients. To write the system in a matrix form,

$$A\ T(I,t+\Delta t)=B\ T(I,t)+C \tag{3.24}$$

where A and B are the coefficients matrices for future time-row and present time-row. Their numerical values normally are known. The column matrices $T(I,t+\Delta t)$ and $T(I,t)$ contain the nodal temperature terms at future and present time-rows, respectively. The column matrix C contains the known boundary conditions due to the temperature and heat flux fluctuations that can influence thermal nodes.

3.3 Conclusion

In this chapter, two numerical models, airflow and thermal, were developed. Numerical airflow modeling is based on the nodal network approach, which is capable of predicting bulk airflow. Thermal modeling is based on control volume method. The DSF is divided into a number of independent façade layers and each façade is in turn divided vertically into a number of zones, which are only coupled due to the presence of the air cavity. One- dimensional conduction heat transfer is assumed through these independent vertical façades. The temperature of the cavity's control volume is represented by a bulk temperature. It is assumed that enthalpy flows only occur in the vertical direction.

In thermal modeling, to estimate the convective heat transfer coefficient, existing relations obtained from literature are implemented. Distinction is made between natural, forced and mixed convection regimes. In most cases, the flow in one storey high double-skin can be regarded as a developing flow. For the naturally ventilated as well as the mechanically ventilated DSF, heat transfer correlations are then suggested. Appendix B discusses in detail convection coefficient used for different layers of DSF. It should be mentioned that the suggested correlations have been developed for generic cases and are not unique to DSF; this may lead to inaccuracy. Appendix C presents a procedure to find absorbed solar radiation on each layer using shape factors while considering multi-reflection and partial shading due to the shading device of DSF. The methodology also takes into account the thickness of slats while determining partial shading. The long-wave radiation is calculated by the net-radiation method in appendix D.

CHAPTER 4

MECHANICALLY-VENTILATED DSF

In this chapter, first the numerical model discussed in chapter 3 will be applied to develop a base-case model of a mechanically-ventilated double-skin façade. This is done using the building energy simulation software, ESP-r (ESRU, 1999). ESP-r is a transient heat transfer modeling program which is able to evaluate the energy performance of the building. The implementation of the base-case into ESP-r is shown in Fig 4.1. In the next step, the result of simulated base-case model is verified. This verification will be in two levels: with measured data and with inter-model comparison.

4.1 Base Case Model Development

4.1.1 Test-cell Set-up

The experimental facility used for the development and verification of base case model is a test-cell at the Department of Energy Studies, University of Politicnico di Torino, Italy. The test-cell is 2.5m high, 1.6m wide and, 3.6m long. The south facing side of the cell, which is 1.6m wide and 2.5m high, has an airflow window (supply air and exhaust both from and to indoor) with an outer double-glazed façade, and an inner single glazed façade, as shown in figure 4.2. The outer double-glazed façade, L1 and L2, is divided into three parts: upper, middle and lower. L1 and L2 are 8mm and 6mm thick clear glass, respectively. The air cavity between L1 and L2 is 15mm wide. The indoor pane, L4, is 6mm thick clear glass, which can be opened in order to make the air channel accessible.

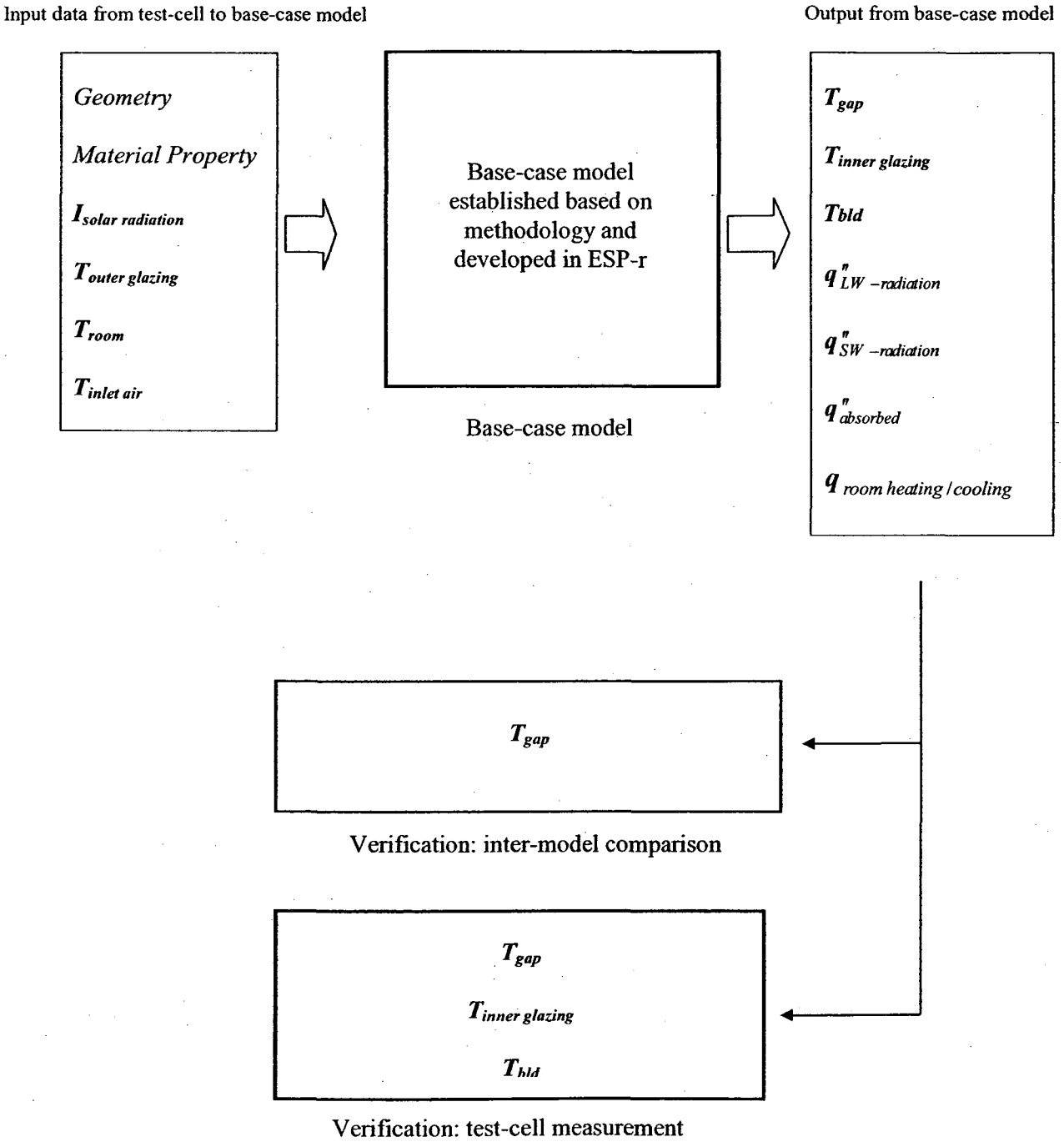

Figure 4.1: Inputs to base-case and verification of the outputs

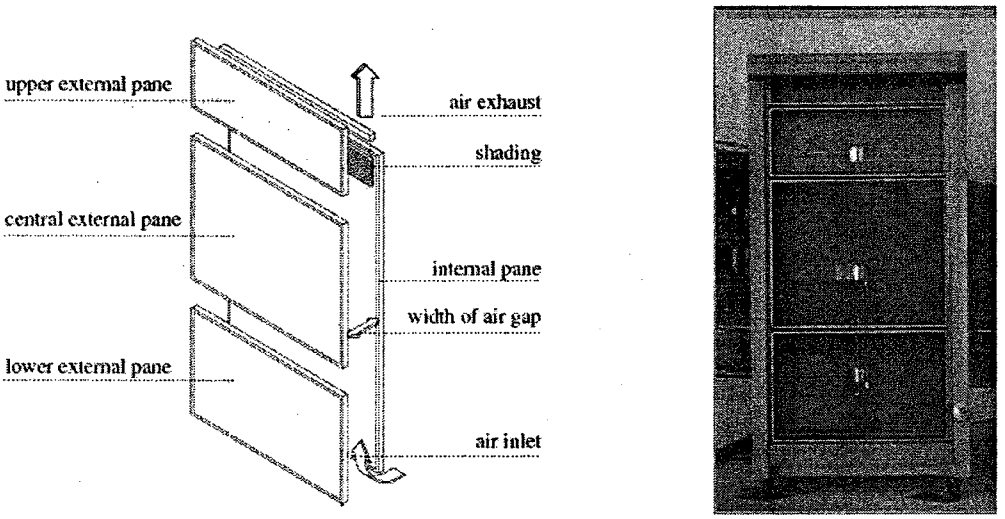

Figure 4.2: Scheme of the components of DSF

The air cavity between L2 and L4 is 14.8cm wide and can be enlarged up to 30cm. However during the measurement campaign it was kept at 15cm.

Venetian blind was installed in the air cavity between L2 and L4. The slats had small pores and were inclined at 45° from the horizontal. The air from the test cell entered into the DSF cavities through an opening located at the bottom of the DSF, which was then extracted at the top of DSF by a fan.

The test-cell was equipped with a continuous monitoring system to measure energy consumption, indoor air temperatures, heat fluxes through the façade, temperature distributions in the air channel and on the façade surfaces, and airflow rate. The sensors in the DSF system were positioned at 0.4cm, 1.35m, and 2.3m from the floor as shown in

Figure 4.3. There is no information available on the horizontal location of these sensors respect to panes. The solar radiation incident on the façade and its transmitted portion were measured by means of pyranometer, while the outdoor air temperature was obtained from a meteorological station located near the site. In this study, the measurement data of both summer and winter were used while the test cell had the configuration of airflow window with constant airflow rate. Summer cavity air flow rate was 35.2 m^3/hr and that in winter was 27.2 m^3/hr.

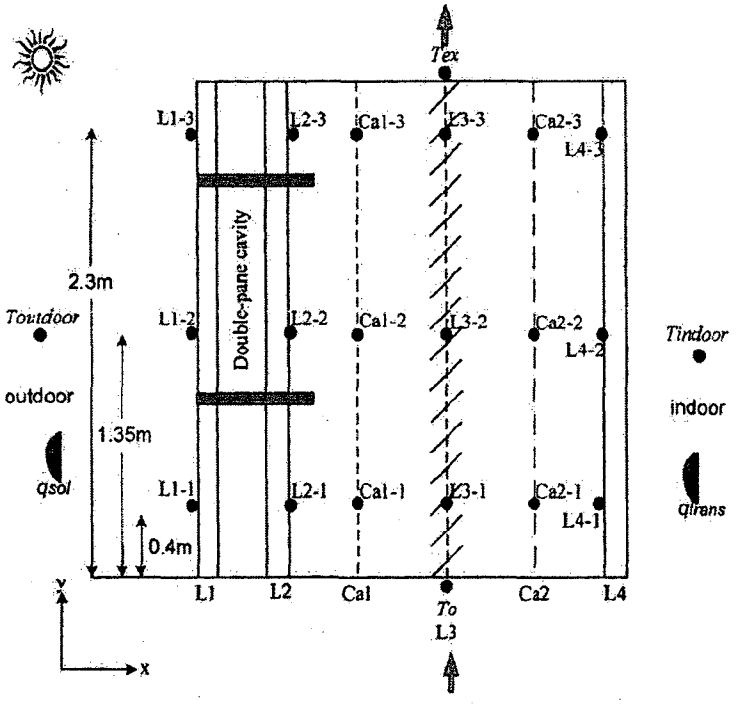

Figure 4.3: Mechanically ventilated DSF. Ll is the exterior glass of the double pane; L2 is the interior glass of the double-pane; L3 is the venetian blinds; L4 is the interior glass of the ventilated DSF; Ca_1 is the outer cavity; and Ca_2 is the inner cavity, T_o is the air temperature at the inlet, T_{ex} is the air temperature at the exit, T_{indoor} is the room air temperature, $T_{outdoor}$ is the outside air temperature, q_{sol} is the total solar radiation, q_{trans} is the transmitted solar radiation, • is thermocouple and ◖ is pyranometer. This figure was reproduced from (Jiru, 2006).

4.1.2 Developing a Base Case Model with ESP-r

The base-case model is based on the configuration of the test-cell facility (section 4.2.1) and it is a mathematical model for the purpose of studying the thermo-fluid phenomena of DSF and its attached room. This base-case model is able to predict cavity and surface temperatures of the test cell. It also determines the amount of heat transfer flux inside the test-cell and its attached room. ESP-r was utilized as a tool to simulate the base-case model and to predict the cooling/heating load and temperature distribution.

4.1.3 Setting-up ESP-r and Modeling Assumptions

4.1.3.1 Geometry

The first task to start with ESP-r was to create and define the geometry and material attribution of the base-case model, which is actually the geometry and material attribution of test-cell facility. In ESP-r, the cavity was divided vertically into four thermal zones in front and four behind the shading device (figure 4.4). Each thermal zone was enclosed by the aid of imaginary surfaces. Then the proper boundary conditions including the variation in dry bulb and surface temperatures and solar radiation, were applied at each boundary surface.

As shown in Fig. 4.1, inputs from test-cell measurements are passed directly to ESP-r at each time step. These input data include outdoor condition (incident solar radiation, exterior glazing surface temperature), indoor condition (room temperature, inlet air temperature) and total airflow rate of cavity.

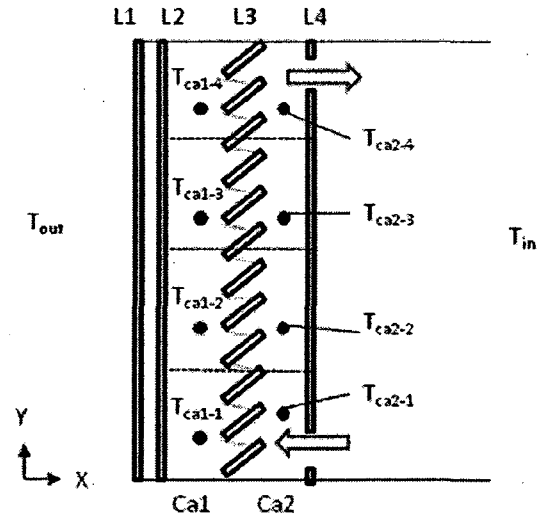

Figure 4.4: The double-skin façade has been discretized using fictitious surfaces to capture thermal stratification in cavity air. Although the test-cell has three vertical subdivisions, in the base-case model implemented to ESP-r, four vertical subdivisions were considered to achieve higher prediction resolution.

Exterior pane surface temperatures measured from the test-cell were used directly as an input for base-case model. This avoids the need to find outdoor convection and radiation heat transfer.

4.1.3.2 Material and Construction

A number of standard databases are available within ESP-r. For some simulations, a user may have to define one's own databases. In this case, the user may copy and use available ESP-r standard databases and apply the required modification, or simply start from scratch. Here, for the base-case, the databases for materials, multilayer constructions and climate were created from scratch based on set-up of the outdoor test-

cell facility. Although accurate information of thermal properties of some test-cell materials was not available, an approximation was assumed.

4.1.3.3 Climate

The simulation climate was Torino, Italy and the run-period was two days in winter and summer. Values for every 15 minute time step for 10 and 11 January and for 6 and 7 July were defined in the climate databases derived from test-cell measurements. For each 15 minute time step, the following data was held:

a. Incident solar radiation on south façade (Wm-2)

b. Dry bulb temperature of outdoor (C)

Surface Type		Layers	Thermal Conductivity ($W\ m^{-1}\ K^{-1}$)	Density ($kg\ m^{-3}$)	Specific Heat ($J\ kg^{-1}K^{-1}$)	Thickness (m)
DSF	**Outer Glazing (L1)**	clear glass + air + clear glass	1 0.024-0.027 1	2500 1.2 2500	840 1000 840	8mm 12mm 6mm
	Blind (L3)	Aluminum	100	2400	910	2mm
	Inner Glazing (L4)	clear glass	1	2500	840	6mm

Table 4.1: Thermo-physical properties of DSF's construction

4.1.3.4 Boundary Conditions

For each surface within the building, a proper boundary condition was defined. The surfaces have two sides, one facing the zone (inside) and the other connected to a boundary condition (another zone, ground, outside). They interact both radiantly and convectively with their environment. The table below shows the assumed boundary conditions for the DSF of the base case-model. The boundary conditions for outer surfaces of the attached room were considered as adiabatic.

Surface Type		Boundary Condition
DSF	Outer Pane (L1)	Surface Temperature (obtained from test-cell measurement)
	Sides	Adiabatic
	Top & Bottom	Adiabatic
	Inner Pane (L4)	Attached room set-point temperature (obtained from Test-cell measurement)

Table 4.2: Boundary conditions imposed on the surfaces of mechanically-ventilated DSF

Moreover, Saelens et al. (2003) and Perino et al. (2007) reported a discrepancy between outdoor air and inlet air temperature for the case of supply-air window and a discrepancy between indoor air and inlet air temperature for the case of airflow window. This discrepancy is caused by thermal bridge effect and may reach as high as 10 C. In order to eliminate this discrepancy here, in the base-case model, inlet temperature was used directly from test-cell measurements for each time step interval.

4.1.3.5 Imaginary Surfaces

Thermal zones in ESP-r need to be completely closed. To fulfill this requirement imaginary surfaces are used. They attempt to act as surfaces that do not influence heat flow paths, within the domain of the standard inter-zonal calculation method. A careful use of a material's physical characteristics allows this. Imaginary materials are made of a material having a

- very low thermal mass
- very low solar absorptivity
- very high emissivity

This means that solar radiation will pass through the surface largely unhindered in magnitude. Furthermore, long-wave radiation will be absorbed and transmitted readily owing to the high emissivity, low thermal mass combination.

4.4.3.6 Ventilation

Following the configuration of the test-cell facility, the base-case is a return airflow window in which air is supplied and exhausted to indoor with fan power. The air flow rate is 35.2 m^3/hr in summer and 27.2 m^3/hr in winter.

Although the base case model is mechanically ventilated and the total airflow provided by fan is constant, here the question arises of how airflow is distributed on either side of venetian blind. The answer is not straightforward and depends on slat angle, position of venetian blind inside the cavity and the type of inlet/exhaust opening. For the base case with rectangular opening and venetian blind which is located near interior glazing with tilt angle of 45 degrees, 75% of total airflow rate was assumed for exterior cavity (Ca1)

and 25% for interior cavity (Ca2). Parametric studies with input from the test-cell and literature (Saelens, 2001; Safer et al, 2004) both confirm this proportion. Saelens (2001) used tracer gas measurements through CFD analysis to find the approximate airflow distribution of mechanically ventilated airflow window.

Through CFD analyses Safar et al. (2004) found that the air velocity between slats of venetian blind is negligible (less than 5% of maximum air velocity in the cavity) for the case of airflow and supply-air windows. Based on this, and for the sake of simplification in this study, one dimensional airflow (y-direction) was assumed inside the air cavity.

4.1.4 Energy flows

As mentioned before, ESP-r evaluates the mass and heat balances between finite zones and each zone is regarded as well-mixed. Therefore in reality, in order to handle thermal stratification of the ventilated air cavity of the test-cell, the double-skin façade was modeled as a series of discrete smaller zones with the aid of fictitious surfaces. Higher resolution can be achieved by discretezition to smaller thermal zones.

The scope of this study is limited to the glass area of the window, and does not deal with heat flows in the frame area. Wherever this document is referred to window, it refers to the glazing area.

4.1.4.1 Convection

The choice of algorithm for calculating the surface convection coefficient affects simulation results. ESP-r by default calculates the convection coefficient using a buoyancy-flow relation. This default is the Alamdary and Hammond correlation (Dickson, 2004). In addition, there are some predefined correlations that the user may assign to building surfaces. However, for the base-case model there was a need to imply the correlations already proposed in methodology (chapter 3). To achieve this, the source code of ESP-r was modified to include those correlations.

4.1.4.2 Solar Radiation

Modeling double-skin façade is not a trivial task and pushes many building energy simulation programs to their limitations, especially in the area of solar modeling. The most significant challenge is how the program treats direct solar radiation in internal zones; in other words, how the program calculates the solar insolation for each interior surface. With regard to external direct radiation, the incident direct beam is tracked throughout the first zone it enters until it hits an internal surface. At this point it is absorbed, reflected or transmitted. However, if the direct beam is transmitted or reflected to an adjacent zone, the directionality is lost and it is treated as diffused radiation. Therefore, it is not possible to use ray-tracing to determine insolated surfaces (Dickson, 2004). In order to overcome this pitfall, the algorithm proposed in chapter 3 was implemented into source code of ESP-r to accurately calculate insolation for interior surfaces.

4.2 Base-case Model Verification: Test-cell Measurement

The verification of the numerical model aims to give an indication of how close the modeling predictions are to measured data or other modeling method results and where the limitation and pitfalls of the base-case model are. The verification process is carried out at two levels. First, verification with test-cell measured data is performed in this section; inter-model comparison will be discussed in the next section.

Two sets of verifications with test-cell measurement were performed: Spatial distribution verification and time-variant distribution verification. The first one verifies the temperature distribution vertically and horizontally and the second one verifies temperature variation as a function of time.

4.2.1 Spatial Distribution Verification

This comparison includes verification of glazing temperatures (L1, L2, and L4), shading device temperature (L3) and the temperature of ventilated cavities (Ca1, Ca2). Horizontal temperature distribution has been presented in figures 4.5 & 4.8 for daytime and nighttime in summer and winter. At midday, high solar radiation will irradiate on DSF and increases the temperature of the glazing. Although exterior glazing receives the highest solar radiation, the shading device will have the highest temperature due to its solar absorptance. The absorbed thermal energy inside the DSF will be dissipated to air cavity (Ca1, Ca2) and glazing by convection and radiation. Therefore, in middle of the day, the shading device and exterior glazing will have the highest temperature. Air cavities exposed to these hot surfaces, by convection heat transfer, present a lower

temperature. The exterior cavity (Ca1) has a higher temperature than the interior (Ca2). At nighttime, in the absence of the sun, outdoor air temperature is lower than the room set point temperature and the ventilation air in the cavity loses thermal energy to cooler exterior glazing. As a result, room side cavity is warmer than exterior side cavity. Figures 4.5 & 4.8 confirm this observation.

There is less agreement between simulation and measurement data at daytime compared with nighttime. The lesser agreement during daytime is caused by the increased complexity of the simulation. At daytime, there are more input parameters which increase the uncertainty: the solar radiation distribution on the surfaces and the angular dependency of the glass and shading device. The more solar radiation incident on Ca1 causes more uncertain prediction of its irradiated portion than Ca2. However, these two are not the only influential factors, and the approximate convection coefficient also contributes to this uncertain prediction. At nighttime, the complexity of solar radiation calculation doesn't exist; however, the approximate convection coefficient still causes some slight discrepancies with measurement data.

A comparison between simulated and measurement vertical temperature distribution is presented in figures 4.6 & 4.7 for daytime and nighttime in summer and 4.8 & 4.9 7 for daytime and nighttime in winter, respectively. Figure 4.6-A & 4.9-A show that glazing and shading device temperatures at 3PM on a summer day (July 6) and a winter day (January 11). Generally, the temperatures are increasing vertically. This is because ventilation air has a higher temperature on the upper part of cavity. The increase of temperature on one hand and high solar radiation at 3PM on the other hand escalate

uncertainties about angular solar properties and the convection coefficient prediction, thus there is always some underestimation in simulation on the upper part of DSF at high solar radiation. In addition to this underestimation, the shading device simulation on the middle and lower part overestimate the measured value. These regions are among those regions that cannot be accurately predicted by ESP-r. Therefore, the simulated result overestimates the temperature of the lower and middle part of the shading device.

Figure 4.6-B shows that there is good agreement between simulated and measurement values. This agreement is less in figure 4.9-B due to increased temperature gradient between outdoor air and room air.

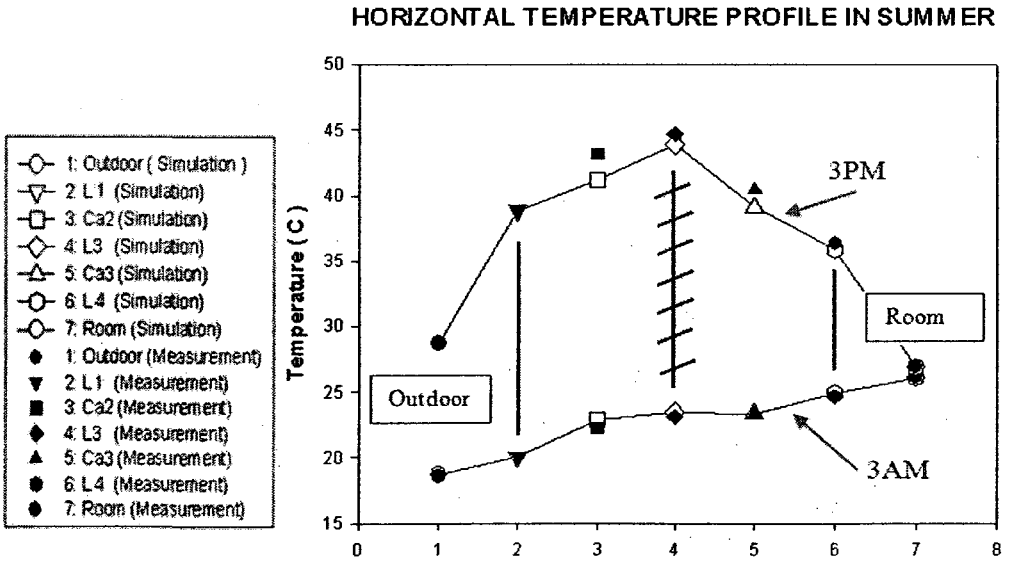

Figure 4.5: Horizontal temperature profile of double-skin façade at a height of h=2.3m on July 6. The temperature of L1 was used as input data, so the simulation and measurement values are the same.

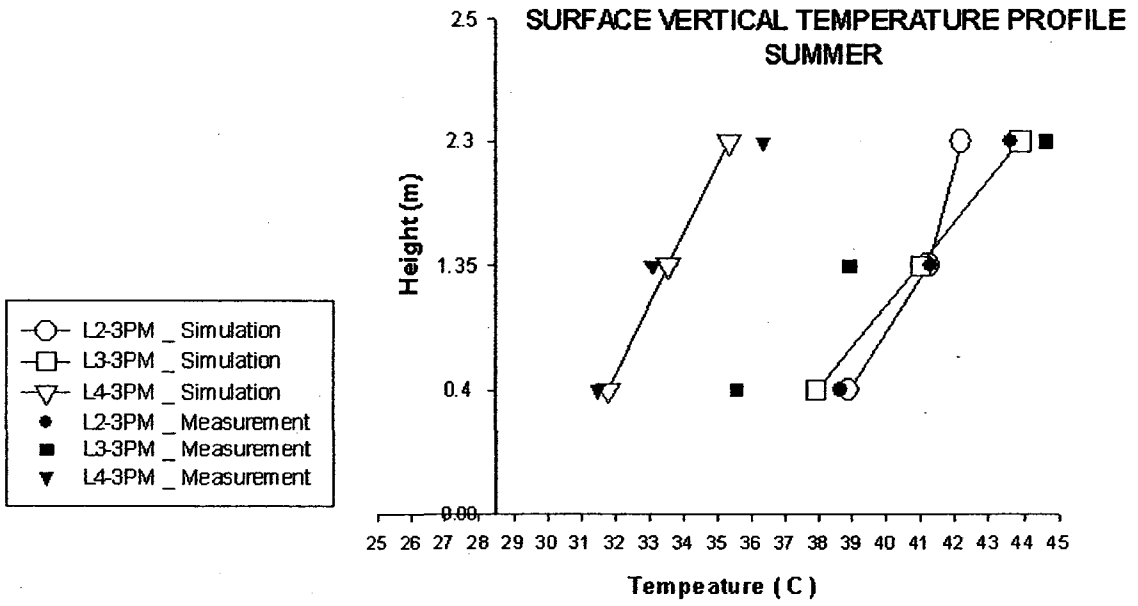

A) Surface Temperature at 3PM

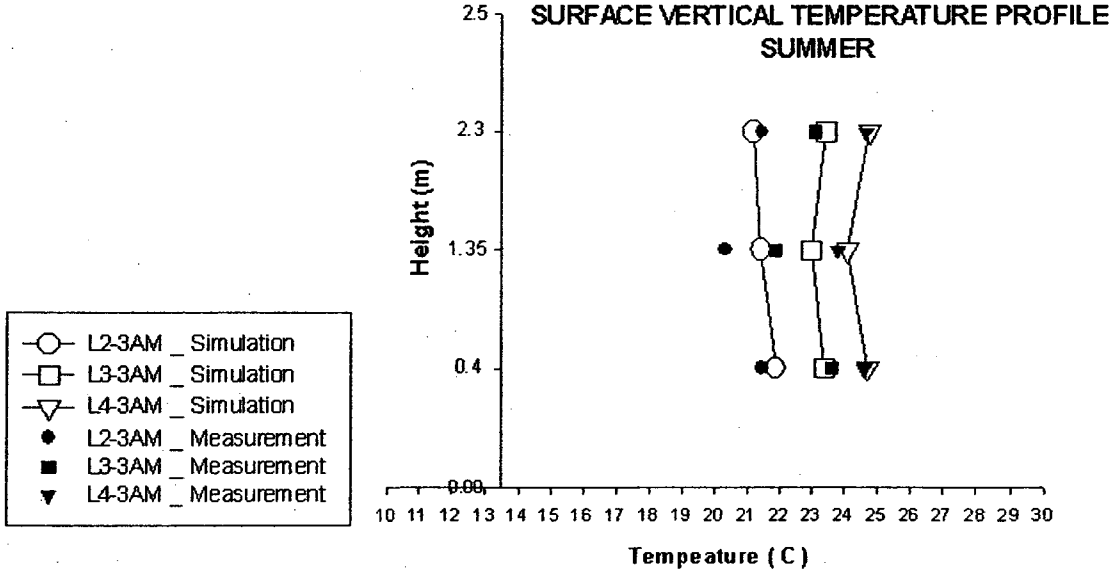

B) Surface Temperature at 3AM

Figure 4.6: Comparison of simulated vertical temperature profile of glazing and shading device with measurement at 3PM (A) and 3AM (B) on July 6.

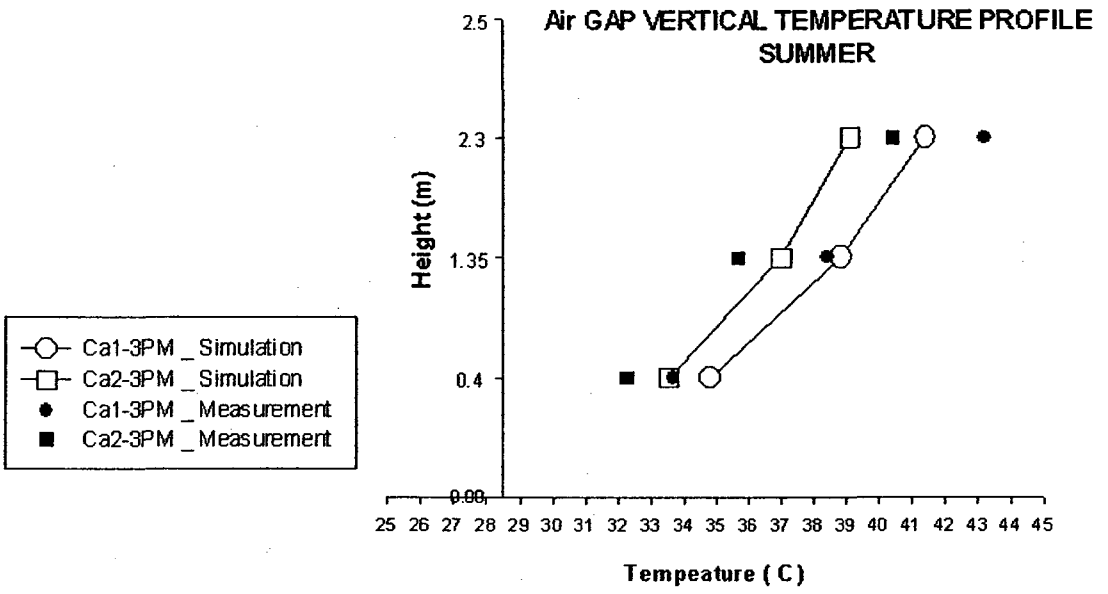

A) Cavity air temperature at 3PM

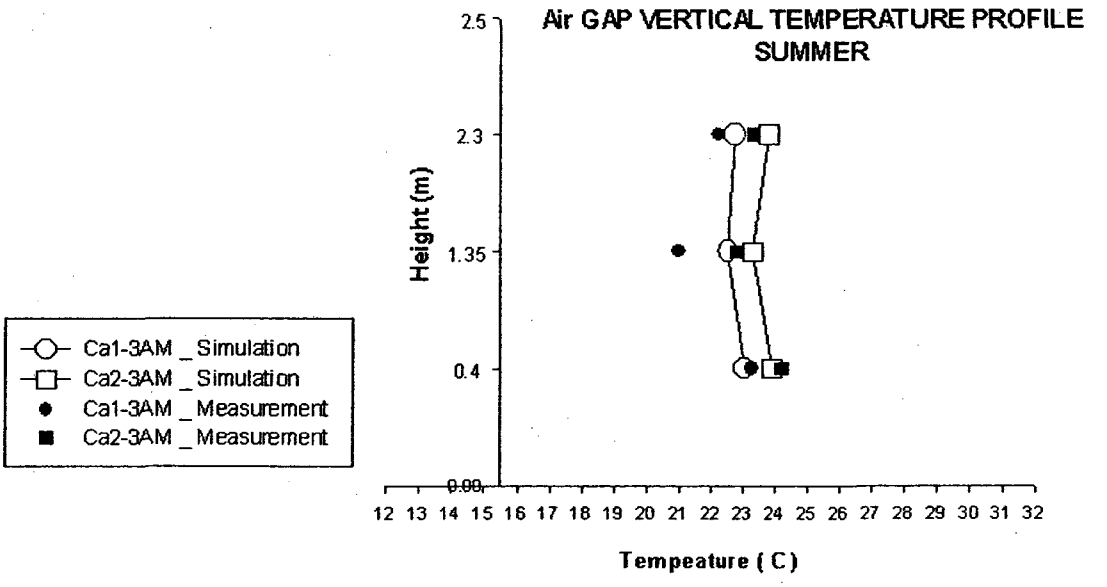

B) Cavity air temperature at 3AM

Figure 4.7: Comparison of simulated vertical temperature profile of cavities with measurement at 3PM (A) and 3AM (B) on July 6.

Specific daytime phenomena, shown both with simulated and measurement data in figures 4.6-A & 4.9-A, is that the temperature of the shading device increases so rapidly that becomes hotter than the exterior glazing. This is due to the fact that higher temperatures especially at the upper part causes the shading device to less dissipate heat than it absorbs solar radiation (less temperature difference between ventilation air and shading device surface) and decreases the rate of heat transfer with ventilation air. The high temperature of the shading device is the main reason of overheating in the attached room in summer.

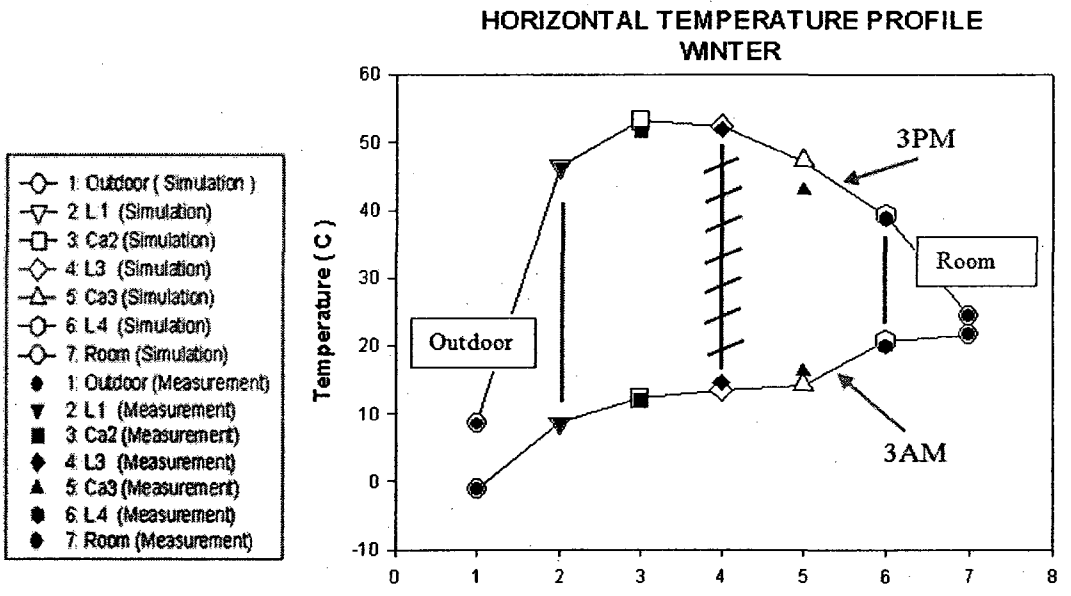

Figure 4.8: Horizontal temperature profile of double-skin façade at a height of h=2.3m on January 11. The temperature of L1 was used as input data, so the simulation and measurement values are the same.

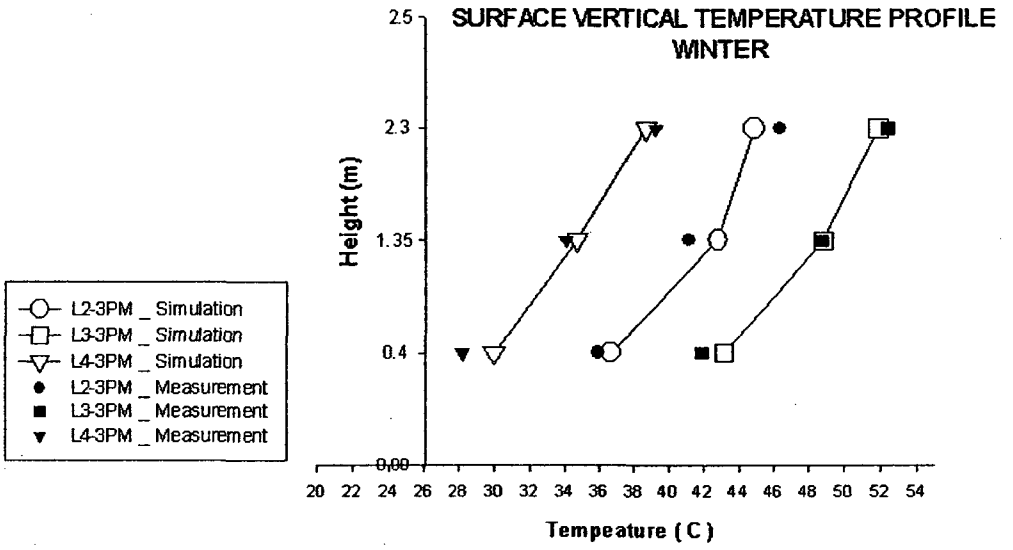

A) Surface Temperature at 3PM

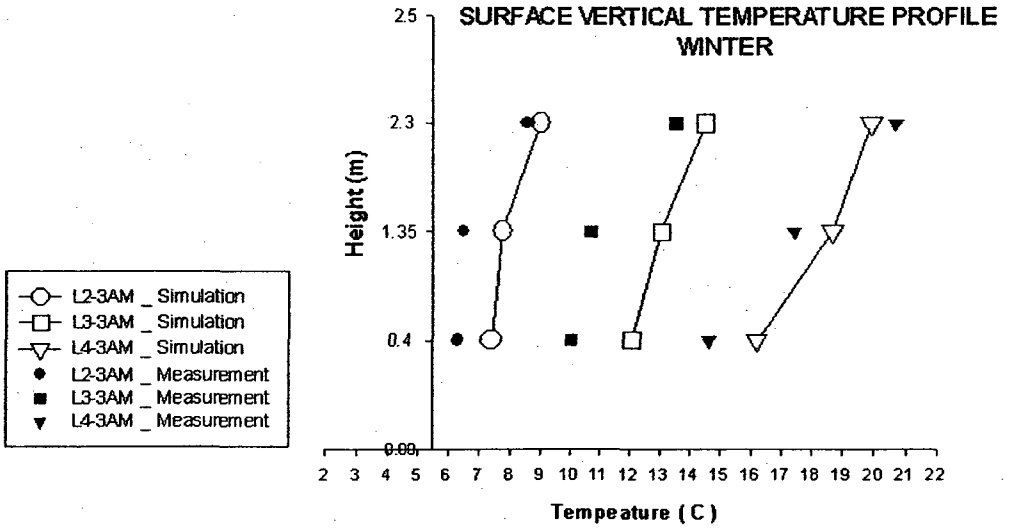

B) Surface Temperature at 3AM

Figure 4.9: Comparison of simulated vertical temperature profile of glazing and shading device with measurement at 3PM (A) and 3AM (B) on January 11.

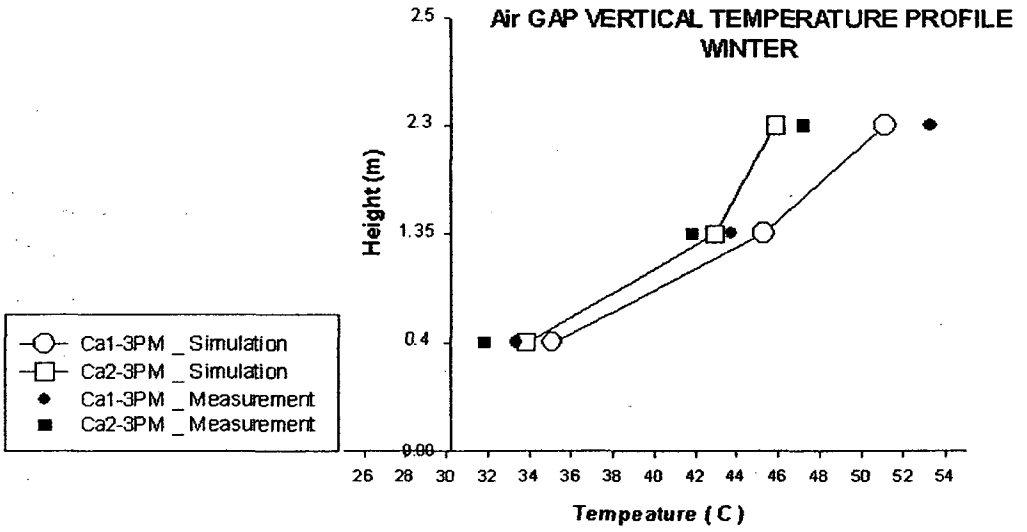

A) Cavity air temperature at 3PM

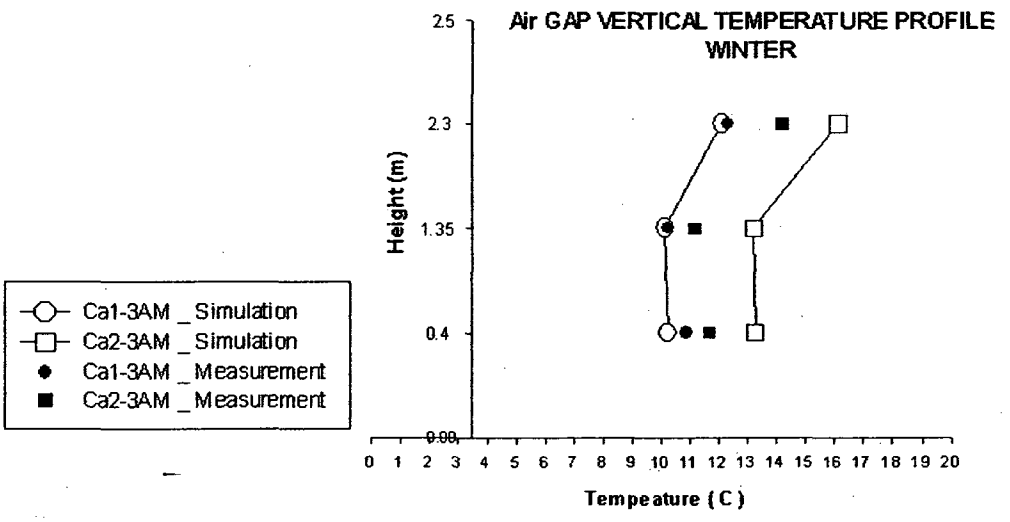

B) Cavity air temperature at 3AM

Figure 4.10: Comparison of simulated vertical temperature profile of cavities with measurement at 3PM (A) and 3AM (B) on January 11.

At daytime, air coming from the attached room is heated up through the cavity due to convection with blind and glazing. Therefore, the temperature of air increases from the lower to upper part of the DSF as shown in figures 4.7-A & 4.10-A. The exterior cavity (Ca1) has a higher temperature since it exchanges heat with hotter surfaces. Like the shading device, there are some overestimations and underestimations in simulation of cavity air.

At night, there is a trend of temperature decrease from the lower to middle part of the DSF (figures 4.7-B & 4.10-B). Cavity air loses thermal energy to the outdoors through outer glazing, and the inner cavity next to the room will have higher temperature. In winter, there is a large difference between room and outdoor temperatures, the difference between inlet and outlet temperature of DSF is more apparent.

Surface temperatures in the simulation seem to be slightly higher than measured. This can be due to uncertainties assumed for the physical properties of glazing and aluminum blind, like absorption.

Generally there is a good agreement between measured temperature and simulation. The figures present a better agreement during nighttime than daytime.

The main temperature distribution, however, is fairly well predicted. The surface temperatures have been predicted within a range of ±1.8K of measured values in summer. This range is ±2.3K in winter.

4.2.2 Time-variant Distribution Verification

In this section, time-variant temperature distribution over the duration of one day (April 23) is compared with measured data. The airflow rate is a known value, of 54.2 m^3/hr. Figure 4.11 compares measured and simulated cavity temperatures (T_{ca1}, T_{ca2}). During the night the average temperatures coincide very well with the measurements. During the day, there are some deviations. When the façade starts to warm up, the simulation underestimates the cavity temperature. This deviation increases for simulated T_{ca1} since it receives more solar radiation than the temperature of Ca2, while both are in the range of high uncertainty due to convection coefficient and angular solar radiation properties.

4.3 Base-Case Model Verification: Inter-Model Comparison

Jiru (2006) applied the zonal approach for the prediction of temperature distribution of the same test-cell and obtained a good agreement with experimental data. Here, the results from the zonal model and simulation of base-case are shown to have a comparison (figure 4.12 and 4.13).

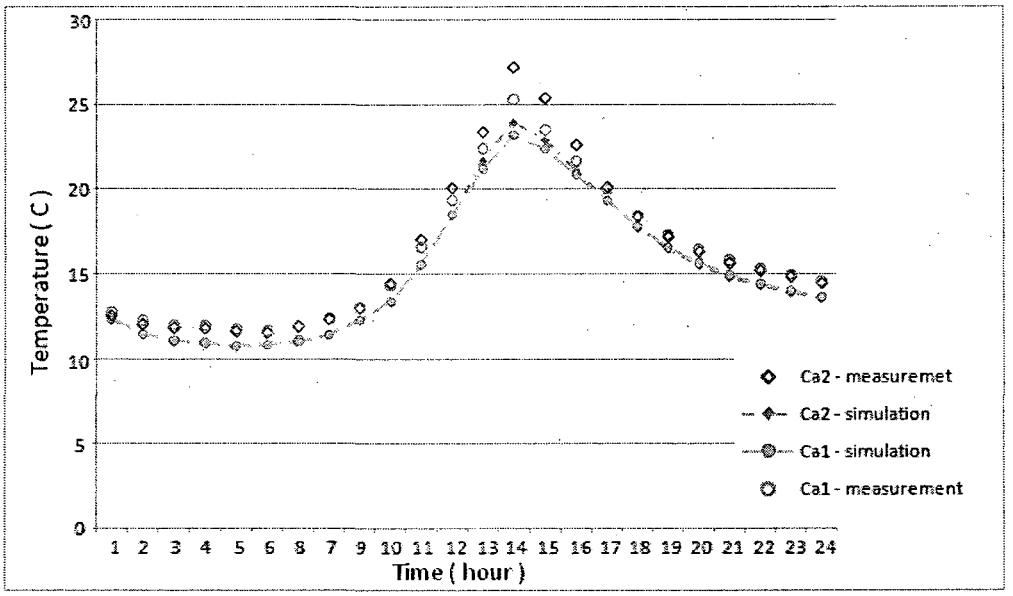

Figure 4.11: Temporal temperature distributions of ventilated cavity

It is apparent that base-case model predicts temperature distribution very close to the zonal model's prediction. Both models show better agreement during nighttime than daytime. However, at mid-day, base-case modeling underestimates the measurements while zonal model overestimates (figure 4.13).

There is a good agreement for the middle zone for both simulations; however, both simulations show considerable discrepancy at the peak temperature for the other two zones.

4.4 Conclusion

A base-case model for mechanically-ventilated airflow window configuration was developed using building energy simulation software (ESP-r). The base case model actually mimics the set-up of an outdoor test-cell facility located at University of Politecnico di Torino, Italy. The test-cell is mechanically ventilated and is equipped with data acquisition system to record its thermal performance under outdoor operating conditions. Verification was carried out at two levels: with measured data and with inter-model comparison. Verification of modeling with measurement states generally a good agreement especially at nighttime. Inter-model comparison with the zonal model also showed good agreement. The discrepancy between the two models increases with high solar radiation.

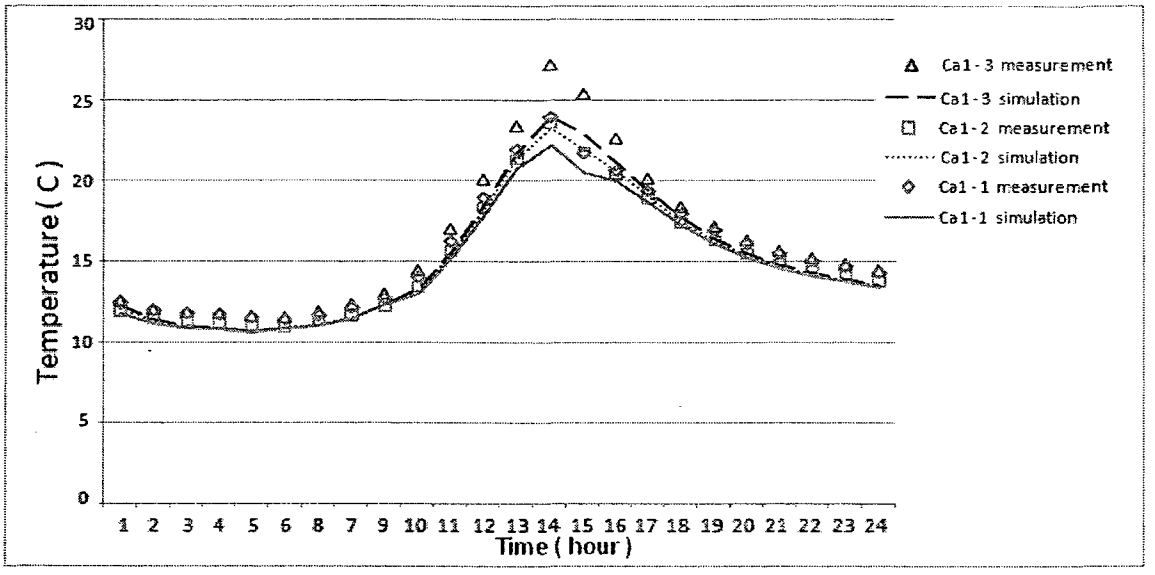

Figure 4.12-a: Hourly-averaged measurement and current simulation results for exterior cavity air Ca1

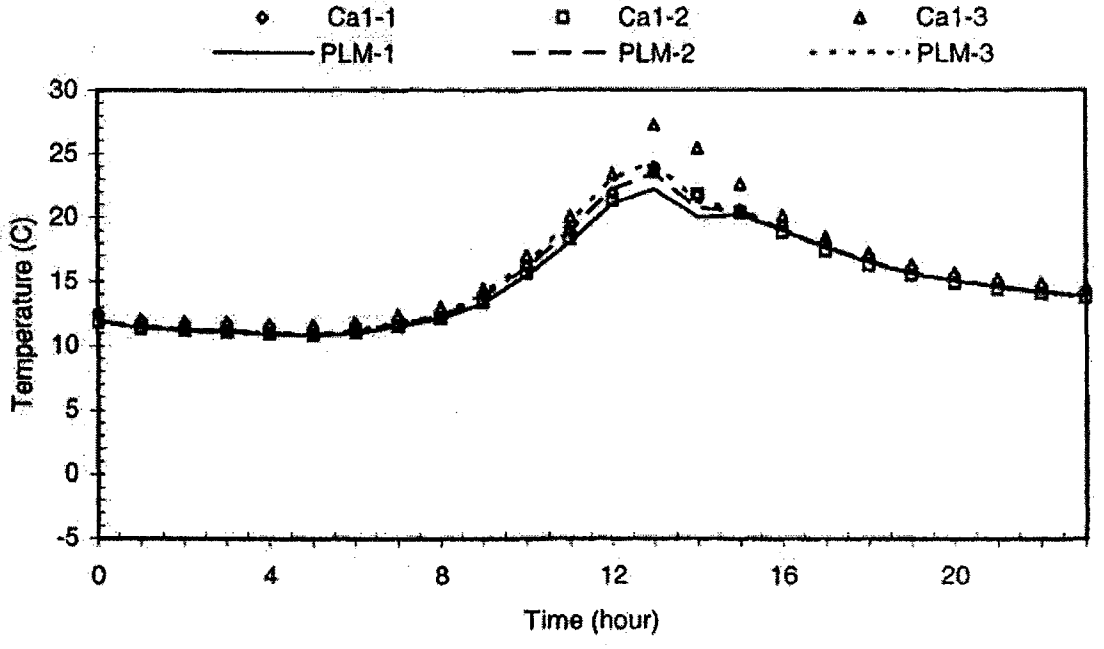

Figure 4.12-b: Measurement and zonal approach results for exterior cavity Ca1.Ca-1, Ca1-2 & Ca1-3 are measured temperatures at three different heights (Reproduced from Jiru, 2006).

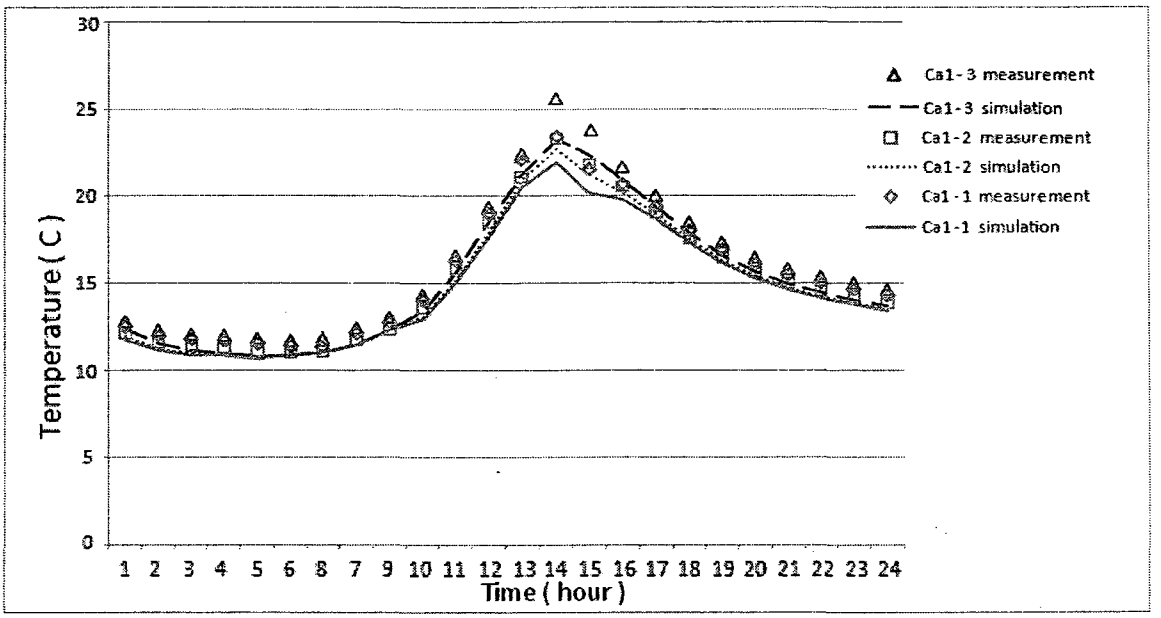

Figure 4.13-a: Hourly averaged measurement and current simulation results for interior cavity air Ca2

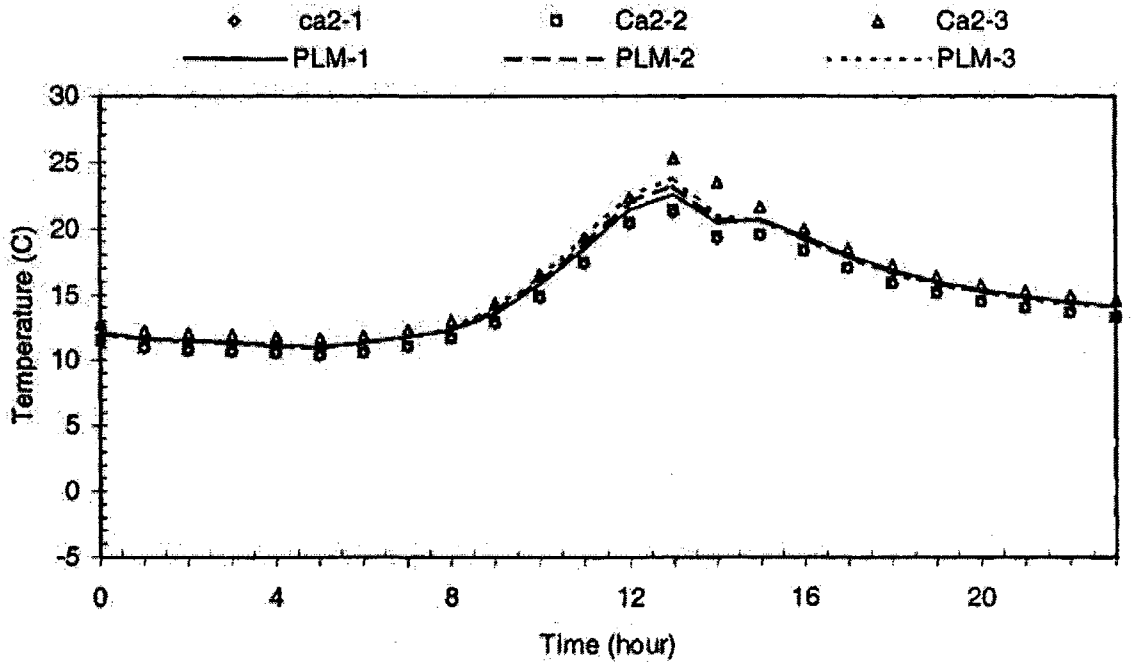

Figure 4.13-b: Measurement and zonal approach results for interior cavity Ca2. Ca-1, Ca1-2 & Ca1-3 are measured temperatures at three different heights (Reproduced from Jiru, 2006).

CHAPTER 5
NATURALLY-VENTILATED DSF

External air circulation DSF is a common type of naturally-ventilated DSF. In this chapter, an external air circulation double-skin façade was chosen as base-case configuration for the study of naturally-ventilated DSF.

In this chapter, first a base-case model for a naturally-ventilated DSF (external air circulation) will be developed using building energy simulation software. This base-case, compared with the one developed in the previous chapter, includes airflow model. Therefore, it is capable of predicting both the airflow rate inside the air channel and thermal distribution of DSF. Next, the simulation results of the base-case model will be verified with experimental data. Finally, a sensitivity analysis will be performed to figure out the severity of errors due to sources of uncertainties in base-case modeling. All these stages for the naturally-ventilated base-case model are shown in figure 5.1.

5.1 Test-Cell Set-Up

To investigate the combined heat transfer and airflow in naturally-ventilated DSF, the measurement data from an outdoor test facility located at Technical University of Munich was used. It is an external air circulation DSF (air is supplied and exhausted from and to outside) oriented southward with dimension of 2.35m high, 0.9m wide and 0.6m deep.

The outer pane is single glazing and inner double glazing. The room attached to the DSF has a depth of 3.1m. Aluminum venetian blind were installed in the channel between two panes 47cm from the inner pane. The tilt angle was 45 degrees and fixed through the experiment. The width of the shading device slats is 8cm.

Thermal and airflow characteristics are measured in the DSF with a monitoring system. The sensors are positioned at three levels in the air channel of the DSF in addition to the upper and lower dampers' sensors. The sensors are positioned at 10cm over the lower damper, 10cm below the upper damper and at the mid-height of DSF. The outdoor air enters air channel through the lower damper and exits from the upper damper by natural ventilation. Depending on wind conditions, it is possible that the flow direction reverses.

Surface temperatures were measured by PT 100 sensors and air temperatures by sheath thermocouples. For the measurement of air velocity, hotwire anemometers were applied in the air channel. Solar radiation was quantified both in front of the DSF and in the room. Ambient weather conditions (air conditions, wind velocity and direction) were measured (Artmann et al., 2004).

At each of the three levels, several sensors distributed in a horizontal plane are required to show the average velocity at that height. A study by Von Grabe (2002) stated that major errors may occur by assuming symmetric velocity profiles having the highest velocity at the centre (like pipes) for a naturally-ventilated DSF.

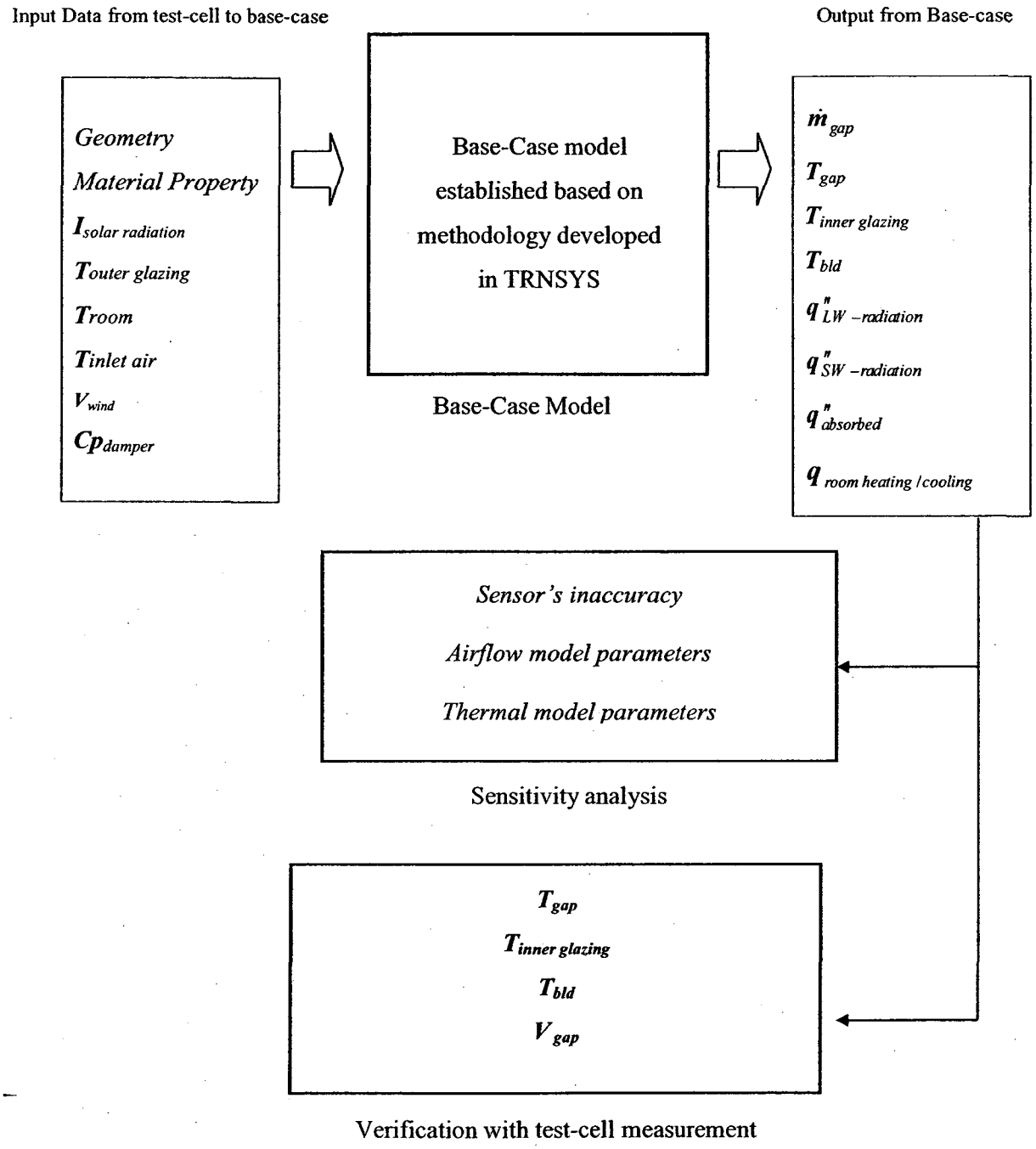

Figure 5.1: Naturally-ventilated DSF base-case model: implementation to TRNSYS, verification with measurement data and sensitivity analysis.

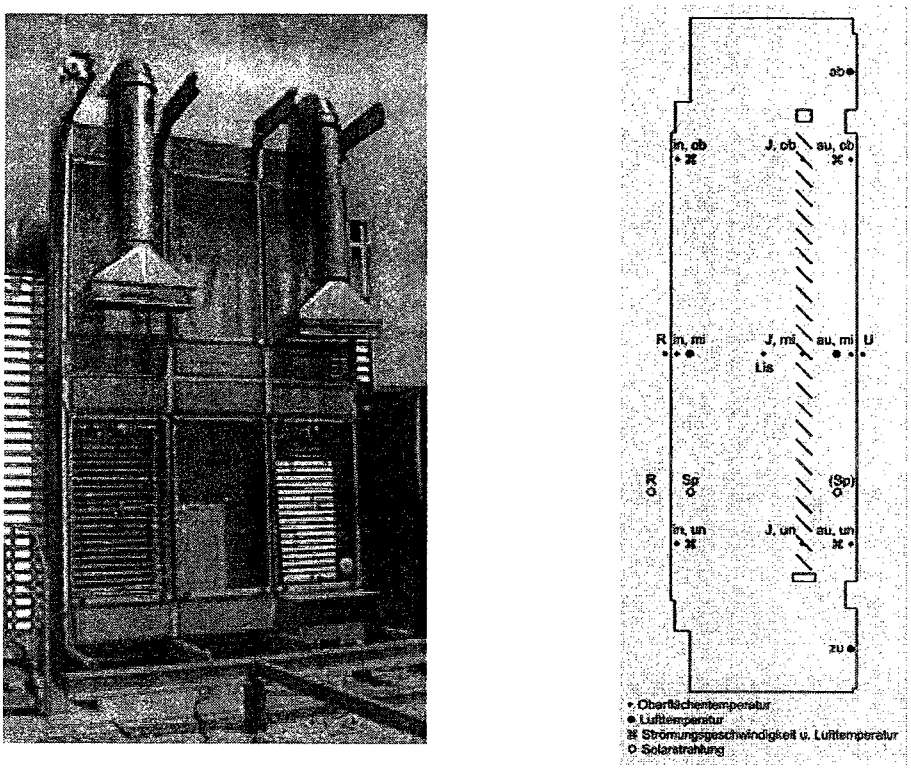

Figure 5.2-a: (Left) South-facing facade testing facilities for experimental investigation at Technical University of Munich. It includes stationary and variable testing façade. (Right) the section of stationary façade which was applied in this study with the position of sensors. The outer cavity has a depth of 13cm and inner 47cm. The tilt angle of venetian blind is fixed at 45 during experiment. (Reproduced from Artmann, 2004).

This is because in a naturally-ventilated DSF the driving force is the reduction of the density due to the increase of air temperature. This increase is greater near the heat sources, thus near the glazing and the shading device. In the current case, there is just one sensor at each level, but as the measurement shows, the mean deviation between blind surfaces and interior/exterior glazing are less than 3C, which may reduce the need of multiple sensors; also the asymmetric velocity profile can be closer to a symmetric profile, especially in turbulent domain.

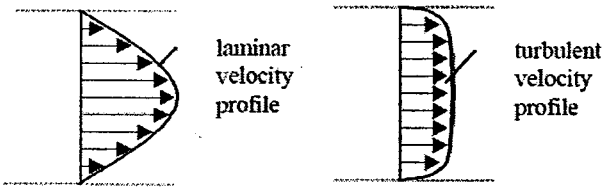

Figure 5.2-b: Velocity profile for forced laminar and turbulent flow in pipe (Reproduced from Von Grabe J, 2002).

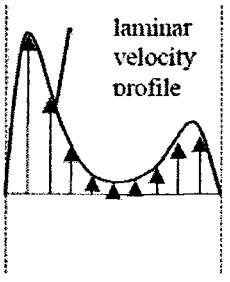

Figure 5.2-c: Possible laminar velocity profile for natural ventilation between glazing and shading device. (Reproduced from Von Grabe J, 2002).

The prediction of velocity profile can be complicated when wind effect is also taken into account. As it will be explained in section 5.3 in this study the wind effect is insignificant and ventilation is largely due to stack effect. Thus, the effect of wind on the velocity profile inside the air channel is minor.

Moreover, it should be noted that the hot-wire anemometers do not determine the flow direction and the estimation of the air flow rate in the cavity is suitable only if there are no changes in flow direction within the profile. However, as Artmann et al. (2004) showed, there are vortices existing in air channel and therefore unidirectional airflow assumption can lead to inaccuracy of the estimated airflow in the DSF cavity.

5.2 Developing Base Case Model and Assumptions

The base-case model is capable of predicting cavity and surface temperatures plus the airflow rate of the test-cell. The prediction of airflow rate is restricted to bulk flow motion; a detailed pattern of air movement is not the aim of this modeling. The bulk flow information is sufficient for a base-case thermal model to predict temperature profiles with desired accuracy. Moreover, heat flux inside the DSF and the energy needs of the attached room to keep room temperature at set point are obtainable with the base-case model.

5.2.1 Geometry

The base-case model is composed of eleven zones, separated by glazing or imaginary surfaces. The DSF itself is subdivided into four zones in front, four zones behind the shading device and two zones for the upper/lower dampers. One zone is also assigned for the attached room. Each zone is assumed to be well-mixed and its bulk temperature is represented by one temperature. The division of zones in the DSF is achieved by using imaginary surfaces which have negligible influence on energy flow paths (chapter 4). Figure 5.3 shows the base-case model geometry and divided zones with imaginary surfaces.

The boundaries of the DSF consist of the inside and outside panes, and the top, bottom and side of the cavity. The ventilation inlet and outlet dampers are placed in the lower and upper part of the cavity, respectively. Table 5.1 shows the assigned boundary condition for DSF surfaces.

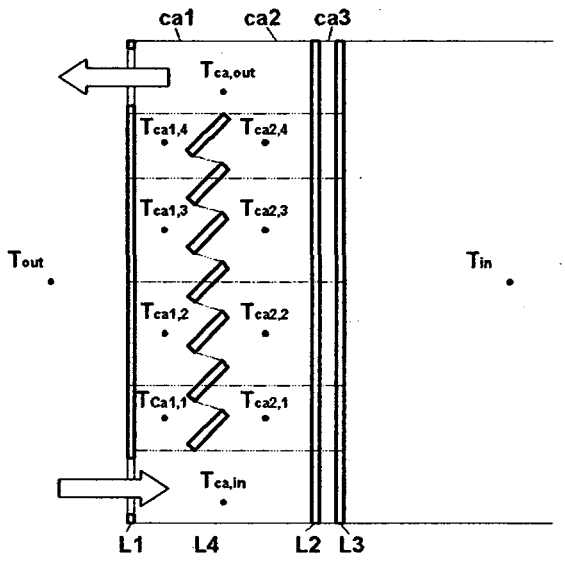

Figure 5.3: Subdivided thermal zones of a naturally-ventilated DSF. Each zone has been represented with one thermal node.

The surface temperature of outer pane is known in advance via measurements of the test-cell, so it is possible to impose this known boundary condition on the outer pane. The air temperatures at the outdoor and attached room are also known boundary conditions.

Surface Type		**Boundary Condition**
DSF	**Outer Glazing**	Surface Temperature (obtained from Test-cell measurement)
	Sides	Adiabatic
	Top & Bottom	Adiabatic
	Inner Glazing	Attached room set-point temperature

Table 5.1: Boundary conditions imposed on the surfaces of naturally-ventilated DSF

It was assumed that the effects of spacers or frames separating the panes are negligible and the heat flows through the bottom, top and sides are expected to be small as compared with the heat flows through the panes. On the top, bottom and sides therefore, adiabatic wall boundary conditions are imposed.

5.2.2 Climate

The simulation climate was Munich, Germany and measurement data was available for two days in winter and summer. The first day was simulated as start-up and the second day represented the base-case modeling result. Like the mechanically-ventilated base-case, the time step was 15 minutes per hour. This following information was provided at each time-step:

a. Global vertical incident solar radiation on south façade (Wm^{-2})

b. Outdoor dry bulb temperature (C)

c. Wind velocity (m/s) and direction (degree)

5.2.3 Ventilation

The base-case has the configuration of an external air circulation DSF, so the air comes from outside, and passes through the air channel naturally, and exhausts to outside. To model this ventilation air based on the methodology of chapter 3, first the air channel was subdivided to eight airflow zones represented with eight internal pressure nodes plus two boundary nodes (figure 5.6-a). This way, the value measured with each thermocouple could be considered as a temperature boundary condition of respected airflow zone. However, as it will be discussed in verification section, the airflow modeling did not

predict the measured airflow rate of test-cell with reasonable accuracy. The reason was that the thermocouples were actually not showing the well-mixed and average temperature of those virtual subdivided zones. Therefore, another subdivision of the air channel was considered. This time, the three zones in front and behind the venetian blind were merged (figure 5.6-b). However, ESP-r (version 11.4) faced some restrictions in defining such a merged airflow zone and picking up the average temperature of three different thermal nodes at each time step. In other words, in ESP-r zoning, thermal and airflow zones must coincide. Due to this restriction, and to avoid much labor effort on airflow rate analysis, CONTAM software combined with TRNSYS was utilized.

Combination of TRNSYS and CONTAM provided this possibility to have thermal zones and airflow zones which do not necessarily coincide. Figure 5.3 illustrates the subdivision of thermal zones while airflow zones are based on figure 5.6-b. The amount of flow rate for each thermal zone was determined by net incoming flow rate for the pressure node of that zone (e.g. the amount of mass flow rate assigned to zone of $T_{ca1,2}$ is equal to net incoming mass flow rate to pressure node $P_{ca1,2}$). However, in the condition that subdivisions of thermal zones and airflow zones did not coincide, the net incoming mass flow rate for P_{ca1} (figure 5.6-b) was assigned to $T_{ca1,1}$ to $T_{ca1,4}$ and similarly P_{ca2} for $T_{ca2,1}$ to $T_{ca2,4}$. This is an approximation but it gave reasonable accuracy to calculate mass flow rate of thermal zones compared with test-cell measurement data (section 5.3).

Another challenge to determine airflow rate is the boundary pressure nodes. There are two boundary pressure nodes in the current network, P_{out1} and P_{out2}. They are located next to the lower and upper dampers. They need to have known total pressure and temperature

in order for the airflow network to be calculable. Temperature is measured directly with thermocouples; however, to find total pressure (dynamic and static), two other variables, wind conditions (velocity and direction) and pressure coefficient (Cp), need to be known at each time-step. Between these two variables, the first one was measured at the test-cell facility, but the pressure coefficient was not among given data.

The results of wind tunnel experiments to find the pressure coefficient (Cp) sets for some typical exposures, as well as building length-to-width measurements can be found in the literature. In the current naturally-ventilated test-cell, due to lack of information about surrounding geometry and its nature, CFD, wind tunnel measurement or algebraic equations method could not be used. The measurement of the test-cell's airflow velocity was the only data could be applicable to determine Cp; therefore, by starting with some tabulated Cp values, the airflow results of base-case modeling were calibrated with measurement data obtained from test-cell. This was an approximation to find Cp; however, the final results of modeling were in good agreement with measurement data. To perform calibration it was necessary to avoid variable wind direction during modeling, so simulation days were chosen so that the wind direction was almost constant during that period. Section 5.3 discusses in more detail this calibration process.

5.2.4 Energy flows

5.2.4.1 Convection

As a default, TRNSYS uses the following equation to find convective heat transfer coefficient (TRNSYS 16, 2004).

$$Hc = 1.5(T_{surfvertical} - T_{airvertical})^{0.25}$$

In order to follow the correlations proposed in the methodology (chapter 3) for base-case modeling, a new component code (proforma) was written and added to standard library of TRNSYS. This code is able to find the convective coefficient of surfaces based on *Ra* or *Re* numbers at each time step. As mentioned before, the modular nature of TRNSYS gives the program tremendous flexibility, and facilitates the addition of mathematical models not included in the standard TRNSYS library. Therefore, analyzing base-case model based on user defined convection coefficient is much easier than with ESP-r.

5.2.4.2 Solar Radiation

In TRNSYS as a default, all direct solar radiation passing through a transparent surface and entering a zone is treated as diffused solar radiation and will be distributed on the zone surfaces by absorptance-weighted area ratios. To mitigate the uncertainties of solar distribution which can result in errors in base-case modeling results, the methodology proposed in chapter 3 was followed. For this purpose a new component code was developed and added to standard library of TRNSYS. This component is able to find absorbed solar radiation for each surface of the base-case model at each time-step.

5.3 Base-case Airflow Modeling Results and Calibration

The purpose of airflow modeling of the base-case is to estimate the amount of airflow rate entering into each zone during each time-step. These airflow rate values are used as an input for thermal modeling. Thermal modeling determines advection and convection heat transfer based on these values. As discussed before, the aim is not to find the airflow pattern; the applied method just gives information on bulk fluid movement.

Figure 5.4 shows the direction and velocity of the wind for a summer day. The wind direction is close to northwest during the whole day (the dashed line is 270 degrees). Figure 5.5-a shows the prediction result and compares it with the measurement. As can be concluded from this figure, there is a good agreement between base-case airflow modeling result and measurement. Table 5.3 reports the airflow rate caused by wind and stack effect separately. It states that during the simulated period a significant portion of the airflow rate is due to stack effect. Even in winter time when the wind velocity is high, the stack effect still prevails. The reason for lower wind effect is due to existence of blades (baffles) in front of the dampers, which deflect wind.

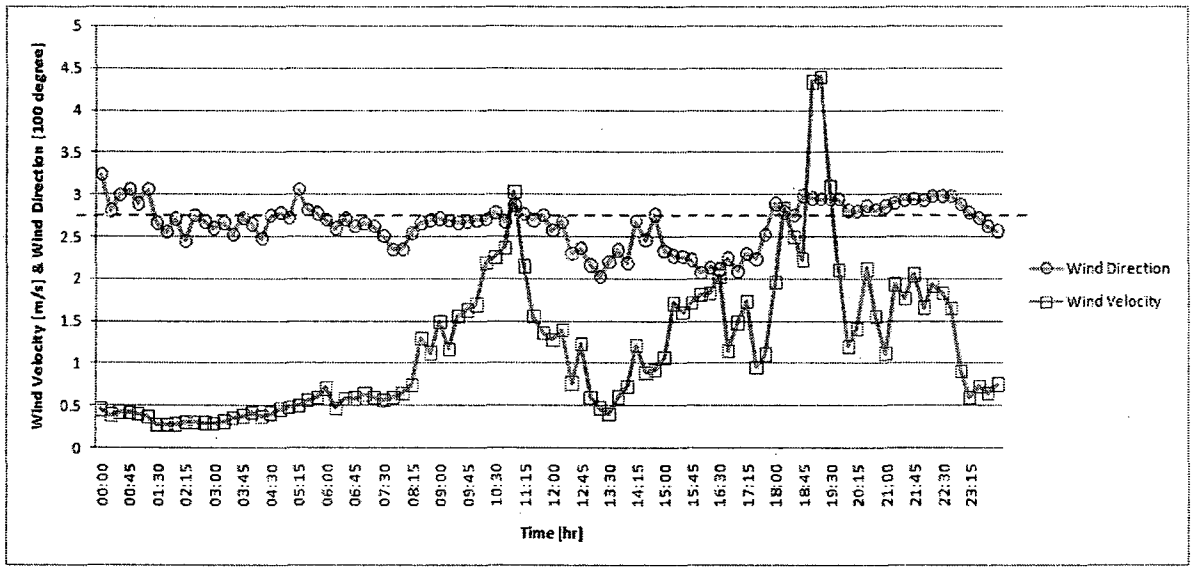

Figure 5.4: Wind direction and velocity measured at test-cell site and used as boundary condition for airflow modeling.

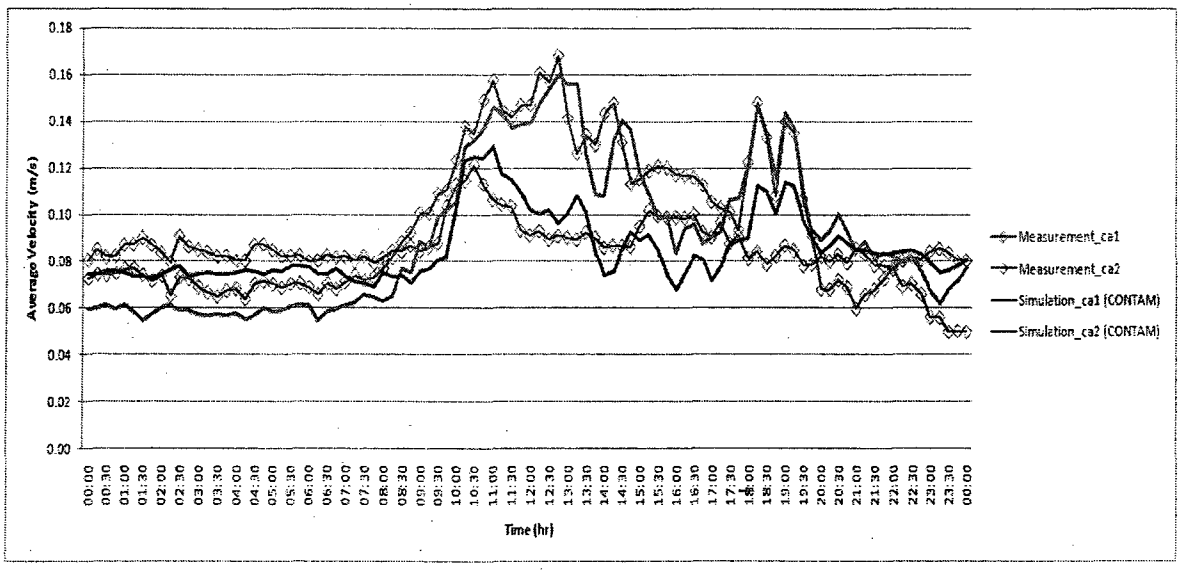

Figure 5.5-a: Comparison of measured data and simulation results.

To model, three airflow zones in front and three airflow zones behind the shading device were assumed (figure 5.6-a). This subdivision was implied to the ESP-r airflow network. It was assumed that each subdivided airflow zone has a temperature boundary condition which is equal to the value that the corresponding thermocouples shows at each time step. However, the modeling result (figure 5.5-b) shows that this assumption caused a significant error and a large discrepancy between the airflow modeling result and measurements.

To improve the prediction of base-case airflow modeling, another subdivision of the pressure zone was assumed. This time only one zone in front of the shading device was considered (figure 5.6-b) and the average value that three thermocouples in front of the

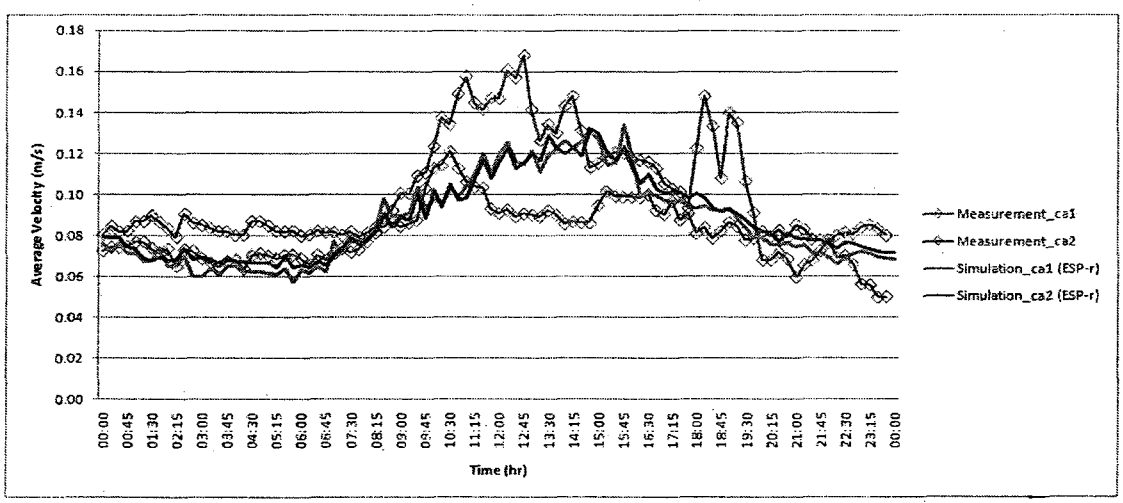

Figure 5.5-b: Airflow modeling with three subdivisions of pressure zones on either sides of the shading device.

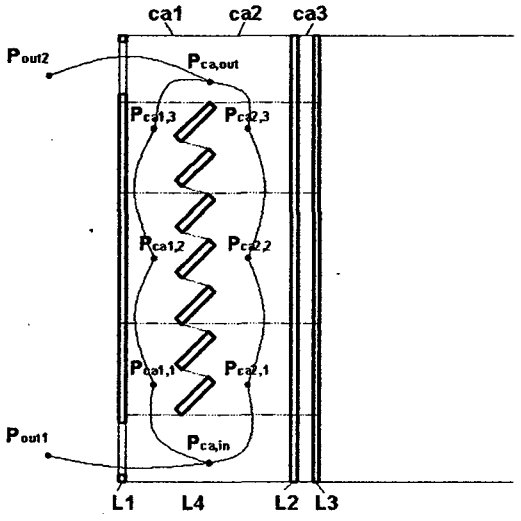

Figure 5.6-a: Subdivision of airflow zones implemented in ESP-r. It was assumed that the temperature of smaller pressure zones can be represented by thermocouples. Simulation of the base-case model showed considerable error caused by this assumption. The figure is not to scale.

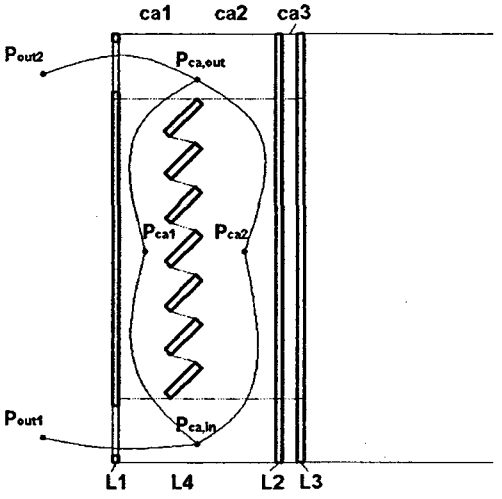

Figure 5.6-b: Subdivision of airflow zones implemented in CONTAM. The average temperatures of three thermocouples on either side of the blind were considered for P_{ca1} and P_{ca2}. This way, the simulation showed that the air velocity of zone P_{ca1} and P_{ca2} are in better agreement with the average values shown by anemometers at each side of blind. The figure is not to scale.

shading device were showing was picked up as the temperature of this single zone. In the same way, one pressure zone was assumed behind the shading device. Figure 5.5-a shows the simulation result with the latter division, and as mentioned before, there is a good agreement with measurement data.

Figures 5.7-a shows the average velocity simulated for single pressure zones with different values of the pressure coefficient (Cp=0.1, 0.3 and 0.5) and compares with values measured in front and behind the shading device. The deviation of simulated

velocity with a different Cp from the measured velocity is also presented in table 5.2. Cp=0.1 was found to have less deviation and closer simulation results to measurement. Comparing figures 5.7-a and 5.7-b it is obvious that the Cp variation can affect the velocity of ca1 (with a lower cross-section area) more than ca2.

Also, the other reason for lower wind effect compared to stack effect in this study is that the simulation periods chosen both for winter and summer are only for west wind with small pressure coefficient value (Cp=0.1) that decreases the effect of wind.

5.4 Base-Case Thermal Modeling Results and Verification

In this section, the base-case model prediction is compared with measurements from the test-cell to determine the accuracy of modeling and to estimate temperature distributions. This comparison was for temperature distribution in outer, inner ventilated cavity (Ca1 & Ca2), surface temperatures of glazing (L1 & L3) and shading device (L2). This will be followed by a sensitivity analysis on the base-case model, giving a better overview on the magnitude of errors that may be caused by source of uncertainties.

Verifications with test-cell measurements were preformed in winter and summer for start-up and one simulation day. Extended simulation for other days could be favourable, however measurement data were scarce, especially during the periods when the wind was blowing solely from west (Cp calibration).

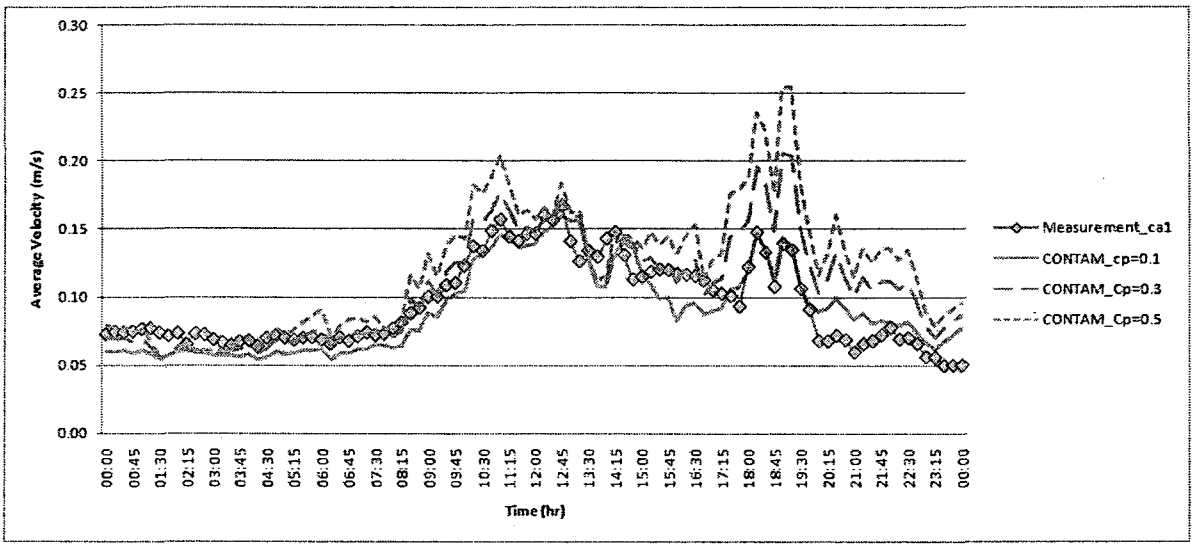

Figure 5.7-a: Comparison of simulated velocity with different Cp and measured value in front of shading device.

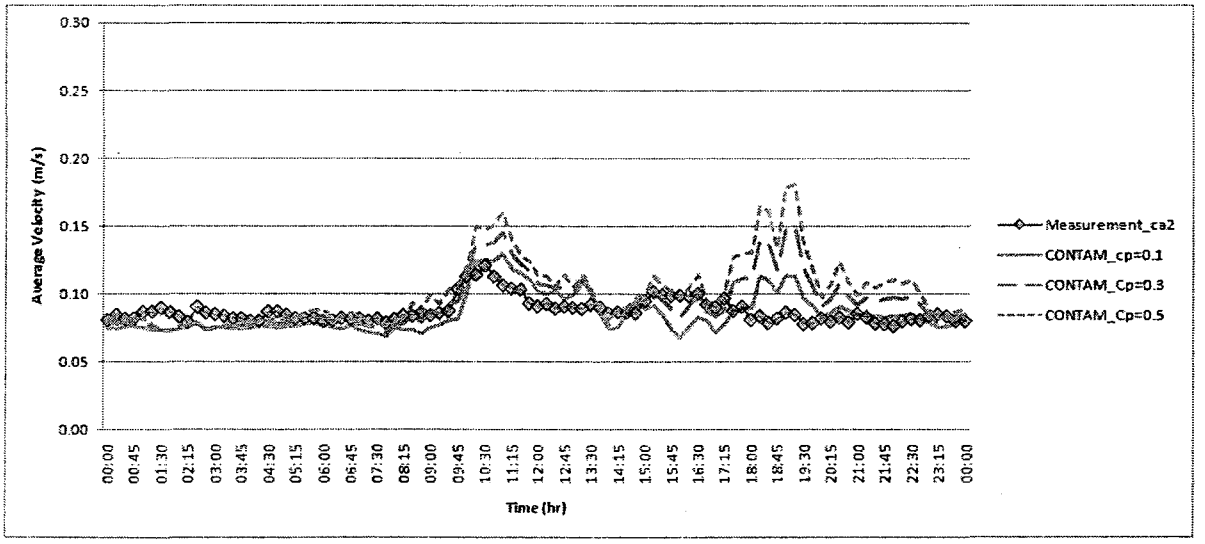

Figure 5.7-b: Comparison of simulated velocity with different Cp and measured value behind the shading device.

	Cp=0.1	Cp=0.3	Cp=0.3
Average deviation from measured velocity in Ca1	1.24	1.74	2.86
Average deviation from measured velocity in Ca2	1.00	1.22	1.65
Total average deviation	2.24	2.96	4.51

Table 5.2: Deviation of simulated velocity from measured velocity at each cavity with different Cp value. Ca1 is the air cavity next to the outdoor and Ca2 is next to the room.

Simulation Period	Total average airflow rate (kg/s)	Average airflow rate due to stack effect	Average $\Delta T_{outlet\ ,inlet}$ (K)	Average airflow rate due to wind effect (kg/s)	Average V_{wind} (m/s)
Summer	0.050	0.045	2.06	0.05	1.2
Winter	0.071	0.063	3.08	0.08	1.4

Table 5.3: Simulated average airflow rate in summer and winter due to wind and stack effect.

Figures 5.8 to 5.10 compare results of a simulated base-case model with measurements obtained from the test-cell during the summer period. Figure 5.8 illustrates horizontal temperature distribution through the DSF on a summer night and afternoon. At night, in the absence of solar radiation, there is a good agreement between measured data and simulation results and the maximum deviation is |0.7| C. However, the discrepancy increases in daytime to a maximum deviation of |2.6|C. This discrepancy is due to errors both in measurement and simulation.

The main sources of simulation errors are due to uncertainties of solar distribution on DSF surfaces, and angular solar properties of DSF components, especially venetian blind. Moreover, no surface temperature measurement was available for the room attached to DSF. Therefore, there are uncertainties about the real amount of long-wave radiation transfer between the room side of L3 and room surfaces. This uncertainty increases over daytime when the temperature of L3 increases due to absorbed solar radiation. This caused the highest temperature deviation in figure 5.8. The value of the convection coefficient is also among sources of errors; however, it is not as severe as the former sources (due to sensitivity analysis). This is more evident at nighttime when there is no solar radiation and the temperature difference between the room side of L3 and room surfaces is not high (figure 5.9); there is still small deviation.

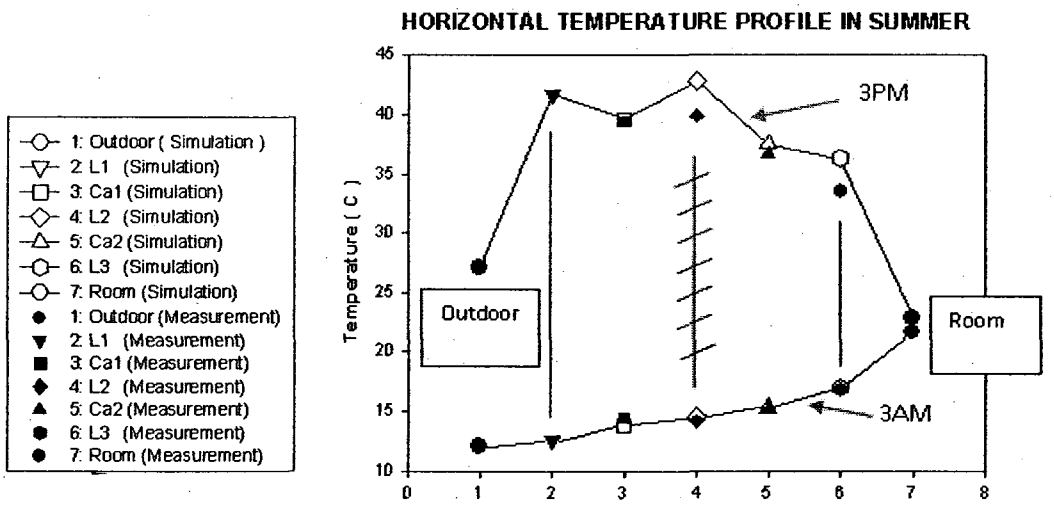

Figure 5.8: Horizontal temperature profile at the height of 1.75 of DSF on a summer day and night; comparison of simulation results with measurement data. Note that Outdoor, room and L1 temperatures are BCs for modeled base-case. Thus they have the same value in measurement and simulation. The total solar incident on L1surface is $I=270W/m^2$ *at 3Pm.*

SUMMER- 3AM

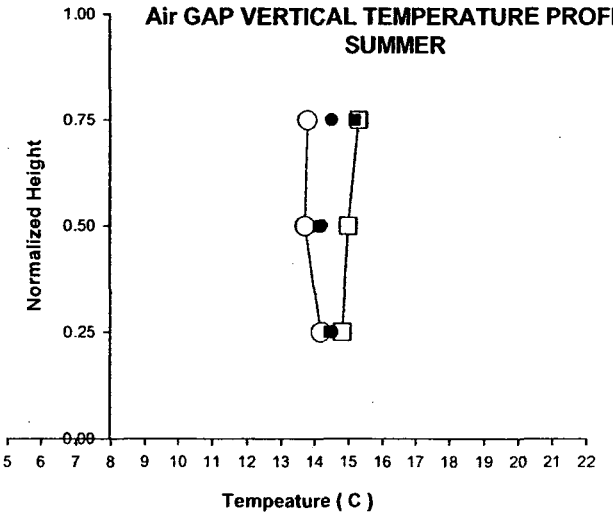

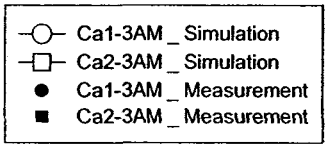

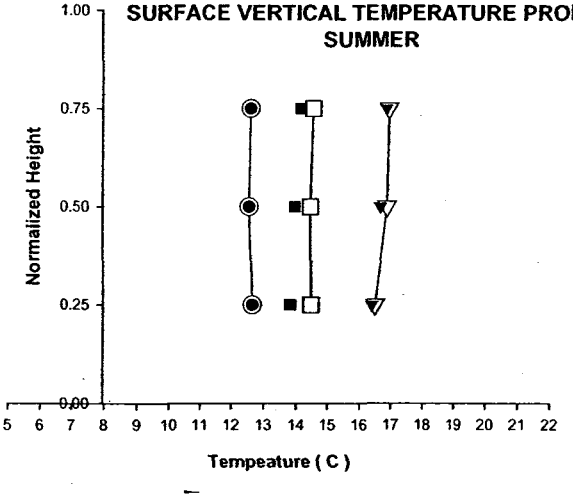

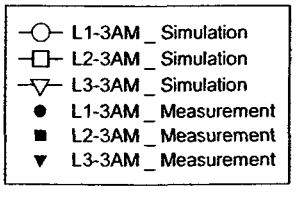

Figure 5.9: Comparison of vertical temperature profile of simulated base-case and measurement data on a summer night; upper diagram (a) shows surface temperature and lower diagram (b) shows air channel temperature comparison

SUMMER- 3PM

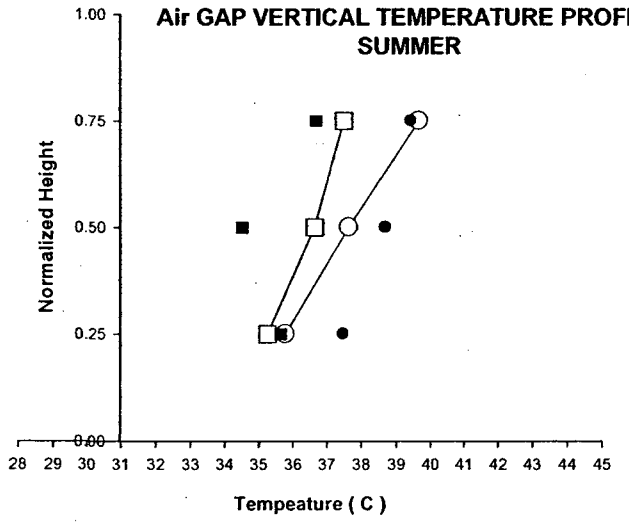

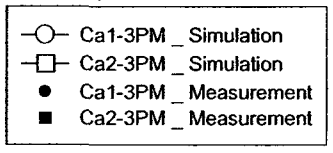

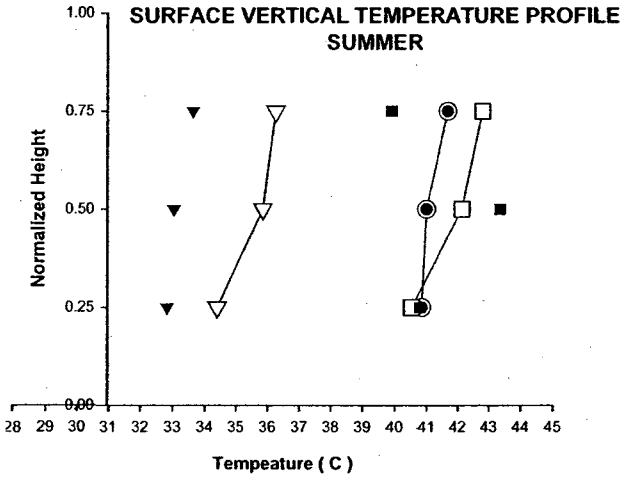

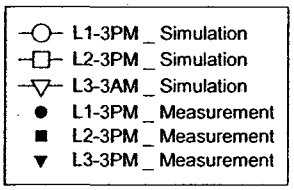

Figure 5.10: Comparison of vertical temperature profile of simulated base-case and measurement data on a summer day; upper diagram (a) shows surface temperature and lower diagram (b) shows air channel temperature comparison

Figures 5.9 to 5.10 show the vertical temperature profiles of the DSF. Generally, temperature increases in a vertical direction with increase of height. The reason is that the ventilated air which is coming from outside will have more time to be in contact with warmer surfaces. These warm surfaces include L3 surface at nighttime (next to room temperature, which is warmer than outside) and hot venetian blind and glazing, due to absorbed solar radiation. As mentioned, the agreement in daytime is less due to uncertainties of angular solar properties, distribution and increased temperature difference of L3 and room surfaces. The deviation increases at higher heights due to warmer ventilated air. The worst case scenario can be seen in figure 5.10-b with a deviation of ±2.8C wherein all these uncertainties coincide.

Figures 5.11 to 5.13 show the comparison between simulation and measurement for a winter night and day. Figure 5.11, which shows a horizontal temperature distribution of DSF layers, indicates an approximately linear temperature gradient at nighttime between outside and room air. The closer layers are to room air, the warmer they are. The slope of the temperature gradient at night in winter is greater than in figure 5.9 due to the higher temperature difference between outdoor and room air. Although simulation results fit well with measurements at summer night, the agreement is less during the winter night because of the aforementioned temperature difference. This can be seen as discrepancy of L3 surface temperature in figures 5.11 and 5.12-b.

In contrast, the winter day shows a better agreement than the summer day since in winter daytime, the hot L3 layer has a closer temperature to room temperature due to absorbed solar radiation. This is not always the case on winter days and based on sky conditions,

the absorbed solar radiation may even exceed that of summer day, and deviation increases.

Figures 5.12 to 5.13 show vertical temperature profiles of DSF. Like the summer counterparts, temperature increase at higher elevations is generally observed. The agreement at nighttime is less than summer nighttime due to increased temperature difference between outdoor and room air (Figures 5.12-a and 5.12-b). Lower incident solar radiation led to better agreement during winter daytime modeling. The maximum deviation between measurements and simulation results during winter nighttime and daytime are |1.3|C and |1.9|C, respectively.

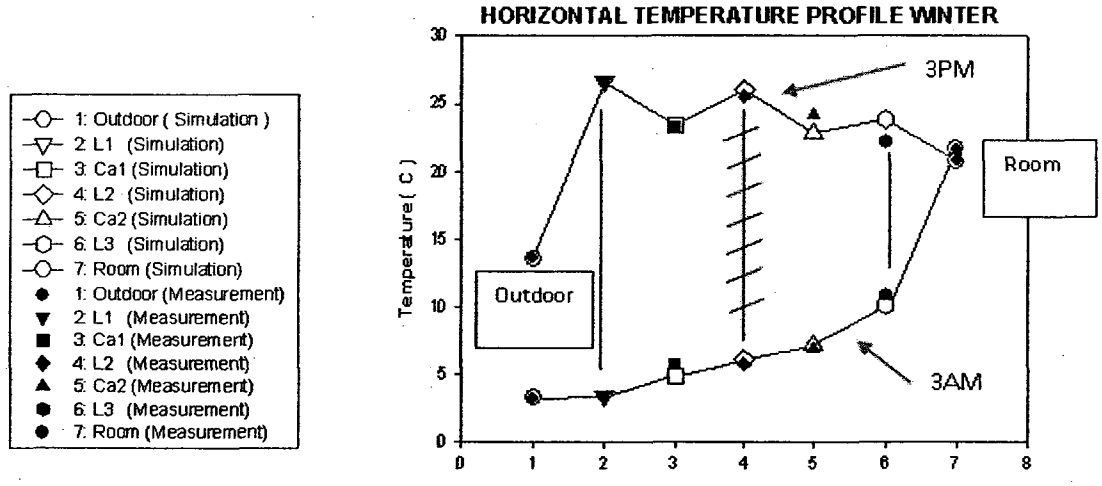

Figure 5.11: Horizontal temperature profile at the height of 1.75 of DSF in a winter day and night; comparison of simulation results with measurement data. Note that Outdoor, room and L1 temperatures are BCs for modeled base-case; thus they have the same value in measurement and simulation. The total solar incident on L1surface is I=190W/m^{2}at 3Pm.

WINTER- 3AM

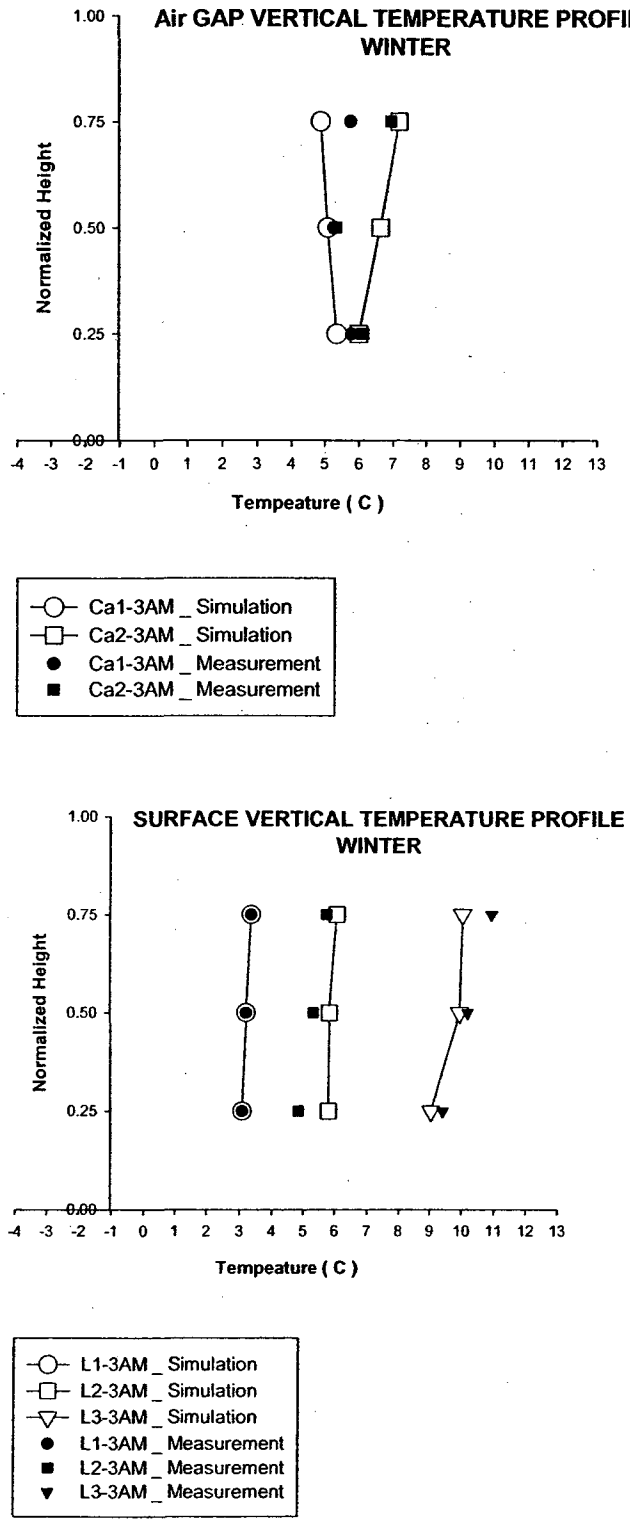

Figure 5.12: comparison of vertical temperature profile of simulated base-case and measurement data in a winter night; upper diagram (a) shows surface temperature and lower diagram (b) shows air channel temperature comparison

WINTER- 3PM

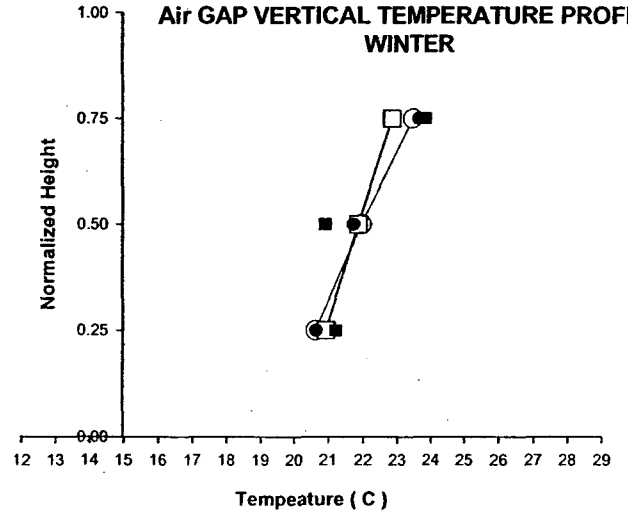

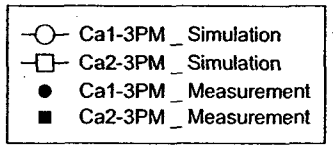

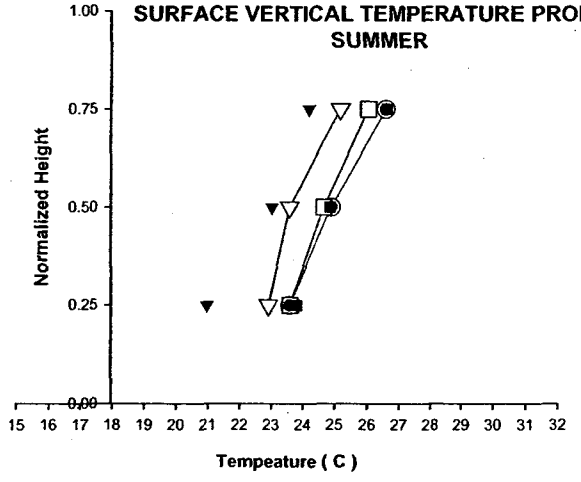

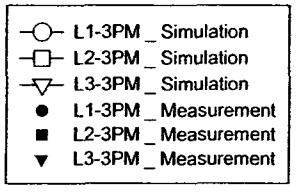

Figure 5.13: comparison of vertical temperature profile of simulated base-case and measurement data in a winter day; upper diagram (a) shows surface temperature and lower diagram (b) shows air channel temperature comparison

5.5 Conclusion

In addition to measurement errors there are several main sources of uncertainties in modeling, including:

- Solar distribution on DSF components (approximation in calculating absorbed solar radiation using shape factors);
- Angular properties of DSF components (the values used for solar properties of test-cell components were approximate);
- Convection coefficient values due to uncertainties of applied correlation and real amount of ventilated air velocity inside the air channel (no particular correlation specified in literature and unidirectional flow assumption);
- Amount of long-wave heat transfer rate between the room side of the L1 surface and room surfaces (lack of room surface temperature measurement);

In spite of these uncertainties, verification of base-case model results revealed that generally there is a good agreement between measurements and simulation results in winter and summer. At nighttime, in absence of solar radiation, the convection heat transfer coefficient and long-wave heat transfer may cause errors which are less than those during daytime (figure 5.12). Between winter nighttime and summer nighttime, winter shows more deviation due to a steeper temperature gradient with outdoor air. Summer daytime was the worst case scenario for prediction due to the accumulation of all uncertainties. However, the maximum deviation was |2.6|C.

Next section performs sensitivity analysis of base-case model considering the main sources of uncertainties whose domain of inaccuracy are given or obtainable from literature. This analysis also includes modeling assumption that may cause errors in prediction of modeling results.

5.6 Sensitivity analysis

In this section, sensitivity analysis investigates how (compared to measurement) errors in the output of base-case model can be apportioned quantitatively to different sources of uncertainties in the input of the model. In other words, sensitivity analysis is to identify what source of uncertainty weighs more on the study's conclusions. It is done by looking at the effect of varying the inputs of a base-case model on the output of the model.

A method by Saelens (2002) was adopted to perform this analysis. This method uses dimensionless temperatures to describe the main energy features of DSF. These dimensionless temperatures include:

$$\Delta T_{Ca1} = \frac{T_{Ca1} - T_{Outdoor}}{T_{Room} - T_{Outdoor}}$$

$$\Delta T_{Ca2} = \frac{T_{Room} - T_{Ca2}}{T_{Room} - T_{Outdoor}}$$

$$\Delta T_{Outlet} = \frac{T_{Outlet} - T_{Inlet}}{T_{Room} - T_{Outdoor}}$$

ΔT_{ca1} and ΔT_{ca2} are measures for the heat flux through the exterior and interior pane, respectively and ΔT_{outlet} is a measure for the enthalpy change of the air flowing through the cavity. Saelens D. (2002) explains that attention should be paid not to compare these

dimensionless numbers with those of other systems because the dimensionless numbers depend on the properties of the panes, the airflow rate, the height of the system, etc.

In this study, sensitivity analysis of the base-case model was performed in two main parts. First, the sensitivity of the base-case model to sensor inaccuracy was studied, and then the sensitivity to numerical modeling assumption and parameters was studied. The numerical modeling sensitivity analysis itself was subdivided to thermal and airflow modeling sensitivity.

The values presented in tables 5.4 to 5.6 are the relative percent errors with respect to calibrated base-case airflow modeling and verified base-case thermal modeling. Table 5.4 shows how the variation of some input parameters due to sensor inaccuracy changes the simulation results, which have been represented here by dimensionless temperatures.

Four types of sensors at the test-cell facility, which measured the input data to base-case model, were analyzed. These sensors measured air temperature, glazing surface temperature, solar radiation intensity and wind velocity. The accuracy of the sensors was not given and they were either derived from the manufacturer's brochure or assumed based on extreme cases in literature.

The inlet air temperature inaccuracy is equal to maximum error caused by the specified thermocouples, which is ±0.5K. After variation of the inlet temperature in the base-case

model, ΔT_{outlet} , which represents enthalpy changes in vertical air channel, showed the highest sensitivity to errors, especially in winter when the temperature gradient increases between DSF and outdoor air.

Input Parameters				ΔT_{ca1} (%)	ΔT_{ca2} (%)	ΔT_{outlet} (%)
Sensors' Inaccuracy	Inlet Temperature	+0.5K	Winter	6.64	-6.90	-11.12
			Summer	-0.86	-0.39	4.37
		-0.5K	Winter	-7.57	5.96	9.45
			Summer	0.87	0.44	-5.08
	Outer Glazing Surface Temperature	+0.5K	Winter	1.74	-0.51	6.87
			Summer	-1.78	-0.25	-3.24
		-0.5K	Winter	-1.90	0.50	-8.25
			Summer	2.00	0.26	3.64
	Solar Radiation	+%3	Winter	0.37	-0.33	1.50
			Summer	0.56	0.27	2.32
		-%3	Winter	-0.38	0.33	-1.59
			Summer	-0.48	-0.07	-1.66

Table 5.4: Sensitivity of base-case model to sensor inaccuracy

The outer glazing surface temperature was measured by thermometers (PT-00) covered with aluminum foil to reduce the effects of radiation. Assuming the error of ±0.5K to

account for sensor inaccuracy, again ΔT_{outlet} in winter demonstrated the highest inaccuracy, but lower than the thermocouple's case.

The measurement error of solar radiation with a pyranometer was approximated to be ±%3. The sensitivity is less than two former cases, however summer shows more uncertainties. Comparing the sensitivities in table 5.4, it can be concluded that the enthalpy change (ΔToutlet), is the most sensitive variable and inaccuracy of inlet thermocouples are the main source of base-case modeling error, especially in winter with a steeper temperature gradient from outdoor to indoor air.

The second part of sensitivity analysis investigates the sources of errors that may arise from numerical modeling assumptions. Tables 5.5 & 5.6 show these uncertainties for airflow and thermal modeling, respectively. These groups led to much higher errors compared with sensor errors.

As stated before, the proposed methodology is able to predict only the bulk flow rate of the air channel; and its detailed patterns are not seen. This airflow modeling method needs the air temperature of simulated zones as a boundary condition. This temperature needs to be the average temperature of the zone, which is measured by thermocouples. Therefore, the number and location of thermocouples with respect to chosen airflow zones play an important role in modeling accuracy. In the test-cell of naturally-ventilated DSF, there were three thermocouples on either side of the blind to measure air temperature. Thus, in modeling there were several alternatives to choose airflow zones:

- Subdividing the air channel on either side of the blind to 3 zones and assuming the measured value of thermocouples as an average temperature of each airflow zone;
- Subdividing the air channel on either side of the blind to 2 zones and assuming the average measured value of each two thermocouples as an average temperature of each airflow zone;
- Subdividing the air channel on either side of the blind to 1 zone and assuming the average measured value of all three thermocouples as an average temperature at each airflow zone.

The last assumption was applied to base-case airflow modeling and the relative percent error reported in table 5.5 is compared to this one zone assumption.

Table 5.5 shows high errors might be caused by choosing three thermal zones. This is because in a three airflow zone subdivision, thermocouples are not representing the average temperature of small zones. The other part of table reports the errors that may occur due to orifice equation parameters. The most significant errors in airflow modeling can cause due to uncertainties of discharge coefficient in the orifice flow equation. As explained in chapter 3, the orifice equation is to find the mass flow rate between two pressure nodes:

$$m_{i,j} = C_d A \sqrt{\frac{2\,(\Delta P_{i,j})}{\rho}}$$

where

i,j = two linked pressure nodes;

C_d = discharge coefficient commonly taken as 0.65;

A = orifice opening area.

Input Parameters					ΔT_{cal} (%)	ΔT_{ca2} (%)	ΔT_{outlet} (%)
Airflow Modeling	Number of Zones	2 zones	Winter		1.91	-2.30	7.74
			Summer		5.31	-0.69	12.80
		3 zones	Winter		2.55	-3.88	10.20
			Summer		7.00	-0.51	17.01
	Orifice Flow Parameters	Dampers	C_d=0.1	Winter	14.90	-46.75	55.12
				Summer	-39.80	-18.14	-44.09
			C_d=0.9	Winter	96.39	100.66	100.26
				Summer	12.69	2.92	27.44
		Air Channel	C_d=0.1	Winter	12.94	-45.51	40.99
				Summer	25.80	8.43	50.38
			C_d=0.9	Winter	0.91	-12.95	8.49
				Summer	2.71	1.08	10.49

Table 5.5: Sensitivity of base-case model to airflow modeling parameters

The discharge coefficient, C_d, is related to the dynamic effects and is typically close to 0.5 for a sharp-edged orifice. In base-case modeling C_d=0.5 was assumed both for the air channel and dampers' openings; the model was then calibrated. The reported values in table 5.5 are deviations of dimensionless temperatures with respect to the calibrated base-case model. Two extreme values of C_d=0.1 and C_d=0.9 were considered. These studied values are 0.4 higher (C_d=0.9) and 0.4 lower (C_d=0.1) than calibrated C_d value (C_d=0.5). Dimensionless temperature ΔT_{outlet} shows a very high error may occur by approximating C_d. The base-case model is more sensitive to C_d approximation through the dampers' openings than through the air channel. However, dampers show more sensitivity in summer while the air channel is more sensitive to C_d uncertainties in winter.

The second part of modeling assumption sensitivity, which analyzes the effect of uncertainties of thermal modeling on the results of base-case model, has been presented in table 5.6. The sources of uncertainties have been divided to three main parts: number of subdivided thermal zones; solar radiation distribution and convection coefficient correlation.

In contrast to airflow zones, the smaller the subdivided thermal zones of the air channel are, the more they can capture the thermal stratification of the air channel. The base-case was modeled with four subdivided thermal zones and table 5.6 shows the deviation of one thermal zone subdivision from the base-case model. The error caused by reducing the thermal zone is significant in the case of ΔT_{outlet} for the summer case. However, ΔT_{Ca2} is slightly sensitive to the number of thermal zones. This indicates that the numbers of

zones are not affecting the amount of predicted heating/cooling load of attached room to the DSF if the ventilation the air from air channel is not exhausted to the room.

As explained earlier, one problem common to building energy simulation software is that the direct solar radiation beam, after passing through the second internal window, is treated as diffused radiation. This way it is distributed according to absorptance-weighted area ratios instead of tracking the entered solar radiation beam. In the base-case model, the software code was changed in order to track the entered solar radiation beam. Table 5.6 compares the base-case model with the default absorptance-weighted area ratio method, showing slight changes of the dimensionless number. In other words, the absorptance-weighted area ratio method does not affect the accuracy of modeling notably. The reason is that during the simulation period the blind was half closed (tilt angle was 45) and the amount of direct beam passing through the venetian blind to enter the second internal zone was not significant.

In chapter 3, a series of convection coefficient correlations were proposed in order to handle all possible convective heat transfer regimes that may occur in DSF air channel. Thus, the code of the building energy simulation software was modified in order to use the proposed correlations. The default correlations in the two applied building energy simulation software programs are general correlations for buoyancy driven flow in vertical channels:

In TRNSYS:

$$Hc = 1.5(T_{surfvertival} - T_{airvertical})^{0.25}$$

(TRNSYS, 2004)

(5.1)

Where,

$T_{surfvertical}$ includes the surface temperature of both glazing and blind and $T_{airvertical}$ is the air channel temperature.

In ESP-r:

$$Ra_D = \frac{g D_{channel} \beta \Delta T}{\nu \alpha} \tag{5.2}$$

$$Nu = \frac{1}{\sqrt{\frac{576}{(Ra_D \frac{D_{channel}}{H_{channel}})^2} + \frac{2.87}{(Ra_D \frac{D_{channel}}{H_{channel}})^2}}}$$

(Bar-Cohen and Rohsenow, 1984)

(5.3)

$$Hc = \frac{Nu K_{air}}{D_{Channel}} \tag{5.4}$$

Where,

$D_{channel}$ is the characteristic length, which is equal to diameter of cavity;

$H_{channel}$ is the height of the cavity, m;

β is the thermal expansion coefficient, 1/K;

ΔT is the temperature difference between the cavity air and glazing or cavity air and blind, K;

ν is the kinematic viscosity, m^2 /s;

α is the thermal diffusivity, m^2/s.

Hc is the average heat transfer coefficient, W / m^2 K ;

K_{air} is the thermal conductivity of air, W/m.K;

And the second correlation from ESP-r is Alamdari and Hammond (1983):

$$Hc = \left[\left(1.5 \left(\frac{\Delta T}{H_{channel}} \right)^{0.25} \right)^6 + \left(1.23 (\Delta T)^{1/3} \right)^6 \right]^{1/6} \tag{5.5}$$

Where,

ΔT is the temperature difference between the cavity air and glazing or cavity air and blind, K;

$H_{channel}$ is the height of the cavity, m;

Hc is the average heat transfer coefficient, W / m^2 K ;

Table 5.6 compares general convection coefficient correlations of TRNSYS and ESP-r with the proposed correlations of chapter 3 used in the base-case model. Although general coefficient correlations of ESP-r and TRNSYS do not consider forced convection, in a naturally-ventilated DSF and in the absence of forced convection, the results are very close to the base-case model (table 5.6). The amount of error even is less than the inaccuracy that can be caused by thermocouple and thermometer error. However, as seen in the previous chapter, this is not the case for mechanically ventilated DSF sensitivity.

Input Parameters					ΔTca1 (%)	ΔTca2 (%)	ΔToutlet (%)
Thermal Modeling	Number of Zones	1 Thermal Zone	Winter		-4.06	-0.72	-113.21
			Summer		-16.96	0.65	-303.64
	Solar Radiation Distribution	Diffused	Winter		0.23	-0.19	0.94
			Summer		0.35	-0.80	2.05
	Convection Coefficient Correlation	TRNSYS	Winter		0.63	3.99	5.02
			Summer		2.31	-3.29	8.44
		ESP-r	Bar-Cohen& Rohsenow	Winter	1.42	4.01	7.12
				Summer	0.36	-3.71	-0.43
			Bar-Cohen& Rohsenow + Alamdari & Hammond*	Winter	1.50	3.89	7.38
				Summer	0.55	-3.73	0.00
			Alamdari & Hammond	Winter	1.52	3.85	7.53
				Summer	0.56	-3.71	0.08

Table 5.6: Sensitivity of base-case model to thermal modeling parameters

* Bar-Cohen& Rohsenow correlation was used for the blind surfaces and Alamdari & Hammond for glazing surfaces

In brief, in this section sensitivity analysis was performed by looking at the effect of varying the inputs of the base-case model on the output of the model. For this purpose three dimensionless parameters were defined to represent the output of the base-case model. These three outputs include ΔT_{Ca1}, ΔT_{Ca2} and ΔT_{outlet} , which indicate the energy flows through outer glazing, inner glazing and enthalpy of ventilation air, respectively. The variation of input parameters was considered based on two factors: inaccuracy of sensors and modeling method assumptions. Modeling method assumptions showed more significant errors than the inaccuracy of sensors. In most cases the error to predict ΔT_{outlet} was higher than other dimensionless temperatures. This stated that evaluation of energy performance of a DSF which exhausts the outlet air to indoor air or HVAC system should be done with care since the prediction of the air channel outlet is very sensitive to source of uncertainties, especially modeling method assumptions. ΔT_{Ca1} & ΔT_{Ca2} are generally less sensitive to sources of uncertainties, except in airflow modeling for the assumed discharge coefficient, Cd. This indicates that many modeling assumptions have minor effects on the heating/cooling load of the attached room to a DSF, as long as outlet air from air channel is not discharged to the room, e.g. as in an external air circulation DSF.

5.7 Conclusion

A naturally-ventilated base-case model of a DSF was developed using TRNSYS software. The base-case model is able to predict thermal distribution and airflow rate of the DSF under real operation conditions. The prediction of the airflow model was restricted to bulk flow motion since a detailed pattern of air movement was not the aim of this modeling. This bulk flow information was enough for the thermal model of the base-

case to predict temperature profiles. The base-case model simulation results were then compared with measurements from the test-cell to determine the accuracy of modeling. The comparison revealed that there is generally a good agreement between measurements and simulation results in winter and summer. Summer daytime was the worst case scenario for prediction due to the accumulation of all uncertainties. However, the maximum deviation was |2.6|C. Finally a sensitivity analysis was performed to figure out the severity of sources of uncertainties in base-case modeling. The considered sources of uncertainties were the inaccuracy of sensors and modeling method assumptions. Modeling method assumptions showed more significant errors than inaccuracy of sensors. In airflow modeling the pressure coefficient (Cd) and in thermal modeling the subdivision of thermal zones are the most important factors affecting the accuracy of the base-case model.

CHAPTER 6

ENERGY PERFORMANCE OF DSF WITH THERMAL MASS

In this section, the energy performance of a DSF façade combined with concrete thermal mass was studied and compared with a conventional type of DSF façade in order to find the energy saving that may be achieved with concrete thermal mass. Section 6.1 points out the performance criteria used in this study to compare the energy saving associated with DSF. Section 6.2 presents the simulation results and compares the energy performance of conventional and concrete thermal mass DSF in winter and summer time. Both mechanically and naturally ventilated DSFs with different air channel configurations were considered. Detailed energy flow paths of air channel configurations are shown in Appendix G. Section 6.3 gives the conclusion and section 6.4 proposes two building system implementations of the proposed thermal mass.

6.1 Performance Criteria

Energy performance of a façade is traditionally expressed with criteria such as U-value and Solar Heat Gain Coefficient (SHGC). However, these parameters are steady-state concepts and ignore the dynamic aspects of façade behaviour; therefore they cannot be directly applied to ventilated façades (as it has already been demonstrated in Saelens, 2002; Corgnati et al., 2003; Faggembauu et al. 2003,Perino et al, 2005). Most performance criteria introduced in the litrature on DSF are assessment parameters only

for DSF separeted from an attached room. In this chapter the heating/cooling load of an attached room to a DSF has been used as a measure to evaluate the energy performnace of the DSF. This way, not only all heat transmission through the façade and solar heat gains are considered, but also the amount of heat intoduced by ventilation air is taken into account.

6.2 Simulation

In this section the energy performance of a conventional DSF is compared with the performance of a DSF combined with concrete thermal mass both for mechanically- and naturally-ventilated cases. The base-case models of conventional DSF were developed and verified in previous chapters (one base-case model for mechanically-ventilated in chapter 4 and one for naturally ventilated DSF in chapter 5). In this section the verified base-case models are modified to develop four new base-case models (three new types of mechanically-ventilated DSF which are IAC, SA & EA, and one new type of naturally-ventilated DSF which is OAC) and then a parametric study was conducted by replacing DSF layers with concrete thermal-mass (figure 6.1).

The differences between the base-cases (which are studied in this chapter with those developed and verified in previous chapters) are airflow path direction, location of single/double glazing and air channel depth. In the parametric study, thermal mass is replaced with one of these three layers:

- Concrete thermal mass slab replacing the outer skin of DSF (TMo),
- Concrete thermal mass slats replacing the aluminum blind (TM),
- Concrete thermal mass slab replacing the inner skin of DSF (TMi)

MECHANICALLY VENTILATED DSF NATURALLY VENTILATED DSF

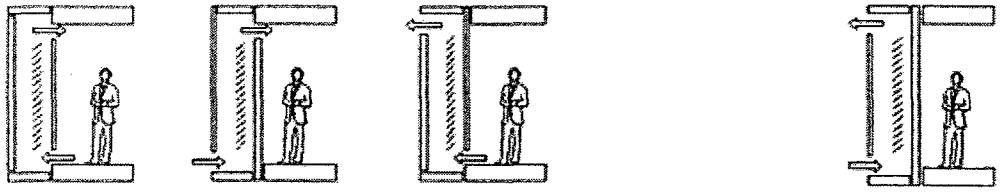

AL

IAC
Inner: single glazing
Outer: double glazing
Blind: aluminum

SA
Inner: double glazing
Outer: single glazing
Blind: aluminum

EA
Inner: single glazing
Outer: double glazing
Blind: aluminum

OAC
Inner: double glazing
Outer: single glazing
Blind: aluminum

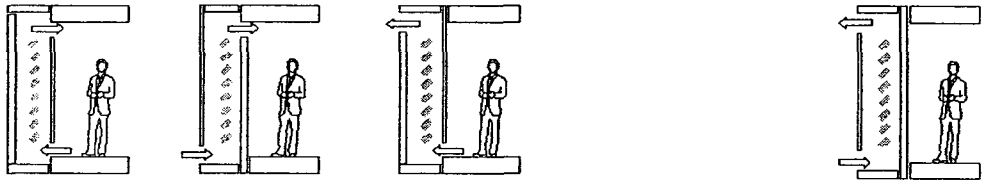

TM

IAC
Inner: single glazing
Outer: double glazing
Blind: concrete slat

SA
Inner: double glazing
Outer: single glazing
Blind: concrete slat

EA
Inner: single glazing
Outer: double glazing
Blind: concrete slat

OAC
Inner: double glazing
Outer: single glazing
Blind: concrete slat

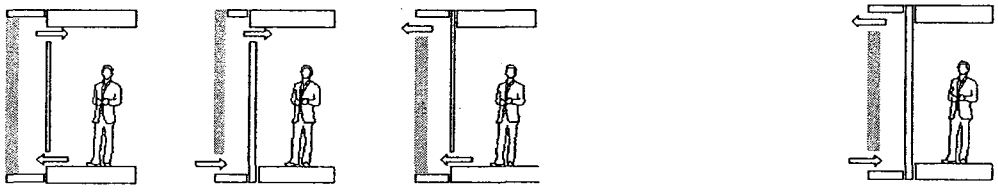

TMo

IAC
Inner: single glazing
Outer: concrete slab
Blind: none

SA
Inner: double glazing
Outer: concrete slab
Blind: none

EA
Inner: single glazing
Outer: concrete slab
Blind: none

OAC
Inner: double glazing
Outer: concrete slab
Blind: none

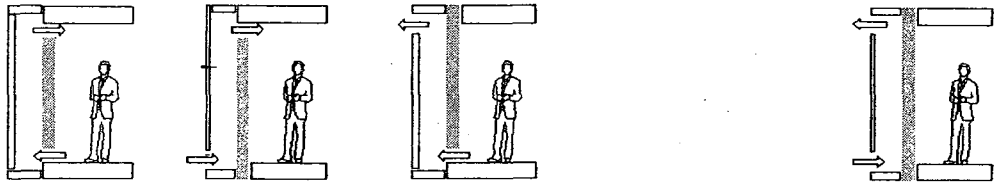

TMi

IAC
Inner: concrete slab
Outer: double glazing
Blind: none

SA
Inner: concrete slab
Outer: single glazing
Blind: none

EA
Inner: concrete slab
Outer: double glazing
Blind: none

OAC
Inner: double glazing
Outer: single glazing
Blind: none

Figure 6.1: *Simulated cases of conventional DSF and its counterparts with thermal mass combined.*

Four base-case models with the original aluminum shading device (AL) and their counter- parts with thermal mass have been illustrated in figure 6.1. More details about dimensions and surface area of AL, TM, TMi and TMo were tabulated in appendix F.

In practice, a DSF with thermal mass can cover the spandrel area of the façade (e.g. the portion of façade between two successive glazing systems). In this study just for the purpose of comparison, thermal mass covered the whole height of the façade including the glazing systems' area.

6.2.1 Mechanically-Ventilated DSF

The same geometry, material, climate, boundary conditions, ventilation rate and modeling assumption applied to the base-case model in chapter four were applied here to three new base-cases with aluminum slats. The only difference is the path of supply/exhaust and the location of double/single-glazed pane.

6.2.1.1 Sunny Day

Base-case models and DSFs with thermal-mass combined (TM, TMi, TMo) were simulated for a sunny day with three startup days during winter and summer period. The graphs show the heating/cooling load of an attached room to DSF in winter and summer. As discussed before, the heating/cooling load is referred in this chapter as performance criteria for alternative types of DSF.

Figures 6.2-a to 6.2-f show cooling/heating loads of the attached room to DSF for various types of AL, TM, TMi & TMo and different airflow path directions on a sunny winter and summer day. In summer, generally the DSF with AL blind has the highest cooling load and between alternatives with thermal mass, the lowest cooling load belongs to

TMo. TM and TMi have a close (almost identical) cooling load profile. During high solar radiation, TMi demands a higher cooling load than TM (by 12%), but in the afternoon TM requires a greater cooling load. The direction of the airflow path affects the magnitude of cooling loads. The highest cooling load is for IAC since the room air is heated up in the DSF and is returned back to the room. The case EA has the lowest cooling load since the outer side of inner layer has a temperature close to the room air and indirect solar gains are exhausted to outdoor.

In winter during solar noon, in almost all cases, the heating load is zero. At night and in early morning, the lowest heating load belongs to TM in all DSF types (IAC, SA & EA). This highlights TM as a superior layout for winter time. TMo, due to its direct exposure to cold ambient air, has the highest heating load at night and early morning (except in SA configuration). AL and TMi have close (almost identical) heating load profile. In the case of SA configuration, cold ambient air is supplied and flows on the DSF side of inner layer. This causes higher temperature gradient and heating loads as compared with the IAC and EA configurations. Moreover, in the case of SA, conventionally the inner layer is double-glazed with high thermal resistance. When this layer is replaced with a layer of thermal mass (TMi) with lower thermal resistance, the heating load increases considerably in comparison with TMi heating load profile in IAC and EA.

Figures 6.3-a to 6.3-c compare the loads associated with different types of DSF in winter and summer conditions. These figures compare the energy saving of DSF combined with thermal mass (TM, TMi & TMo) with the conventional DSF case (AL). Generally, in all

cases increasing the amount of thermal mass is beneficial and leads to load decrease in winter and summer. In winter, TM case leads to the highest energy saving in comparison with AL case, close to 60%, while other combinations (TMi & TMo) do not have any saving when compared with the AL case. During summertime, TMo causes substantial saving, close to 80%; TM and TMi have similar savings while TM still gives a better option than TMi. The figures also show the highest saving for TM configuration is associated with EA airflow path direction.

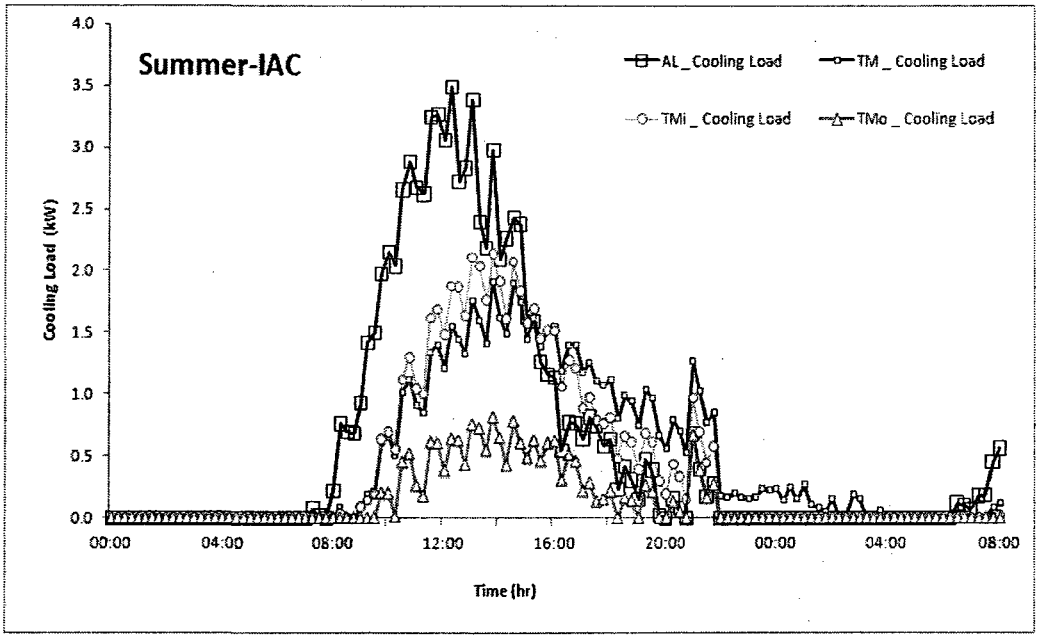

Figure 6.2-a: *Cooling load of the attached room to DSF for various types of AL, TM, TMi & TMo with IAC airflow path direction for a sunny summer day.*

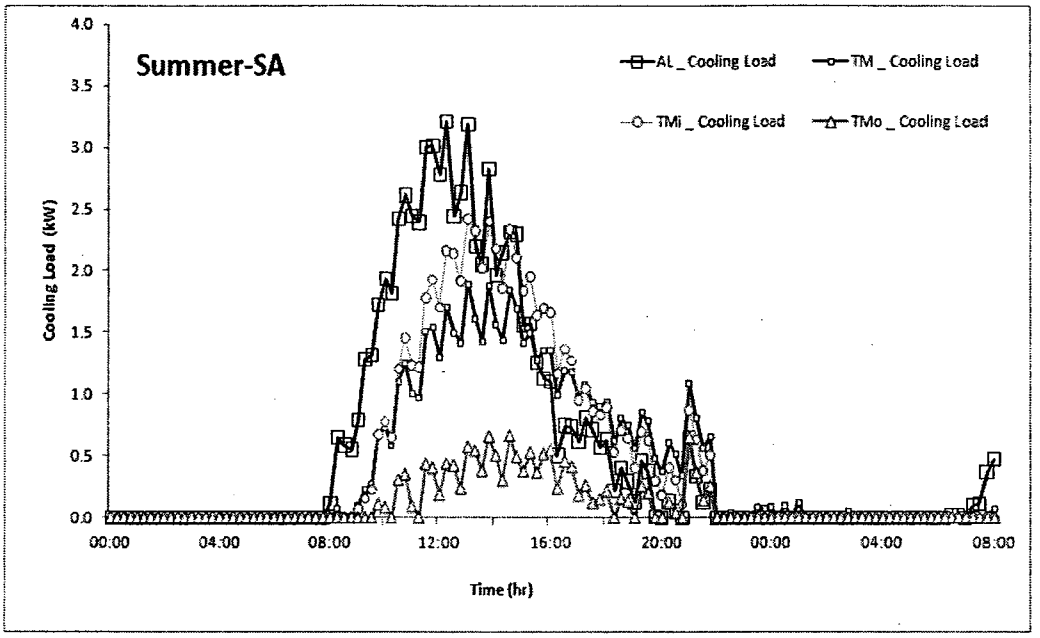

Figure 6.2-b: *Cooling load of the attached room to DSF for various types of AL, TM, TMi & TMo with SA airflow path direction for a sunny summer day.*

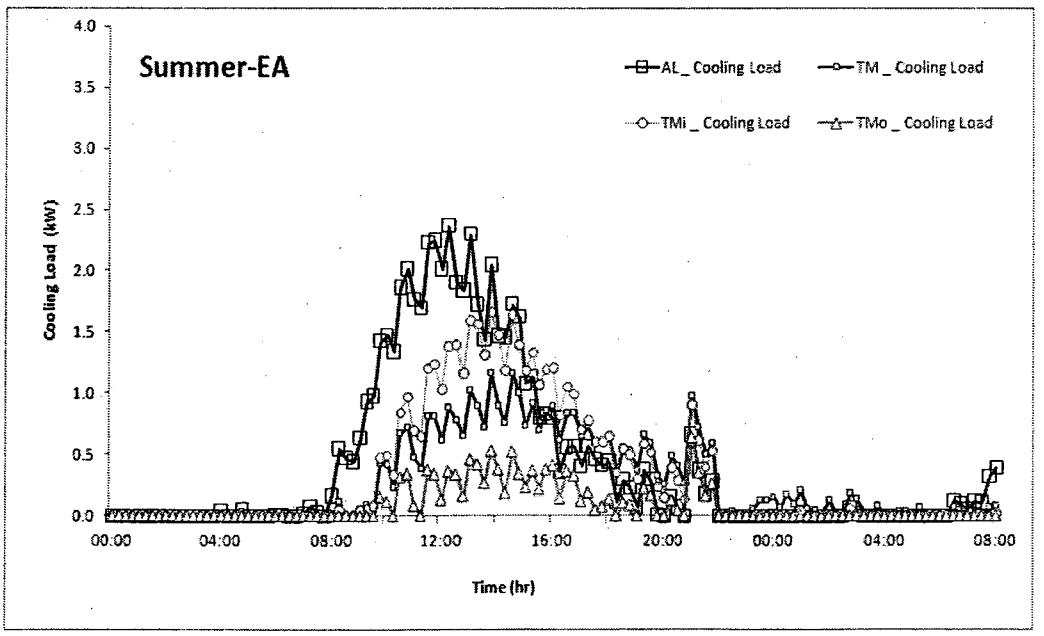

Figure 6.2-c: *Cooling load of attached room to DSF for various types of AL, TM, TMi & TMo with EA airflow path direction in a sunny summer day. In this case, the amount of air that exhausts is assumed to be infiltrated from surrounding warm*

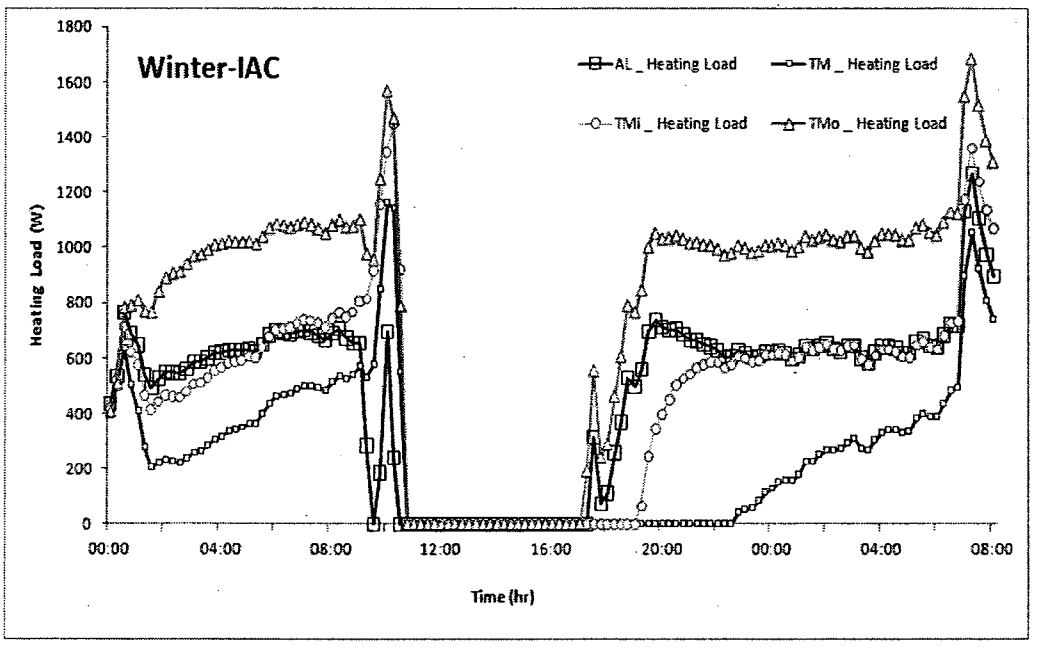

Figure 6.2-d: *Heating load of the attached room to DSF for various types of AL, TM, TMi & TMo with IAC airflow path direction for a sunny winter day.*

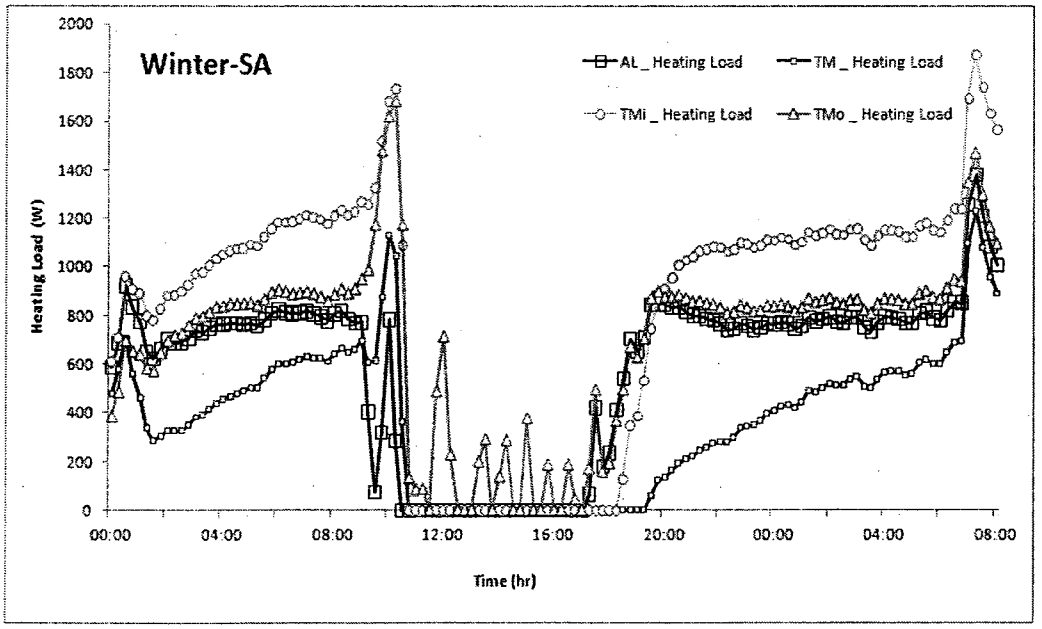

Figure 6.2-e: *Heating load of the attached room to DSF for various types of AL, TM, TMi & TMo with SA airflow path direction for a sunny winter day.*

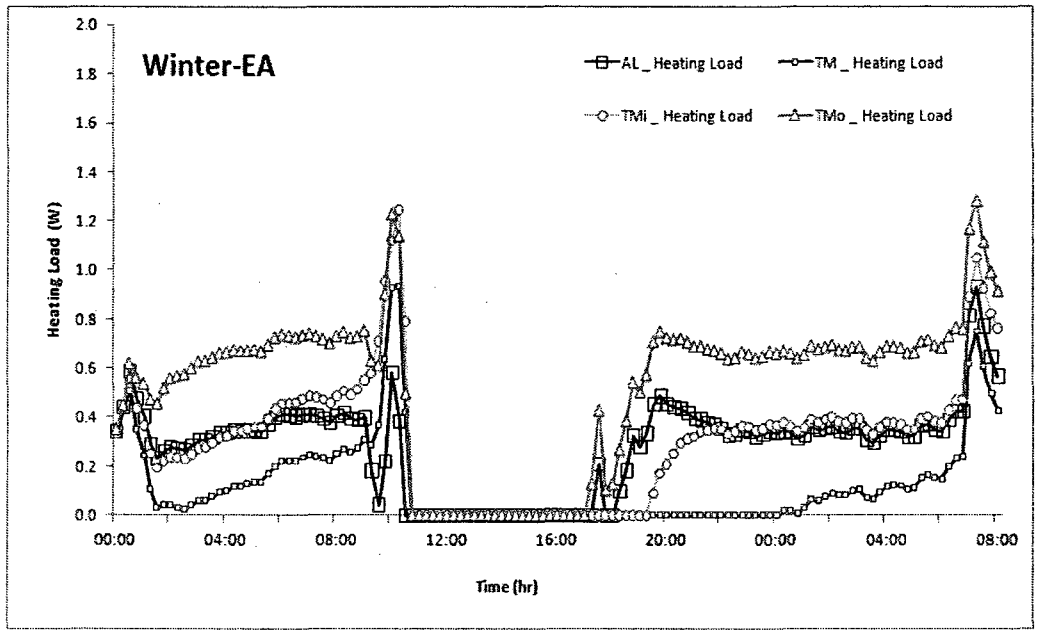

Figure 6.2-f: *Heating load of the attached room to DSF for various types of AL, TM, TMi & TMo with EA airflow path direction for a sunny winter day. In this case, the amount of air that exhausts is assumed to be infiltrated from surrounding warm*

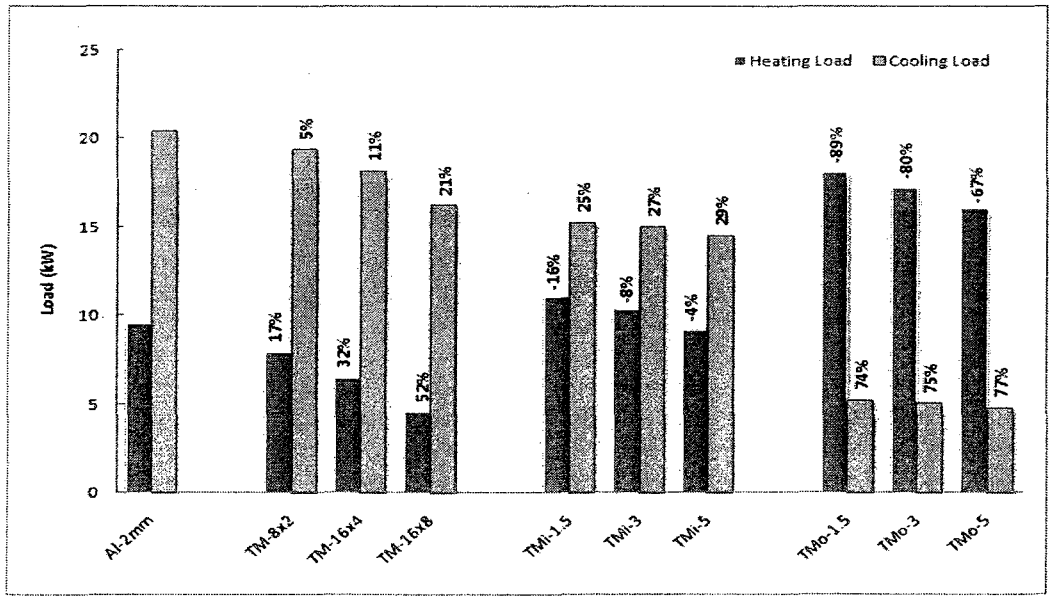

Figure 6.3-a*: Heating/Cooling loads associated with different types of DSF with IAC airflow path direction in winter and summer and the energy saved with TMi, TM & TMo was compared to AL in percentage.*

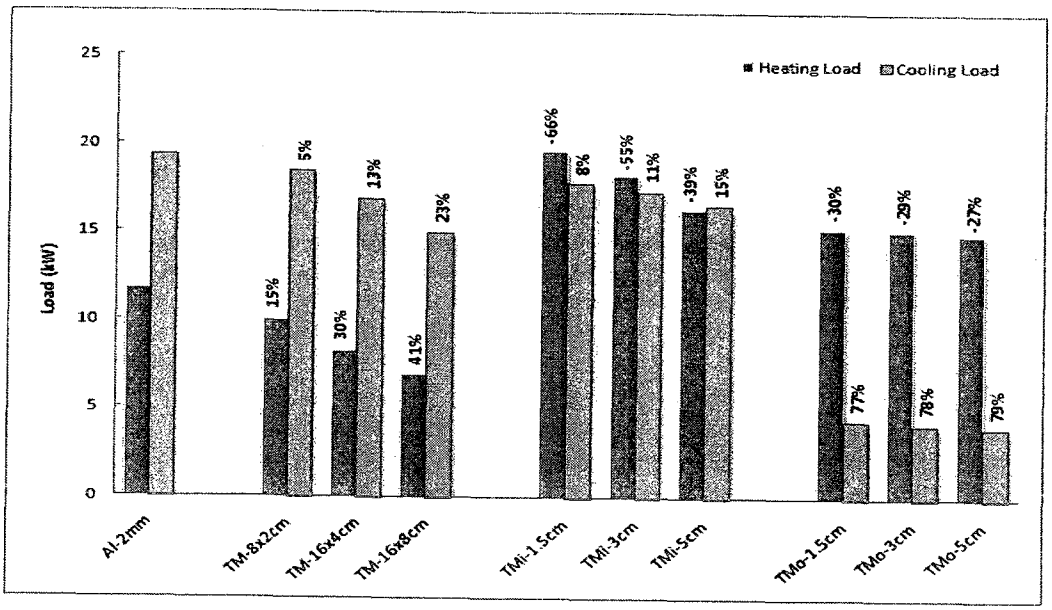

***Figure 6.3-b**: Heating/Cooling loads associated with different types of DSF with SA airflow path direction in winter and summer and the energy saved with TMi, TM & TMo was compared to AL in percentage.*

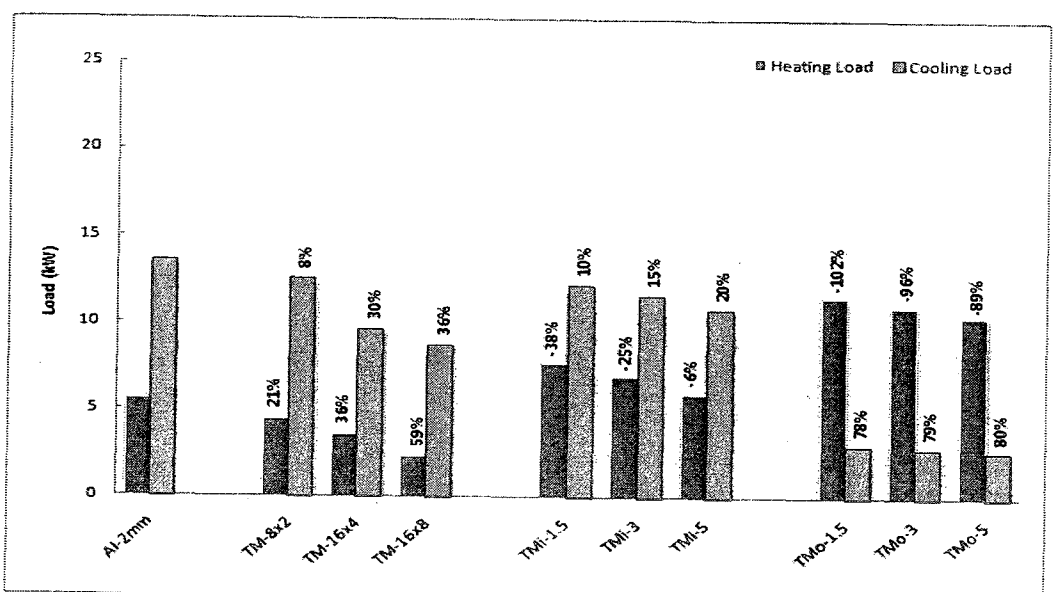

***Figure 6.3-c**: Heating/Cooling loads associated with different types of DSF with EA airflow path direction in winter and summer and the energy saved with TMi, TM & TMo was compared to AL in percentage.*

6.2.1.2 Cloudy Day

To investigate the energy saving of DSF combined with thermal mass on a cloudy day, a typical summer and winter day with an overcast sky were chosen and their thermal performances were modeled. Figure 6.4 illustrates the heating and cooling load of AL and TM. The first day is a sunny day followed by three cloudy days.

On the first winter day, during high solar radiation the heating load is zero both for AL and TM. The energy demanded for the heating load is in the afternoon and early morning. TM decreases heating loads from afternoon until the early morning of next day with a downward trend. As stated before, this way TM with an IAC configuration is capable of saving 52% in cooling load. On cloudy days during solar noon the heating load is still zero for AL but the load for TM is non-zero since it is storing solar energy. The saving for TM occurs from the afternoon and starting releasing it the early morning of next day. The system however has less energy to release due to less absorption (cloudy day). The saving for TM with an IAC configuration on a cloudy day is around 7%.

For the summer scenario, the first day is sunny thus the cooling load increases in the morning after sunrise until it reaches its peak load during high solar radiation for AL. It then starts decreasing in the afternoon and early morning of the next day. TM decreases and delays this peak load to several hours due to its capacity to store energy. On cloudy days, TM stores less solar energy during high solar radiation and releases all the stored energy by the early morning of the next day. The total energy saving on a cloudy day for

TM with IAC configuration is 5% while with the same configuration for a sunny day the saving was 21%.

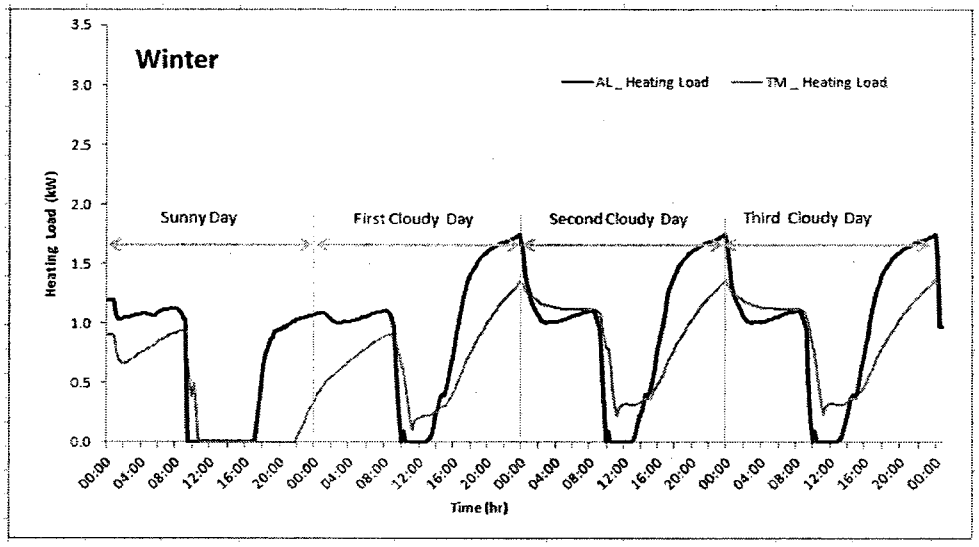

A) Heating load in winter

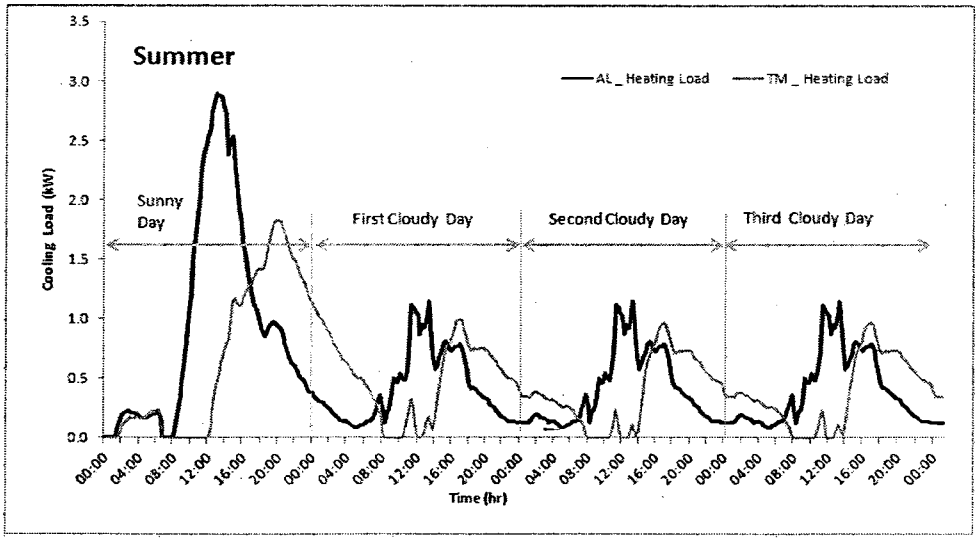

B) Cooling load in summer

Figure 6.4: *Cooling/Heating load of attached room to DSF for AL & TM with IAC airflow path direction. The First day is sunny and follows with three cloudy days. Due to lack of data the cloudy day weather data is repeating.*

Therefore, TM is a more energy efficient layout on summer and winter days with high solar radiation than on cloudy days.

6.2.2 Naturally-Ventilated DSF

Again, the same geometry, material, climate, boundary conditions and modeling assumption applied to the base-case model of chapter 5 were applied here to the new base-case with aluminum slats (AL). Then a parametric study was conducted by replacing DSF layers with concrete thermal-mass (TMi, TM, TMo). Figure 6.1 illustrates these cases for naturally ventilated DSF.

The following graphs show, TM and TMo have similar cooling load profiles and they both require less cooling load than the AL case. The figures also show that TMo is performed better that TM in summer by requiring shorter and less cooling load during daytime.

In contrast to a mechanically-ventilated DSF, TMi set-up needs a much higher cooling load in comparison with AL. This is due to replacement of the inner double glazing layer with low resistance thermal mass. Moreover, the lower airflow rate in summer in a naturally ventilated DSF leads to a higher air channel temperature and a higher cooling load as compared with the mechanical case.

In winter, surprisingly, AL has the lowest heating load of all DSFs with thermal mass combined (TM, TMo and TMi). This is due to its low airflow rate in air channel.

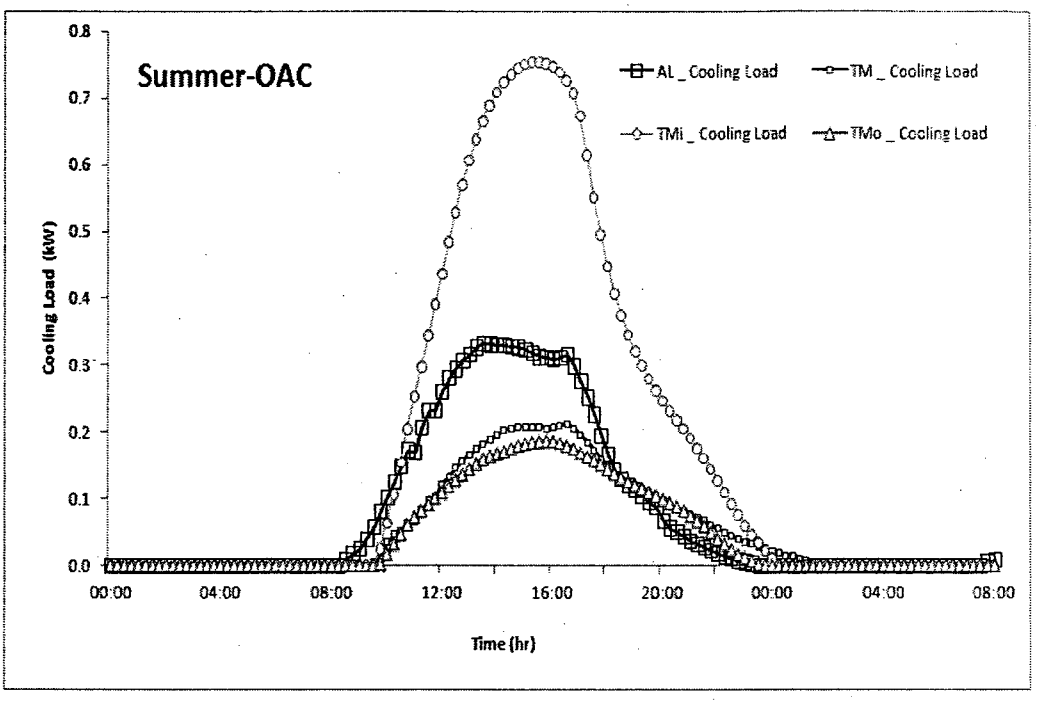

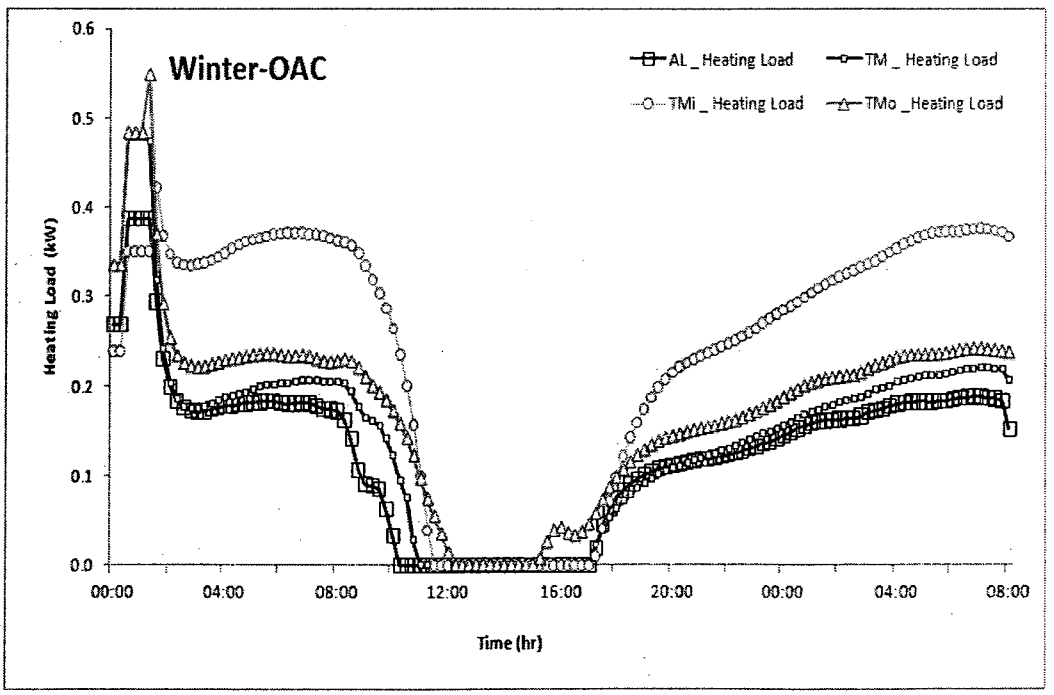

Figure 6.5: *Cooling/Heating load of attached room to DSF for various types of AL, TM, TMi & TMo with OAC airflow path direction in a sunny winter and summer day.*

Generally, in a naturally ventilated DSF, airflow rate is a function of outdoor climate conditions and the air channel's stack effect. Having thermal mass inside the air channel leads to higher surface temperatures of TM at nighttimes and evenings with respect to aluminum blind, thus increases the stack effect and the airflow. This airflow is favorable in summer and undesirable in winter. Figure 6.6 shows the percentage of increased airflow rate with thermal mass. In summer however, unlike TM, TMi and TMo, which have one side exposed to the air channel, are not capable of generating high stack effect. Therefore the daily average airflow rate is less than that of AL case. In winter, room temperature is higher than the ambient temperature, thus the closer the thermal mass is to interior layer, the hotter surface it has and the higher stack effect it generates. That is why TMo generates the lowest airflow rate in winter. TM and TMi both have high airflow rate increases. Also, keep in mind that TM inside the air channel has more surface area to interact and exchange heat; close profile of airflow rate increase of TM to TMi is expected.

In summer TM and TMo are capable of saving 27% and 40%, respectively. TM has similar savings to the mechanically-ventilated case. In other words, for the case of TM, method of ventilation (mechanical or natural) does not affect the energy saving in the cooling season. However, for the case of TMo, the energy saving halves with natural ventilation and there is no saving with TMi. This is due to lower stack effect generation in summer for these two, compared with AL.

Only in summer, increasing the amount of thermal mass is beneficial and leads to load decrease; in winter there is no energy saving that can be achieved by thermal mass.

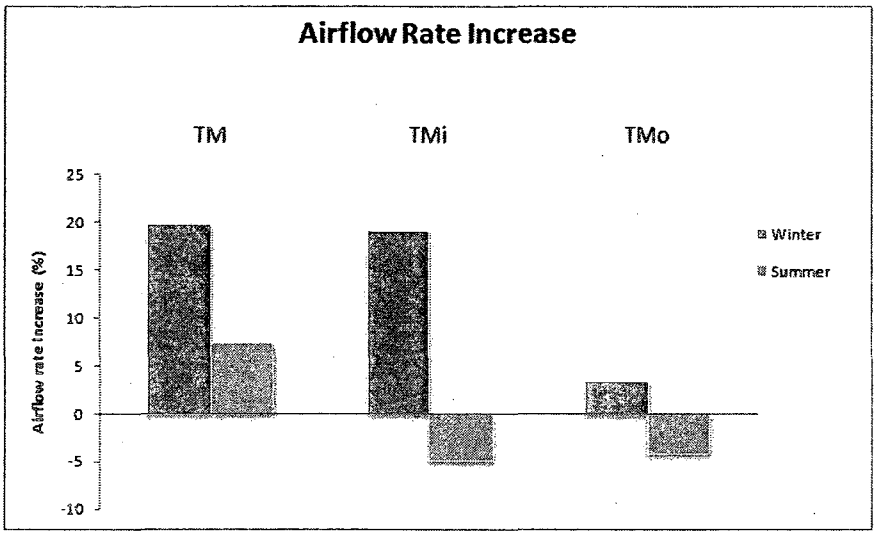

Figure 6.6: *The daily average of airflow rate increases through the air channel of DSF (NV-OAC) due to thermal mass effect as compared to AL.*

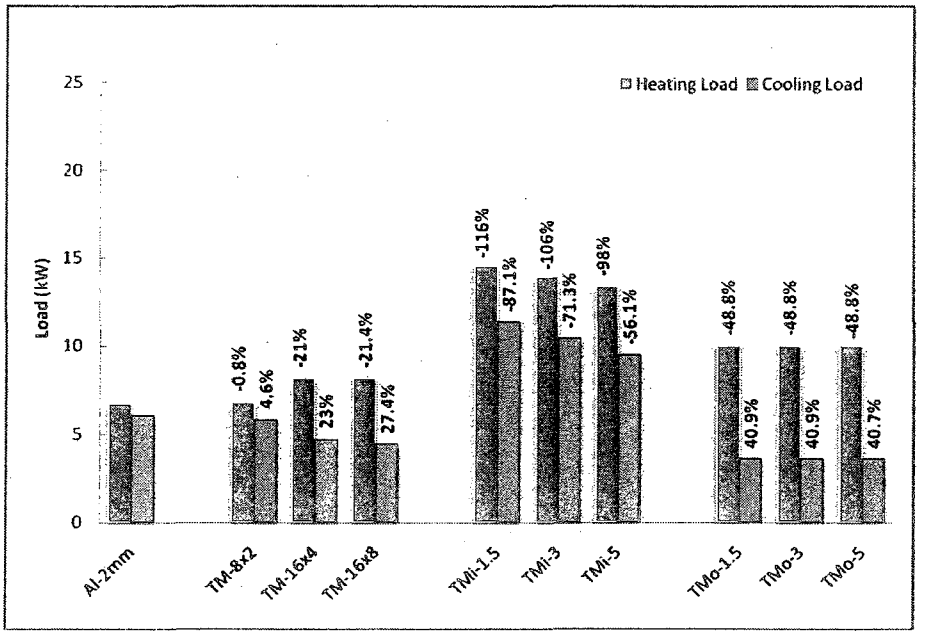

Figure 6.7: Cooling/Heating load of the attached room to naturally-ventilated DSF for various types of AL, TM, TMi & TMo with OAC configuration for a sunny winter and summer day. The values over charts represent energy saving in comparison with AL.

6.3 Conclusion

In this chapter energy performance of a DSF with different airflow path directions (IAC, SA, EA and OAC) was modeled both for mechanically and naturally ventilated DSF. Then a parametric study was conducted by replacing the inner glazing, outer glazing and shading device (TMi, TMo & TM) with concrete thermal mass in order to find potential achievable energy saving. The parametric study was done for both winter and summertime.

For the mechanically ventilated DSF, the parametric study revealed, in summer and winter, TM is superior to other thermal mass alternatives (TMi, TMo) and it is capable of reducing the heating/cooling loads. TM can save energy based on air channel configuration from 21% to 26% in summer and from 41% to 59% in winter. In summer, TMo and TMi both save energy and in some cases save much more than TM; however, in winter they show poor performance and the heating load is more than a conventional double-skin façade (AL). The parametric study also states that more energy efficiency is achievable for TM with sunny skies than for cloudy skies.

The modeling also showed that in a naturally ventilated DSF, concrete thermal mass is not appropriate. Though there are some savings achievable in summer; the winter performance is not improved compared to the conventional DSF (AL). This is due to increased stack effect and airflow rate within the air channel. TM and TMo are capable of

saving energy only in summer, the former due to its increased airflow rate compared to AL case and the latter due to its location, which is next to ambient air.

Overall, in terms of energy saving, a mechanically-ventilated DSF is a better option to place concrete thermal mass in rather than naturally-ventilated approach.

6.4 Building System Implementations

The innovative concept of integrating concrete thermal mass with DSF provides potentials for energy efficiency by thermal performance improvement and also by generating a time lag between peak solar radiation and the air channel's peak temperature. This can be implemented in other building systems. Two proposed implementations are listed below. However, these are preliminary ideas and their feasibility and suitability need more study and research.

6.4.1 Absorber Plate for Solar Thermal Collector

A water pipe is placed inside the thermal mass and the thermal mass acts as heat absorber from incident solar radiation and also as a heat exchanger with hot ventilation air of the DSF. This system can be used to preheat domestic hot water or circulating water loops in HVAC systems. The thermal mass is capable of preheating water hours after sunset.

Moreover, in contrast to solar collectors, placing thermal mass inside the air channel of a DSF reduces the concern of stored heat escaping to ambient air.

At nighttime in summer the cold air passing over the thermal mass can reduce the water temperature inside the pipe. Then the thermal mass keeps the temperature below ambient temperature for several hours in the morning.

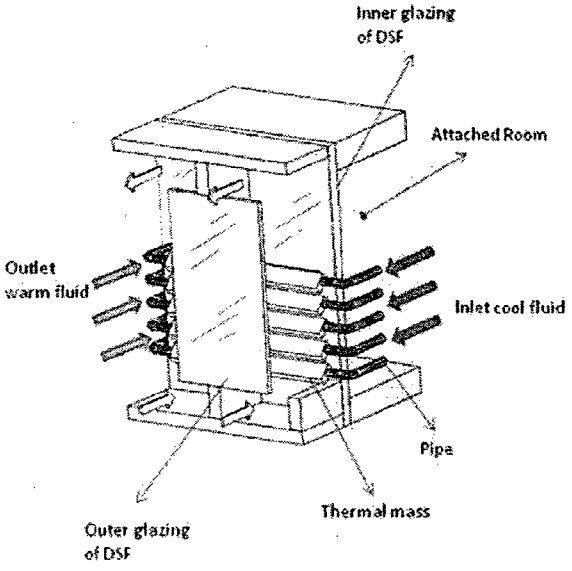

Figure 6.8: *Thermal mass as heat exchanger and absorber plate for solar thermal collector.*

6.4.2 Attic Ventilation

Vapour barriers provides resistance against water vapour penetrating through wall or roof assemblies. Figure 6.10 illustrates one common roofing system in which the vapour barrier is placed underside of the insulation to stop moisture penetration into the insulation from warm and moist indoor air during wintertime. If part of the moisture finds its way to the insulation layer and is trapped, there is a need for ventilation air to remove the moisture. Normally, ventilation over insulation is supplied from ambient air.

However, in cold wintertime, warm ventilation air exhausting from a DSF (OAC type) can be a good candidate to provide more opportunity for trapped moisture to be absorbed in comparison with cold ambient ventilation air. The table below compares the humidity ratio at different temperatures and states that at higher temperatures, moisture is removed at a higher rate.

T (c)	Humidity ratio at saturation kg/kg dry air	Incremental change per Kelvin
20	148×10^{-4}	9×10^{-4}
10	76×10^{-4}	5×10^{-4}
0	38×10^{-4}	3×10^{-4}
-10	16×10^{-4}	1.5×10^{-4}

Table 6.1: The ability of the air to hold water falls off rapidly with temperature reduction.

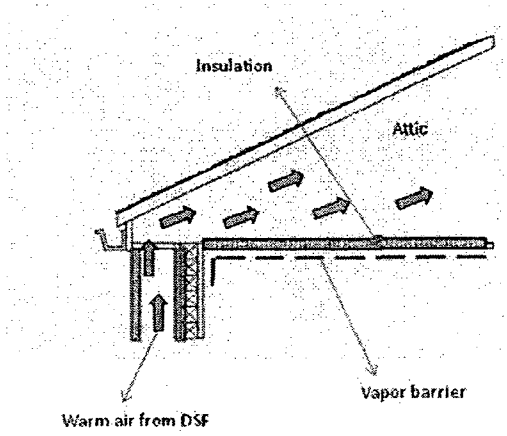

Figure 6.9: Attic vented with ventilation air exhausted from DSF

Moreover, by using the warm exhaust air of the DSF to vent the attic, a layer of warm air will surround the ceiling and heat losses through the ceiling decrease drastically; this leads to heating load decrease. Specially, a DSF combined with thermal mass keeps the air channel's temperature higher in the evening.

CHAPTER 7

CONCLUSION AND FUTURE WORK

In order to mitigate the overheating problem in the cooling season and to decrease the heating load in heating season that means improving thermal performance and energy efficiency of the system, this study introduced a new concept of integration of thermal mass with DSF. To investigate the thermal performance of proposed thermal mass a simple procedure was presented. This procedure is composed of airflow and thermal models of the air channel for both naturally and mechanically ventilated DSF. Based on the proposed procedure, naturally/mechanically ventilated base-cases were developed using building simulation software. The predictions of model were verified at two levels: with actual data obtained from test-cell facilities and with inter-model comparison. Generally, a good agreement was found between simulation results of base-cases and measured data from the test-cell. Also, inter-model verification confirmed that the results of base-case modeling are within the acceptable range of previous modeling results. Then a parametric study was conducted on the base-cases with different configurations of the air channel equipped with concrete thermal mass. The thermal performance of simulated cases was then compared with the conventional type of DSF.

In the following sections, the concluding remarks are summarized and recommendations for future work are addressed.

7.1 Concluding Remarks

Good agreement between simulated base-cases and measured data or inter-model comparison:

- The proposed methodology can be used to assess the performance of the DSF system with venetian blind and mechanically/naturally ventilated air channel by providing information which is in good agreement with measured data.

- Inter-model comparison with the zonal model for the case of a mechanically ventilated DSF showed also good agreement. The discrepancy between the two models increases at high solar radiation.

Sensitivity Analyses

- The results of parametric study showed that uncertainties due to modeling parameter assumptions cause more significant errors than uncertainties due to inaccuracy of sensors.

- The discharge coefficient (Cd) in airflow modeling and the subdivision of thermal zones in thermal modeling are the most important factors affecting accuracy of base-case models.

- Many modeling assumptions have minor effects on heating/cooling load of the attached room to the DSF as long as the air channel is not discharged to the room. Therefore, evaluation of the energy performance of a DSF which exhausts to indoor air or to an HVAC system should be done with care.

Mechanically Ventilated DSF combined with thermal mass

- For a mechanically ventilated DSF, the parametric study revealed that in summer and winter TM is superior to other thermal mass alternatives (TMi, TMo) and is capable of reducing heating/cooling load. TM can save energy based on configuration from 21% to 26% in summer and from 41% to 59% in winter.

- In summer TMo and TMi both save energy, and in some cases save much more than TM; however, in winter they show poor performance and the heating load is more than a conventional double-skin façade (AL).

- Generally in all cases, increasing the amount of thermal mass is beneficial and leads to load decrease in winter and summer. The best airflow path direction is EA.

- The parametric study also states that more energy efficiency is achievable for the TM with sunny skies than with cloudy skies.

Naturally Ventilated DSF combined with thermal mass

- Stack effect and therefore airflow rate inside of the air channel increases with increasing the amount of thermal mass.

- For a naturally ventilated DSF, concrete thermal mass is not appropriate. Though there are some savings achievable in summer, the winter performance is not improved compared with conventional DSF (AL).

- TM and TMo are capable of saving energy only in summer, TM due to its increased airflow rate compared with AL and TMo due to its location, which is next to ambient air.

- The type of ventilation (mechanical or natural) doesn't greatly affect energy saving associated with TM in summer. However, the saving for TMo halves with natural ventilation and there is no saving with TMi.

- In terms of energy saving, a mechanically ventilated DSF is a better option to place concrete thermal mass in rather than in a naturally ventilated type.

7.2 Future Work

Following the proposed procedure to measure the thermal performance of DSF and the comparison study of a conventional DSF with the one combined with thermal mass in previous chapters, future work may include:

1- **Annual performance of DSF with thermal mass:**

Due to lack of experimental data from both the conventional DSF test-cell and the one with thermal mass combined, the comparison in the current study was for typical days of summer and winter. There is a need for monitoring and analyzing the year-round thermal performance of conventional DSF and with thermal mass combined to have a better understanding and comparison of their thermal performances.

2- **Performance of DSF with thermal mass in different climates:**

Performance of thermal mass is closely related to the diurnal temperature difference of its surrounding air. In different climates, a different performance of DSF with thermal mass is expected.

3- Performance of DSF with thermal mass in different façade orientations or different glazing properties: Solar radiation penetrating through the outer skin of DSF varies based on façade orientation and glazing property of DSF. Therefore, orientation and glazing properties are between influential parameters and a study of these parameters to find the optimums can improve the performance of integrated DSF with thermal mass.

4- **Natural ventilation of perimeter zones to DSF with thermal mass and operable windows:** Some studies have been done on the potential of operable DSF to naturally ventilate the perimeter rooms during summer time (Gratia et al. 2007). A new configuration of the air channel with thermal mass (TM) can improve natural ventilation of attached rooms to the DSF on summer mornings.

5- **Combined effect of thermal mass and insulation inside the air channel of the DSF:** Insulation layers may be used with thermal mass to control discharge time. This can improve the thermal performance of the thermal mass.

7.3 Contributions:

- Proposing concept of integration of thermal mass technology with existing double-skin façade technology;

- Proposing a protocol to numerically study the thermal performance of double-skin façade;

- Developing base-case models using building energy simulation software for both naturally and mechanically ventilated DSFs based on set-ups of test-cell facilities;

- Modifying source code of building energy simulation software to imply proposed protocol;

- Calibrating naturally-ventilated base-case with measured data to obtain proper parameters for airflow modeling;

- Verifying developed base-case models with measured data and inter-model comparison;

- Sensitivity analysis of naturally-ventilated base-case model to identify the magnitude of errors may cause due to source of uncertainties such as sensor's inaccuracy and numerical modeling assumptions and parameters;

- Studying energy performance of proposed integrated thermal mass with DSF;

- Studying the effect of influential factors on the performance of proposed thermal mass in DSF such as airflow path direction, type of ventilation, season and thermal mass configuration and thickness inside the air channel.

REFERENCES

Alamdari F. and Hammond G. P. 1983. Improved data correlations for buoyancy-driven convection in rooms. Building Services Engineering Research Technology 4(3), pp. 106-12;

Allard F. and Santamouris M. 1998. Natural ventilation in buildings: a design handbook. James & James;

Antonopoulos K. A. and Koronaki E. P. 2000. Thermal parameter components of building envelope. Applied Thermal Engineering 20(13), pp. 1193-1211;

Artmann N., Sattelmayer T., Spinnler M. 2004. Double-skin façades with diverse sunscreen configurations. International Symposium on the Application of Architectural Glass;

Asan H., Sancaktar Y.S. 1998 .Effects of wall's thermophysical properties on time lag and decrement factor. Energy and Buildings, v 28, n 2, pp. 159-166;

ASHRAE Handbook Fundamentals. 2005. American Society of Heating, Refrigerating and Air-Conditioning Engineers, Inc., Atlanta;

Athienitis A. K., Charron R., 2006 .A two-dimensional model of a double-façade with integrated photovoltaic panels. Journal of Solar Energy Engineering, Transactions of the ASME, v 128, n 2, pp. 160-167;

Athienitis A. K., Charron R. 2006 . Optimization of the performance of double-façades with integrated photovoltaic panels and motorized blinds. Solar Energy 80, pp.482–491;

Aung W. 1972. Fully developed laminar free convection between vertical plates heated asymmetrically. International Journal of Heat and Mass Transfer, vol. 15, pp. 1577-1580;

Aung W., Fletcher L. S. and Sernas V. 1972. Developing laminar free convection between vertical flat plates with asymmetric heating. International Journal of Heat and Mass Transfer, vol. 15, pp. 2293-2308;

Balocco C. 2002. A simple model to study ventilated façades energy performance. Energy and Buildings 34, pp. 469-475;

Balocco C. 2004. A non-dimensional analysis of a ventilated double façade energy performance. Energy and Buildings 36, pp. 35–40;

Barakat SA. 1987. Thermal performance of a supply-air window. Proceedings of the 12th Annual Passive Solar Conference, 12, pp.152-158;

Bar-Cohen A., Rohsenow W.M. 1984. Thermally optimum spacing of vertical natural convection cooled parallel plates. Journal of Heat Transfer, pp. 106;

Bejan, A. 1984. Convection heat transfer. Wiley, New York;

Bejan, A. 1993. Heat transfer. Wiley, New York;

Bejan A., Lage J.L. 1990. The Prandtl number effect on the transition in natural convection along a vertical surface. Journal of Heat Transfer, vol. 112, pp. 787-790;

Berkovsky B. M., Polevikov V. K. 1977. Numerical study of problems of high-intensive free convection. Heat Transfer and Turbulent Buoyant Convection, Hemisphere;

Bodoia J.R., Osterle J.F. 1962. The development of free convection between heated vertical plates. Journal of Heat Transfer, vol. 84, pp. 40-44;

Boake T. M., Harrison K., Collins D., Balbaa T., Chatham A., Lee R., Andre B. 2001.The Tectonics of the double skin: Green Building or Just More Hi-Tech Hi-Jinx? What are

Double Skin Façades and How Do They Work? . University of Waterloo Research Articles on Double Skin Façades, Canada;

Chapra S.C. and Canale R.P., 2002. Numerical Methods for Engineers. McGraw Hill;

Churchill S.W., Ozoe H. 1973. Correlations for forced convection with uniform heating in flow over a plate and in developing and fully developed flow in a tube. Journal of Heat Transfer, vol. 95, pp. 78-84;

Clarke J. A. 2001. Energy Simulation in Building Design. Butterworth Heinemann, 2nd edition;

Corgnati S.P., Perino M. and Serra V. 2003. Energy performance evaluation of an innovative active envelope: results from a year round field monitoring. Proceedings of the 2nd International Conference on Building Physics, September 14-18, pp. 487–496.

Dickson A. 2004. Modelling double-skin façades. Master Thesis. University of Strathclyde, Glasgow UK;

Djunaedy E., Hensen J.L.M., Loomans M. 2002. A strategy for integration of CFD in building design. Proc. Roomvent. Danish Society of Heating, Refrigerating, and Air-Conditioning Engineers, Copenhagen;

ElSherbiny S. M., Raithby G.D., Hollands K.G.T..1982. Heat transfer by natural convection across vertical and inclined air layers. Journal of Heat Transfer, no 104, pp. 96102;

EnergyPlus. 2004. Engineering Manual: Documentation Version 1.2.1. Lawrence Berkeley National Laboratory with the U.S. Department of Energy;

ESRU. 1999. The ESP-r system for building energy simulations: User guide version 9 series- ESRU Manual U99/1. University of Strathclyde, Glasgow UK;

Feustel H.E., Dieris J. 1992. A survey of airflow models for multizone structures. Energy and Buildings 18, pp. 79-100;

Faggembauu D., Costa M., Soria M., Oliva A. 2003. Numerical analysis of the thermal behavior of ventilated glazed façades in mediterranean climates- Part I: development and validation of a numerical model. Solar Energy 75, pp. 217–228;

Faggembauu D., Costa M., Soria M., Oliva A. 2003. Numerical analysis of the thermal behavior of glazed ventilated façades in mediterranean climates- Part II: applications and analysis of results. Solar Energy 75, pp. 229–239;

Gratia E., De Herde A. 2003. Optimal operation of a south double-skin façade. Energy and Buildings 36, pp. 41–60;

Gratia E., De Herde A. 2004a. Is day natural ventilation still possible in office buildings with a double-skin façade?. Building and Environment 39, pp. 399 – 409;

Gratia E., De Herde A. 2004b. Natural cooling strategies efficiency in an office building with a double-skin façade. Energy and Buildings 36, pp. 1139–1152;

Gratia E., De Herde A. 2004c. Natural ventilation in a double-skin façade. Energy and Buildings 36, pp.137–146;

Gratia E., De Herde A. 2006. The most efficient position of shading devices in a double-skin façade. Energy and Buildings 39, pp. 364–373;

Gratia E., De Herde A. 2007a. Are energy consumptions decreased with the addition of a double-skin? . Energy and Buildings 39, pp. 605–619;

Gratia E., De Herde A. 2007b. Greenhouse effect in double-skin façade. Energy and Buildings 39, pp. 199–211;

Gratia E., De Herde A. 2007c. Guidelines for improving natural daytime ventilation in an office building with a double-skin façade. Solar Energy 81, pp. 435–448;

Haddad K. H., Elmahdy A.H. 1998. Comparison of the monthly thermal performance of a conventional window and a supply-air window. ASHRAE Transactions, v 104, pp. 1261-1270;

Haddad K. H., Elmahdy A.H. 1999. Comparison of the thermal performance of an exhaust-air window and a supply-air window. ASHRAE Transactions, Vol. 105, Part 2.SE-99-12-4.

Hamza N., Underwood C. 2005. CFD Supported modeling of double-skin façade in hot arid climates, Ninth International IBPSA Conference, Montréal, Canada;

Hamza N. 2008. Double versus single skin façades in hot arid areas, Energy and Buildings 40, pp. 240–248;

Heiselberg P., Kalyanova O., Jensen R. L. 2008. Empirical validation data sets for double skin façade models, Proceedings: The First International Conference on Building Energy and Environment, pp. 2450;

Heiselberg P., Kalyanova O., Jensen R. L. 2008. Measurement and modeling of air flow rate in a naturally ventilated double skin façade, Proceedings: The First International Conference on Building Energy and Environment, pp. 1895;

Hensen J., Bartak M. and Drkal F. 2002. Modelling and simulation of a double-skin façade system. ASHRAE Transactions 108(2), pp. 1251-9;

Holmes, M. J. 1994. Optimization of the thermal performance of mechanically and naturally ventilated glazed façades. Renewable Energy 5, pp. 1091-1098;

Holmes M.J., Hanby V.I., Cook M.J. 2008. Infield D.G., Ji Y., Loveday D.L. and Mei L. Nodal network and CFD simulation of airflow and heat transfer in double skin façades with blinds. Building Serv. Eng. Res. Technol. 29-1, pp. 45–59;

Høseggen R.,Wachenfeldt B.J.,Hanssen S.O. 2008. Building simulation as an assisting tool in decision making Case study: With or without a double-skin façade?. Energy and Buildings 40, pp. 821–827;

Hutcheon N.B., Handegord G. O. P. 1995. Building science for a cold climate. Institute for research in construction;

IEA Annex 44, 2008. Integrating environmentally responsive elements in buildings. ECBCS Publications (Draft Version);

Incropera, F.P. De Witt, D.P. 1981. Fundamentals of heat transfer. John Wiley and Sons, New York;

Ismail K.A.R., Henriquez J.R. 2005. Two-dimensional model for the double glass naturally ventilated window. International Journal of Heat and Mass Transfer 48, pp. 461–475;

Jiru T. E. 2006. A new generation of zonal models: development, verification and application. PhD thesis, Concordia University, Montreal, Canada;

Kalogirou S. A., Florides G. and Tassou S.. 2002. Energy analysis of buildings employing thermal mass in Cyprus. Renewable Energy 27(3), pp. 353-368;

Khalifa A. J. N., Marshall R. H. 1990. Validation of heat transfer coefficient on interior building surface using a real-sized interior test cell. Int. J. Heat Mass Transfer 33(10), pp. 2219-36;

Li S. 2001. A Protocol to Determine the Performance of South Facing Double Glass Façade System: A Preliminary Study of Active/Passive Double Glass Façade Systems. M.S. Thesis, Virginia Polytechnic Institute and State University, Blacksburg, Virginia;

Loncour X., Deneyer A., Blasco M., Flamant G., WoutersP. 2004. Ventilated double façades: classification & illustration of façade concepts, Belgian Building Research Institute (BBRI),

http://www.bbri.be/activefaçades/new/index.cfm?cat=7_documents&sub=1_download ;

Manz H. 2003. Numerical simulation of heat transfer by natural convection in cavities of façade elements. Energy and Buildings 35, pp. 305–311;

Manz H., Schaelin A., Simmler H. 2004. Air flow patterns and thermal behavior of mechanically ventilated glass double façades. Building and Environment 39, pp. 1023 – 1033;

Manz H. 2004. Total solar energy transmittance of glass double façades with free convection. Energy and Buildings 36, pp. 127–136;

Manz H., Frank T.H. 2005. Thermal simulation of buildings with double-skin façades. Energy and Buildings 37, pp. 1114–1121;

Marques da Silva F., Gomes M. G., Pinto A., Pereira A. I., Moret Rodrigues A. 2006. Double-skin façade thermal monitoring. Proceedings of the Healthy Buildings, vol. III, Lisbon, Portugal, pp. 111–116;

McEvoy M.E., Southall S.G. 2000. Validation of a computational fluid dynamics simulation of a supply air ventilated window. CISBE Conference, Dublin, Ireland;

McEvoy M.E., Southall R. G., Baker P. H. 2003. Test cell evaluation of supply air windows to characterize their optimum performance and its verification by these modeling techniques. Energy and Buildings 35, pp. 1009-1020;

Pappas, A. 2006. Energy modeling of a double skin façade: A method using CFD & energyPlus. M.S. thesis, Department of civil engineering, University of Colorado at Boulder;

Pappas A., Zhai Zh. 2008. Numerical investigation on thermal performance and correlations of double skin façade with buoyancy-driven airflow. Energy and Buildings 40, pp. 466–475;

Park C.S., Augenbroea G., Sadegh N., Thitisawata M., Messadic T. 2004a. Real-time optimization of a double-skin façade based on lumped modeling and occupant preference. Building and Environment 39, pp. 939 – 948;

Park C.S., Augenbroea G., Sadegh N., Thitisawata M., Messadic T. 2004b. Calibration of a lumped simulation model for double-skin façade systems. Energy and Buildings 36, pp. 1117–1130;

Perez-Grande I., Meseguer J., Alonso G. 2005. Influence of glass properties on the performance of double-glazed façades. Applied Thermal Engineering 25, pp. 3163–3175;

Perino M. 2005. IEA-ECBCS Annex 44: Subtask A-contribution to the state of the art report;

Perino M., Micono C., Serra V., Zanghirella F. & Filippi M., 2006. Performance assessment of innovative transparent active envelopes through measurements in test cells measurements in test cells. Research in Building Physics and Building Engineering, Taylor & Francis Group, London;

Perino M., Corgnati S. P., Serra V. 2007. Experimental assessment of the performance of an active transparent façade during actual operating conditions. Solar Energy 81, pp. 993–1013;

Pfrommer P., Lomas K. J., Kupke C. 1996. Solar radiation transport through slat-type blinds: A new model and its application for thermal simulation of buildings. Solar Energy, Vol. 57, No. 2, pp.77-91;

Rohsenow W.M., Harnett J.P., Ganic E.P. 1985. Handbook of Heat Transfer Fundamentals. McGraw-Hill, New York;

Rheault S., Bilgen E. 1989. Heat transfer analysis in an automated venetian blind window system, Journal of Solar Energy Engineering, Vol.111, No.1, pp. 89-95;

Saelens D., Hens H. 2001. Experimental evaluation of airflow in naturally ventilated active envelopes. Department of Civil Engineering, Laboratory of Building Physics, Catholic University of Leuven;

Saelens D. 2002. Energy performance assessment of single storey multiple-skin façades. Katholike University Leuven . Belgium;

Saelens D., Carmeliet J., and Hens H., 2003, Energy performance assessment of multiple skin façades, International Journal of HVAC&R Research., vol. 9, no. 2, pp.167-186;

Saelens D., Roels S., Hens H., 2004. The inlet temperature as a boundary condition for multiple-skin façade modeling. Energy and Buildings 36, pp. 825–835;

Saelens D., Blocken B., Roels S., Hens H. 2005. Optimization of the energy performance of multiple-skin façades. Building Simulation 2005, Ninth International IBPSA Conference, Montreal, Canada;

Saelens D., Roels S., Hens H. 2008. Strategies to improve the energy performance of multiple-skin façades. Building and Environment 43, pp. 638–650;

Safer N.,Woloszyn M., Roux J. J. 2005. Three-dimensional simulation with a CFD tool of the airflow phenomena in single floor double-skin façade equipped with a venetian blind . Solar Energy 79, pp. 193–203;

Stec W.J., van Paassen A.H.C. 2005. Symbiosis of the double skin façade with the HVAC system. Energy and Buildings 37, pp. 461–469;

Sun L., Jones P. J., Alexander D. K. 2008. Energy efficiency of double-skin façade in office buildings of Shanghai. Proceedings of the first international conference on building energy and environment, pp. 1887;

Szokolay S. 1984. Passive and low energy design for thermal and visual comfort. 3rd Int. PLEA Conf. Mexico City, pp. 11-28;

Tanimoto J., Kimura K. 1997. Simulation study on an air flow window system with an integrated roll screen. Energy and Buildings 26, pp. 317-325;

TRNSYS. 2004. TRNSYS: A transient simulation program, reference manual. Wisconsin Solar Energy Laboratory, University of Wisconsin-Madison;

Von Grabe J. 2002. A prediction tool for the temperature field of double façades, Energy and Buildings 34, pp. 891–899;

Walton G.N. 1982. Airflow and multi-room thermal analysis. ASHRAE Trans. 88(2), pp. 78-91;

Walton GN. 1984. A computer algorithm for predicting infiltration and inter-room airflows. ASHRAE Transactions 90 (1), pp. 601-610;

Walton GN. 1989. Airflow network models for element-based building airflow modeling. ASHRAE Transactions 95 (2), pp. 613-620;

Yamada T., Ding W., Hasemi Y. 2005. Natural ventilation performance of a double-skin façade with a solar chimney, Energy and Buildings 37, pp. 411–418;

Zerefos C. S. 2007. On the performance of double skin façades in different environmental conditions. International Journal of Sustainable Energy Vol. 26, No. 4, pp. 221–229;

Zollner A., Winter E.R.F., Viskanta R. 2002. Experimental studies of combined heat transfer in turbulent mixed convection fluid flows in double-skin-façades. International Journal of Heat and Mass Transfer 45, pp. 4401–4408;

Zukauskas A., Ziugzda J. 1985. Heat transfer of a cylinder in crossflow. Hemisphere Publ. Corp. Washington D.C., pp. 208.

APPENDIX A

AIRFLOW MODELING

The wind at a building site will be influenced by the upstream surface roughness, so it is necessary to make a correction to the observed wind speeds to take into consideration of surface roughness and height above ground. Based on an analysis of the underlying physics, Simiu & Scalan R. H. (1986) suggested a logarithmic form for the wind profile:

$$\frac{V_i}{V_m} = \frac{V_i^*}{V_m^*}\left(\ln\frac{z_i - d_i}{z_{o,i}} \Big/ \ln\frac{z_m - d_m}{z_{o,m}}\right) \tag{A.1}$$

$$\frac{V_i^*}{V_m^*} \approx \left(\frac{z_{o,i}}{z_{o,m}}\right)^{0.1}$$

Terrain	Z_o	d
Open flat country	0.03	0.0
Country, Scattered wind breaks	0.1	0.0
Rural	0.5	0.7h
Urban	1.0	0.8h
City	>2.0	0.8h

h = building height (m)

Table A.1: Values of terrain parameters

where V_i is the local wind speed at a height Z_i above the ground; V_m the free stream wind speed measured at some reference height Z_m (m/s); V_i^*, V_m^* the atmospheric friction speed (m/s) ; $Z_{o,i}$, $Z_{o,m}$ a terrain dependent roughness length (m) and d_i, d_m are terrain displacement lengths (m). Table A.1 shows the typical values for these two parameters.

APPENDIX B

CONVECTION

As figure B.1 shows, convective heat transfer can be divided into three groups:

1. Convective heat transfer between ambient air and a DSF's outer surface (h_{out}): External convection coefficients are calculated based on the empirical relationship between wind speed, wind direction and surface orientation.

2. Convective heat transfer inside double-skin façade (h_{cav1}, h_{cav2}, h_{cav3} & h_{cav4}): The internal surface convective transfer process is particularly important in double façades and much attention has been focused on this element in this research.

3. Convective heat transfer inside room zones adjacent to double-skin façade (h_{in}): as default, a family of correlations that cover both buoyant and mechanically induced convective regimes (as found within a building) is used.

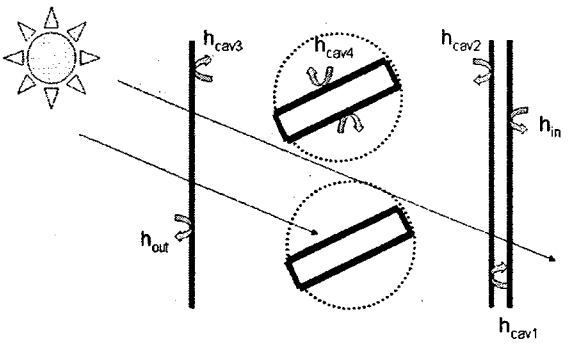

Figure B.1: Convection heat transfer coefficient

The reminder of Appendix B explains how to calculate the above mentioned convective heat transfers. Most of correlations were reported by Saelens (2002).

B.1 Ambient air and DSF's Outer Surface (h_{out})

Based on an air reference temperature of 21C, McAdams (1982) proposed the following expression:

$$h_c = 5.678\left[a + b\left(\frac{V}{0.3048}\right)^n\right] \qquad \text{(B-1)}$$

where h_c is the forced convection coefficient (W/m^2C), *a, b & n* are empirical values and *V* the parallel component of the flow velocity (m/s). These values can be obtained from the table below. For non-reference temperatures, a simple adjustment to the velocity term is required: $294.26V/(273.16+\theta_n)$, where θ_n is the non-reference temperature (C).

	V < 4.88 m/s			4.88 ≤ V < 30.48 m/s		
Nature of surface	**a**	**b**	**n**	**a**	**b**	**n**
Smooth	0.99	0.21	1	0	0.50	0.78
Rough	1.09	0.23	1	0	0.53	0.78

Table B.1: Empirical coefficients and exponents for McAdams correlation

B.2 Inside double-skin façade

B.2.1Convection coefficient in enclosed cavity (h_{cavl})

For low aspect ratio enclosures with isothermal walls, the Berkovsky & Polevikov relationship may be useful to determine the convective heat transfer:

$$Nu_H = 0.22\left(\frac{\mathrm{Pr}}{0.2+\mathrm{Pr}}Ra_H\right)^{0.28}\left(\frac{1}{A}\right)^{0.09} \qquad (2 < A < 10,\ \mathrm{Pr} < 10^5,\ \mathrm{Ra_H} < 10^{13}) \qquad \text{(B-2)}$$

In (B-2) equation characteristic length for dimensionless numbers is the height of cavity. For high aspect ratio, the experimental results of El-Sherbiny et al. (1982) can be applied (Saelens, 2002). The characteristic length in the definitions of the Nusselt and Rayleigh number is the cavity depth L; the temperature difference is the temperature difference between the hot and the cold pane. The results for air (Pr≈ 0.72) may be summarized by the following set of equations:

$$Nu_L = \max\left(Nu_L^{ct} + Nu_L^{l} + Nu_L^{t}\right) \tag{B-3}$$

$$Nu_L^{ct} = \left(1+\left(\frac{0.104Ra_L^{0.293}}{1+(6310/Ra_L)^{1.36}}\right)^3\right)^{1/3} \tag{B-4}$$

$$Nu_L^{l} = 0.242\left(\frac{Ra_L L}{H}\right)^{0.273} \tag{B-5}$$

$$Nu_L^{t} = 0.0605Ra_L^{1/3} \tag{B-6}$$

In this set of relations, the superscript "ct" refers to the conduction and the turbulent transition regime. The superscript "l" describes the laminar boundary-layer regime and "t" refers to the turbulent boundary-layer regime.

The maximum Rayleigh number for which these relations have been validated depends on the aspect ratio and is listed in table below. The equations approximate the data within 10%; the mean deviation is 4%. The relations are valid for perfectly conducting walls. Following Rohsenow et al. (1985), the effect of the wall properties is not expected to be important for aspect ratios A > 10.

aspect ratio A (A = H/L)	5	20	40	80	110
maximum Rayleigh number (Ra_L)	10^6	2×10^6	2×10^5	3×10^4	1.2×10^4

Table B.2 : Relationship between the maximum Rayleigh number and aspect ratio for which El-Sherbiny equation is valid.

B.2.2 Convection coefficient between blind and cavity air (h_{cav4})

The convective heat transfer between the cavity air and the blind (h_{cav4}) can be modeled by assuming each of the slats to be a long cylinder in cross flow in the ambient air. For natural convection wide a range of Rayleigh number, Churchill & Chu (1975) correlation is used with properties at (Ts + T∞) /2 and the characteristic length is the assumed cylinder's diameter:

$$\overline{Nu}_D = \left\{ 0.60 + \frac{0.387 Ra_D^{1/6}}{[1+(0.599/\mathrm{Pr})^{9/16}]^{8/27}} \right\}^2 \qquad Ra_D \le 10^{12} \qquad \text{(B-7)}$$

For forced convection, Zukauskas (1985) correlation for a cylinder at uniform temperature Ts :

$$\overline{Nu}_D = \frac{\overline{h}_c D}{k} = C\left(\frac{U_\infty D}{V}\right)^m \mathrm{Pr}^n \left(\frac{\mathrm{Pr}}{\mathrm{Pr}_s}\right)^{0.25} \qquad \text{(B-8)}$$

where all fluid properties are evaluated at the free stream fluid temperature except for Pr_s, which is evaluated at the surface temperature. For Pr < 10, n=0.37, and for Pr>10, n=0.36. Again, the characteristic length is the assumed cylinder's diameter.

Re_D	C	m
1 - 40	0.75	0.4
$40 - 1 \times 10^3$	0.51	0.5
$1 \times 10^3 - 2 \times 10^5$	0.26	0.6
$2 \times 10^5 - 1 \times 10^6$	0.076	0.7

Table B.3 : Empirical coefficients and exponents for Zukauskas correlation

For mixed convection, Incropera & De Witt (1981) suggested the following limits (the characteristic length is the height of the channel):

$Gr_H >> Re^2_H$ natural convection (B-9a)

$Gr_H \approx Re^2_H$ mixed convection (B-9b)

$Gr_H << Re^2_H$ forced convection (B-9c)

B.2.3 Convection coefficient between inner surface of double skin façade and cavity air (h_{cav2} & h_{cav3})

The flow in naturally and mechanically ventilated cavities is fundamentally different. Therefore, the development of expressions describing the convective heat transfer will be split into two parts.

B.2.3.1 Natural Convection in Ventilated Cavity

a. Wide cavities

When the wide channel limit holds:

$$\frac{L}{H} > Ra_H^{-1/4} \quad \text{or} \quad \frac{L}{H} > Ra_L^{-1} \qquad \text{(B-10)}$$

where L and H are the depth and the height of the cavity. The surface heat transfer can be calculated from single wall formulas. Churchill & Chu (1975) developed empirical

correlations for averaged heat transfer rate from a vertical wall. The following equations are valid for uniform wall temperature:

$$Nu_H = 0.68 + 0.515 Ra_H^{1/4} \qquad \text{Laminar regime } (Gr_H < 10^9) \qquad \text{(B-11)}$$

$$Nu_H = (0.825 + 0.325 Ra_H^{1/6})^2 \qquad \text{Laminar and turbulent regime } (10^{-1} < Ra_H < 10^{12}) \qquad \text{(B-12)}$$

b. Narrow cavities

If the wide channel criterion no longer holds, relations for flow between plates are used. For parallel isothermal plates Aung (1972) has shown that in the fully developed (fd) regime (valid for very high cavities), the heat transfer from both plates to the fluid can be estimated by:

$$Nu_{L,fd} = \frac{4T^{*2} + 7T^* + 4}{90(1+T^*)^2} Ra_L \frac{L}{H} \approx \frac{1}{24} Ra_L \frac{L}{H} \qquad (Ra\ L/H < 10) \qquad \text{(B-13a)}$$

$$T^* = \frac{T_{s,1} - T_\infty}{T_{s,2} - T_\infty} \qquad (1 \le T^* \le 1) \qquad \text{(B-13b)}$$

The Nusselt number is based on the temperature difference between the wall surface and the inlet temperature; the characteristic length is the depth of cavity. For higher Rayleigh numbers ($Ra_L\ L/H > 10^3$), a laminar boundary layer (bl) regime establishes. The observed values of the Nusselt number have the following form:

$$Nu_{L,bl} = C\left(Ra_L \frac{L}{H}\right)^{1/4} \qquad (Ra_L\ L/H > 10^3) \qquad \text{(B-13c)}$$

The analysis of Bodoia & Osterle (1962) and Aung et al. (1972) indicate a value of $c \approx$ 0.68. These values are approximately 17% higher than the corresponding values obtained for a single vertical isothermal plate in fully developed regime. Following Rohsenow et al. (1985) the latter equations can be combined into:

$$Nu_L = \left(\left(Nu_{L,fd} \right)^{-1.9} + \left(Nu_{L,bl} \right)^{-1.9} \right)^{1.9} \qquad \text{(B-13d)}$$

The Nusselt number is based on the temperature difference between the wall surface and the inlet temperature.

B.2.3.2 Forced Convection in Ventilated Cavity

a. Entrance region

For laminar flow along an isothermal wall, Bejan & Kraus (1993) give a similar solution for the average Nusselt number from the boundary layer theory:

(H height of the channel)

$$\overline{Nu}_H = 0.664 \, \mathrm{Pr}^{1/3} \, \mathrm{Re}_H^{\,1/2} \qquad (\mathrm{Pr} > 0.5) \qquad \text{(B-14)}$$

The Nusselt number is based on the temperature difference between the wall surface and the inlet temperature.

b. Fully developed flow

For hydrodynamically and thermally fully developed laminar flows ($x > 0.05 \, Re_{Dh}$ and $x > 0.05 \, Re_{Dh} \, Pr$) the Nusselt number is invariant with tube length and independent of the Reynolds number. Bejan (1984) tabulates the Nusselt numbers for internal flows with

constant wall temperature. The results for flows between parallel plates are $Nu_{Dh} = 7.541$ for uniform and equal wall temperatures. The characteristic length is the channel's hydraulic diameter (Dh).

c. Turbulent regime

An empirical relationship for the local Nusselt number along an isothermal vertical wall in turbulent regime is given by Bejan (1984).

$$Nu_x \approx 0.0296 \mathrm{Pr}^{1/3} \mathrm{Re}_x^{4/5} \quad (\mathrm{Pr} > 0.5) \qquad \text{(B-15)}$$

A combination of the above relationship for turbulent flow and the entrance region equation for laminar flow (above equation) gives a relationship for the average Nusselt number, valid for lengths that exceed the transition length:

(B-16a)

$$Nu_H = 0.664 \mathrm{Pr}^{1/3} \mathrm{Re}_{x,tr}^{1/2} + 0.0296 \mathrm{Pr}^{1/3} \left(\mathrm{Re}_H^{4/5} - \mathrm{Re}_{x,tr}^{4/5} \right) \quad (\mathrm{Pr} > 0.5)$$

where $Re_{x,tr}$ is the Reynolds number at the position of transition estimated by

$$\frac{X}{D_H} \cong \frac{X_T}{D_H} \cong 10 \qquad \text{(B-16b)}$$

B.2.3.3 Mixed Convection in Ventilated Cavity

The average heat transfer for laminar assisting flow conditions with isothermal boundary condition has been correlated by Chu & Churchill (1977):

$$Nu_H = \left(\left(Nu_{H,na} \right)^3 + \left(Nu_{H,for} \right)^3 \right)^{1/3} \quad \text{(B-17)}$$

where $Nu_{H,nat}$ and $Nu_{H,for}$ are the Nusselt numbers for pure natural and forced convection over a single wall which were derived before.

B.3 Indoor Air and DSF's Inner Surface (h_{in}):

A correlation from Khalifa & Marshall (1990) that covers both buoyant and mechanically induced convective regimes in the range of building was used (Clark 2001):

Location	Applicability	h_c correlation
Wall	• room heated by radiator • radiator located under window • wall surface adjacent to radiator	$2.30\ \Delta\theta^{0.24}$
Window	• room heated by radiator • radiator located under window	$8.07\ \Delta\theta^{0.11}$
Ceiling	• room heated by radiator • radiator located under window	$3.10\ \Delta\theta^{0.17}$

$\Delta\theta$ is the surface-to-air temperature difference.

Table B.4 : h_c correlation suggested by Khalifa and Marshall

APPENDIX C

SHORT-WAVE SOLAR RADIATION

In mathematically formulating the direct, diffuse and reflected solar radiation and long-wave radiation between surfaces, the theoretical model suggested by Rheault et al. (1989) and reported by Park C. (2003) was used with some modifications in order to take into account the thickness of blind.

C.1 Shape Factor

The shape factors between each surface and sky and ground are calculated as indicated in figure C.1.

$$F_{1,1} = 0 \qquad F_{1,3} = 1 - \sin(\frac{90 - \varphi}{2})$$

$$F_{1,2} = 1 - \sin(\frac{90 + \varphi}{2}) \qquad F_{1,4} = 1 - F_{1,2} - F_{1,3} = \sqrt{2}\cos(\frac{\varphi}{2}) - 1$$

Symmetry and reciprocity rule:

$$F_{2,1} = F_{1,2} \quad F_{2,2} = 0 \quad F_{2,3} = F_{1,4} \quad F_{2,4} = F_{1,3}$$

$$F_{3,1} = F_{1,3} \quad F_{3,2} = F_{2,3} \quad F_{3,3} = 0 \quad F_{3,4} = F_{1,2}$$

$$F_{4,1} = F_{1,4} \quad F_{4,2} = F_{2,4} \quad F_{4,3} = F_{3,4} \quad F_{4,4} = 0$$

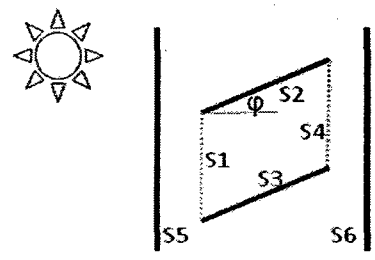

Figure C.1: fictitious surface between two slats

To calculate diffuse (solar + ground) solar radiation, the shape factors between surfaces 1) to 4) and sky and ground are determined, based on the following assumptions:

1) $F_{3,1}$ accounts for $F_{3,sky}$ and $F_{3,gr}$

2) $F_{3,sky}$ increases as φ increases , as in a wall with surface tilt angle φ.

3) $F_{4,1}$ accounts for $F_{4,sky}$ and $F_{4,gr}$

4) $F_{4,sky}$ decreases as φ increases.

For example, the following equations can be derived based on the above assumptions.

$$F_{3,1} = F_{3,sky} + F_{3,gr}$$

	$0 \le \varphi \le 90$	$-90 \le \varphi < 0$
$F_{2,sky}$	0	$(1-\cos\varphi)/2$
$F_{2,gr}$	$F_{2,1}$	$F_{2,1}- [(1-\cos\varphi)/2]$
$F_{3,sky}$	$F_{3,1}- [(1-\cos\varphi)/2]$	$F_{3,1}$
$F_{3,gr}$	$(1-\cos\varphi)/2$	0
$F_{4,sky}$	$F_{4,1}$ $(1-\sin\varphi)/2$	
$F_{4,gr}$	$F_{4,1}$ $(1+\sin\varphi)/2$	

Table C.1: View factors of slats at different tilt angles

C.2 Reflectance, Transmittance and Absorptance

According to the ray tracing method, the fraction of incident energy reflected by the glazing is the sum of the terms leaving an incident surface:

$$R = \rho\left[1 + \frac{(1-\rho)^2\tau^2}{1-\rho^2\tau^2}\right] \tag{C.1}$$

The fraction transmitted is the sum of terms leaving the opposite surface:

$$T = \tau\left[\frac{1-\rho}{1+\rho}\right]\left[\frac{(1-\rho)^2\tau^2}{1-\rho^2\tau^2}\right] \tag{C.2}$$

The fraction of energy absorbed is:

$$A = \frac{(1-\rho)(1-\tau)}{1-\rho\tau} \tag{C.3}$$

If the reflectance at the incident surface and the opposite surface are not equal (for the case of low-e glazing), the results for R and T are as follows:

$$R = \frac{\rho_1 + \rho_2(1-2\rho_1)\tau^2}{1-\rho_1\rho_2\tau^2} \tag{C.4}$$

$$T = \tau\left[\frac{(1-\rho_1)(1-\rho_2)\tau}{1-\rho_1\rho_2\tau^2}\right] \tag{C.5}$$

C.3 Permeability

To consider the effect of blind located inside the air channel at a given sun altitude (Figure C.2), the permeability p is defined as the ratio between the unshaded area and the total area between the blinds, and can be expressed as (Pfrommer, 1996):

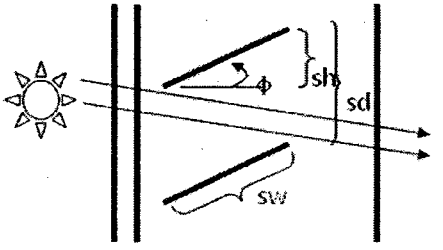

Figure C.2:2D Geometry of blind

$$p = \frac{sd - sh}{sd} = 1 - \left|\cos\varphi \tan\beta - \sin\varphi\right| \tag{C.6}$$

where sh is the shaded area and β is the solar altitude and φ is the slat's tilt angle. A positive blind slat angle (degrees from horizontal) permits building occupants to view the sky, while a negative blind slat angle permits view of the ground. p can be used to

describe the amount of direct solar radiation reaching the interior glazing. For example, the direct solar radiation reaching the interior glazing I_{g3} (the single glazing on the right in figure C.4) is:

$I_{g3} = p\, \tau_{D,g1}\, \tau_{D,g2}\, I_D$

where $\tau_{D,g1}$ and $\tau_{D,g2}$ are the transmittance of the outer and inner pane of exterior double glazing for direct solar radiation, and I_D is the direct solar radiation incident on the exterior glazing.

C.4 Slat Thickness Correction Factor

In order to take into account the fraction of radiation incident which is reflected and absorbed on the edge of slats, a correction factor was considered for transmittance, reflectance and absorptance properties of the blind. This is illustrated in figure C.3 for the case of direct radiation incident on the blind. The quantity of interest is the fraction, f_{edge}, of direct radiation incident on the blind that strikes the slat edges. Based on the geometry shown in figure C.3 (EnergyPlus engineering manual, 2008):

$$f_{edge} = \frac{t\cos\gamma}{(sd + \frac{t}{\cos\zeta})\cos\beta} = \frac{t\cos(\beta-\zeta)}{(sd + \frac{t}{\cos\zeta})\cos\beta} = \frac{t\cos(\varphi'-\beta)}{(sd + \frac{t}{\sin\varphi'})\cos\beta} \qquad \text{(C.7)}$$

Where β is the solar altitude and φ′ is the edge of slat's tilt angle (if slat cross section is a rectangle then φ=90 - φ while φ is the slat's tilt angle). t is slat thickness and sd is the distance between two adjacent slats.

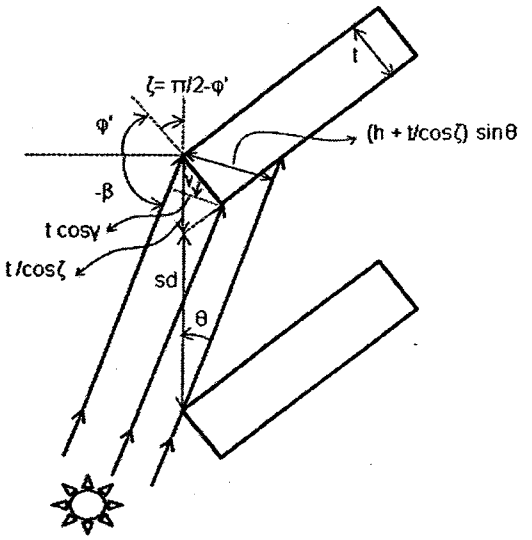

Figure C.3: Geometry of slat edge correction factor for incident direct radiation

The edge correction factor for diffuse incident radiation is calculated by averaging this value of edge over profile angles, φs, from –90 degrees to +90 degrees.

The following two equations are examples of how the edge correction factor is applied.

$p \rightarrow$ *(after correction)* $(1-f_{edge})\,p$

$(1-p) \rightarrow$ *(after correction)* $(1+f_{edge})(1-p)$

C.5 Absorbed Solar Radiation

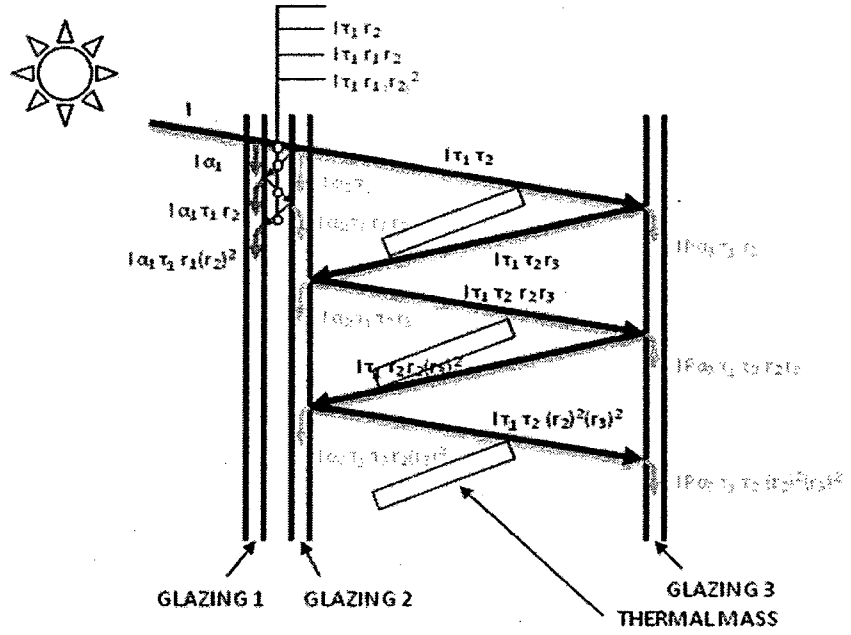

Figure C.4: Multiple reflections between glazing and blind; α, τ & r are total absororptance, transmittance and reflectance of each glazing layer and blind slat.

The solar radiation absorbed by each surface can be formulated as (Park, C. 2003):

a) *GLAZING 1:*

$$q_{s,g1,out} = q_{g1,i} + q_{g1,ii} \tag{C.8}$$

where $q_{g1,i}$ is absorbed direct and diffuse solar radiation (direct, diffuse sky, diffuse ground absorbed by glazing 1)

$$q_{g1,i} = \alpha_{D,1} I_D A_1 + \alpha_{d,1}\left(I_{d,sky} + I_{d,gr}\right)A_1 \tag{C.9}$$

$q_{g1,\ ii}$ is absorbed direct and diffuse solar radiation by multiple reflections between glazing 1 and glazing 2

$$q_{g1,ii} = \frac{\alpha_{D,1}\ \tau_{D,1}\ r_{D,2}}{1 - r_{D,1}\ r_{D,2}} I_D\ A_1 + \frac{\alpha_{d,1}\ \tau_{d,1}\ r_{d,2}}{1 - r_{d,1}\ r_{d,2}} \left(I_{d,sky} + I_{d,gr}\right) A_1 \qquad \text{(C.10)}$$

b) ***GLAZING 2:***

$$q_{s,g2,out} = q_{g2,\ i} + q_{g2,\ ii} + q_{g2,\ iii} \qquad \text{(C.11)}$$

where $q_{g2,\ i}$ is absorbed direct and diffuse solar radiation (direct, diffuse sky, diffuse ground absorbed by glazing 2)

$$q_{g2,i} = \alpha_{D,2}\tau_{D,1} I_D\ A_2 + \alpha_{d,2}\tau_{d,1}(I_{d,sky} + I_{d,gr})\ A_2 \qquad \text{(C.12)}$$

$q_{g2,\ ii}$ is absorbed direct and diffuse solar radiation by multiple reflections between glazing 1 and glazing 2:

$$q_{g2,ii} = \frac{\alpha_{D,2}\ \tau_{D,1}\ r_{D.1} r_{D,2}}{1 - r_{D,1}\ r_{D,2}} I_D\ A_2 + \frac{\alpha_{d,2}\ \tau_{d,1} r_{d,1}\ r_{d,2}}{1 - r_{d,1}\ r_{d,2}} \left(I_{d,sky} + I_{d,gr}\ \right) A_2 \qquad \text{(C.13)}$$

$R_{\ 2,\ iii}$ is absorbed direct and diffuse solar radiation by multiple reflections between glazing 2 and glazing 3 and blind slats (or thermal mass):

$$q_{g2,iii} = \frac{\alpha_{D,2}\ \tau_{D,1}\ \tau_{D,2}\ r_{e,D,2}}{1 - r_{D,2}\ r_{e,D,2}} I_D\ A_2 + \frac{\alpha_{d,2}\ \tau_{d,1}\ \tau_{d,2}\ r_{e,d,2}}{1 - r_{d,2}\ r_{e,d,2}} \left(I_{d,sky} + I_{d,gr}\ \right) A_2 \qquad \text{(C.14)}$$

where $r_{e,D,2}$ and $r_{e,d,2}$ are equivalent reflectance for multiple reflections of direct radiation and for multiple reflections of diffuse radiation between glazing 2, glazing 3 and blind slats (or concrete thermal mass) respectively.

The equivalent reflectance $r_{e,D,2}$ accounts for what bounces back from the blind slats and glazing 3 to glazing 2, simply assumed to be proportional to a sum of multiplication of the shape factor between surfaces and the reflectance of each surface (Park, C-S, 2003). Surely, this assumption that the reflected rays from surface i to j has a linear relationship with the shape factor from surface i to j, doesn't explain exactly the complex processes of directional reflections between curved blinds slats and glazing, but to some extent, this concept is practical and takes into consideration the complex reflections.

$$r_{e,D,2} = F_{2,3} r_{D,3} + F_{2,1} r_{D,1} \tag{C.15}$$

$$r_{e,d,2} = F_{2,3} r_{d,3} + F_{2,1} r_{d,1} \tag{C.16}$$

c) ***GLAZING 3:***

$$q_{s,g3,out} = q_{3g,i} + Q_{3g,ii} \tag{C.15}$$

where $Q_{3g,i}$ is absorbed direct and diffuse solar radiation (direct, diffuse sky, diffuse ground absorbed by glazing 3) :

(C.16)

$$q_{3g,i} = \alpha_{D,3}\tau_{D,1}\tau_{D,2} p \left(1 - f_{edge,D}\right) I_D A_3 + \alpha_{d,3}\tau_{d,1}\tau_{d,2} F_{4,sky} \left(1 - f_{edge,diff}\right)(I_{d,sky} + I_{d,gr}) A_3$$

$Q_{3g,\,ii}$ is absorbed direct and diffuse solar radiation by multiple reflections between glazing 2 and glazing 3 and blind slats (or concrete thermal mass):

$$q_{3g,ii} = \frac{\alpha_{D,3}\,\tau_{D,1}\,\tau_{D,2}\,p\left(1-f_{edge,D}\right)r_{D,3}\,r_{e,D,3}}{1-r_{D,3}\,r_{e,D,3}} I_D\,A_3 \qquad \text{(C.17)}$$

$$+\frac{\alpha_{d,3}\,\tau_{d,1}\,\tau_{d,2}\,r_{d,3}\,r_{e,d,3}}{1-r_{d,3}\,r_{e,d,3}}\left(1-f_{edge,diff}\right)\left(F_{4,sky}I_{d,sky}+F_{4,gr}I_{d,gr}\right)A_3$$

where $r_{e,D,3}$ and $r_{e,d,3}$ are equivalent reflectances for multiple reflections of direct radiation and for multiple reflections of diffuse radiation between glazing 2, glazing 3 and blind slats (or thermal mass) respectively, defined as:

$$r_{e,D,3} = F_{3,2}r_{D,2} + F_{3,bld}r_{D,bld} \qquad \text{(C.18)}$$

$$r_{e,d,3} = F_{3,2}r_{d,2} + F_{3,bld}r_{d,bld} \qquad \text{(C.19)}$$

d) *Blind Slats (concrete thermal mass):*

$$q_{bld\,out} = q_{bld,\,i} + q_{bld,\,ii} \qquad \text{(C.20)}$$

where $q_{bld,\,i}$ is absorbed direct and diffuse solar radiation (direct, diffuse sky, diffuse ground absorbed by blind slat) :

(C.21)

$$q_{bld,i} = \alpha_{D,bld}\tau_{D,1}\tau_{D,2}(1+f_{edge,D})(1-p)I_D\,A_{bld}$$
$$+\alpha_{d,bld}\tau_{d,1}\tau_{d,2}(1+f_{edge,D})\left(F_{2,sky}+F_{3,sky}\right)I_{d,sky}\,A_{bld}$$
$$+\alpha_{d,bld}\tau_{d,1}\tau_{d,2}(1+f_{edge,D})\left(F_{2,gr}+F_{3,gr}\right)I_{d,gr}\,A_{bld}$$

$Q_{bld,ii}$ is absorbed direct and diffuse solar radiation by multiple reflections between glazing 2 and glazing 3 and blind slats (or thermal mass):

$$q_{bld,ii} = \frac{\alpha_{D,bld}\ \tau_{D,1}\ \tau_{D,2}\ r_{D,bld}\ (1+f_{edge,D})(1-p)r_{e,D,bld}}{1-r_{D,bld}\ r_{e,D,bld}} I_D\ A_{bld} + \frac{\alpha_{d,bld}\ \tau_{d,1}\ \tau_{d,2}\ r_{d,bld}\ r_{e,d,bld}}{1-r_{d,bld}\ r_{e,d,bld}}(1+f_{edge,D}) \left[\left(F_{2,sky}+F_{3,sky}\right)I_{d,sky}+\left(F_{2,gr}+F_{3,gr}\right)I_{d,gr}\right]A_{bld} \quad \text{(C.22)}$$

where $r_{e,L}$ is equivalent reflectance for multiple reflections of direct radiation and for multiple reflections of diffuse radiation between glazing 2, glazing 3 and blind slats (or thermal mass) respectively, defined as:

$$r_{e,D,bld} = F_{bld,2}r_{D,2} + F_{bld,3}r_{D,3} \quad \text{(C.23)}$$

$$r_{e,d,bld} = F_{bld,2}r_{d,2} + F_{bld,3}r_{d,3} \quad \text{(C.24)}$$

APPENDIX D

LONG-WAVE RADIATION

The long-wave radiation between two panes of double glazing can be expressed as:

$$q_{LW,g1-g2} = \frac{A\sigma\left(T_1^4 - T_2^4\right)}{\frac{1}{\varepsilon_1} + \frac{1}{\varepsilon_2} - 1} \tag{D.1}$$

Within an enclosure the radiation emitted by all surfaces will, after multiple reflections, be totally absorbed and redistributed. The initial fluxes emitted by each surface are tracked to first reflection and surface absorptions determined (Clarke. 2001). For example, for four grey surfaces in an enclosure the flux emitted is:

$$q_1 = A_1\varepsilon_1\sigma T_1^4 \qquad q_3 = A_3\varepsilon_3\sigma T_3^4$$

$$q_2 = A_2\varepsilon_2\sigma T_2^4 \qquad q_4 = A_4\varepsilon_4\sigma T_4^4$$

And, at first reflection, the absorption at each surface will have contribution as follows

$$\begin{cases} a_1' = & +q_2F_{2,1}\varepsilon_1 & +q_3F_{3,1}\varepsilon_1 & +q_4F_{4,1}\varepsilon_1 \\ a_2' = q_1F_{1,2}\varepsilon_2 & & +q_3F_{3,2}\varepsilon_2 & +q_4F_{4,2}\varepsilon_2 \\ a_3' = q_1F_{1,3}\varepsilon_3 & +q_2F_{2,3}\varepsilon_3 & & +q_4F_{4,3}\varepsilon_3 \\ a_4' = q_1F_{1,4}\varepsilon_4 & +q_2F_{2,4}\varepsilon_4 & +q_3F_{3,4}\varepsilon_4 & \end{cases} \tag{D.2}$$

where a_i' is the total flux absorption at surface I from all surfaces after the first reflection and Fi,j is the geometric view factor between surface j and i. A single flux quantity can now be determined for each surface that presents the total apparent flux emission for processing the next reflection:

$$r_i' = a_i'(1-\varepsilon_i)/\varepsilon_i \quad ; i = 1,2,3,4 \tag{D.3}$$

where r_i' is the flux reflected at surface I after first reflection. After the second reflection, the total absorption at each surface is given by:

$$\begin{cases} a_1'' = a_1' + r_2'F_{2,1}\varepsilon_1 + r_3'F_{3,1}\varepsilon_1 + r_4'F_{4,1}\varepsilon_1 \\ a_2'' = a_2' + r_1'F_{1,2}\varepsilon_2 + r_3'F_{3,2}\varepsilon_2 + r_4'F_{4,2}\varepsilon_2 \\ a_3'' = a_3' + r_1'F_{1,3}\varepsilon_3 + r_2'F_{2,3}\varepsilon_3 + r_4'F_{4,3}\varepsilon_3 \\ a_4'' = a_4' + r_1'F_{1,4}\varepsilon_4 + r_2'F_{2,4}\varepsilon_4 + r_3'F_{3,4}\varepsilon_4 \end{cases} \tag{D.4}$$

where a_i'' is the total absorption of flux at surface I from all surfaces after the second reflection. Then the flux reflections are:

$$\begin{cases} r_1'' = (a_1'' - a_1')(1-\varepsilon_1)/\varepsilon_1 \\ r_2'' = (a_2'' - a_2')(1-\varepsilon_2)/\varepsilon_2 \\ r_3'' = (a_3'' - a_3')(1-\varepsilon_3)/\varepsilon_3 \\ r_4'' = (a_4'' - a_4')(1-\varepsilon_4)/\varepsilon_4 \end{cases} \tag{D.5}$$

where the absorptions and reflections at each recursive step may be determined from

$$a_i^n = a_i^{n-1} + \sum_{j=1}^{N} r_j^{n-1} F_{j,i}\varepsilon_i \tag{D.6}$$

$$r_i^n = (a_i^n - a_j^{n-1})(1-\varepsilon_i)/\varepsilon_i \tag{D.7}$$

$(1 \le n < \infty \ ; \ a_i^0 = 0 \ ; \ r_i^0 = q_i \ ; \ F_{i,j} = 0)$

and in practice the recursive process continues until the reflected flux is reduced to insignificance.

APPENDIX E

HEAT BALANCE EQUATIONS

Based on energy paths illustrated in chapter 3 figure 3.8, heat balances at every discrete node are expressed as the following set of equations.

E.1 Outer glazing of ventilated & non-ventilated channels ($Tg1_{out}$ & $Tg3_{in}$)

If node I is located at outer surface of glazing 1 exposed to ambient air then the general equation 3.21 is modified to find T(g1-out, t+Δt):

(E.1)

$$\left[2\rho_{g1}(t+\Delta t)\,C_{g1}(t+\Delta t)+\frac{\Delta t\,k_{g1}(t+\Delta t)}{\Delta x^{2}}+\frac{\Delta t\,h_{c,g1out}(t+\Delta t)}{\Delta x}+\frac{\Delta t\sum_{s=1}^{n}h_{r_s,g1out}(t+\Delta t)}{\Delta x}\right]T(g1_{out},t+\Delta t)-$$

$$\left[\frac{\Delta t\,k_{g1}(t+\Delta t)}{\Delta x^{2}}\right]T(g1_{mid},t+\Delta t)-\left[\frac{\Delta t\,h_{c,g1out}(t+\Delta t)}{\Delta x}\right]T(amb,t+\Delta t)-$$

$$\frac{\Delta t\sum_{s=1}^{n}h_{r_s,g1out}(t+\Delta t)\,T(S,t+\Delta t)}{\Delta x}-\frac{\Delta t\left[q_{R-g1out}(t+\Delta t)+q_{S-g1out}(t+\Delta t)\right]}{\Delta x\;A_{g1out}}=$$

$$\left[2\rho_{g1}(t)\,C_{g1}(t)-\frac{\Delta t\,k_{g1}(t)}{\Delta x^{2}}-\frac{\Delta t\,h_{c,g1out}(t)}{\Delta x}-\frac{\Delta t\sum_{s=1}^{n}h_{r_s,g1out}(t)}{\Delta x}\right]T(g1_{out},t)+$$

$$\left[\frac{\Delta t\,k_{g1}(t)}{\Delta x^{2}}\right]T(g1_{mid},t)+\left[\frac{\Delta t\,h_{c,g1out}(t)}{\Delta x}\right]T(amb,t)+$$

$$\frac{\Delta t\sum_{s=1}^{n}h_{r_s,g1out}(t)\,T(S,t)}{\Delta x}+\frac{\Delta t\left[q_{R-g1out}(t)+q_{S-g1out}(t)\right]}{\Delta x\;A_{g1out}}$$

where, T(s) can be the sky, ground or surrounding temperature. A_g is the cross section area at node $T_{g1\ out}$. $hc_{g1\ out}$ is the convection coefficient between the outer surface of glazing1 and the ambient air (Appendix B), $hr_{s,\ g1\ out}$ is the long-wave radiation coefficient with sky, ground and surrounding (Appendix D). q_s is short-wave energy absorption (Appendix C). q_R is casual heat gains, which in this case wherein the thermal air node is located in the ambient air, is equal to zero. Δx is the half of distance between surface node and middle node.

The formulation to find $T(g3_{in} , t+\Delta t)$ can be written similar to above equation by replacing (figure 3.8):

$Tg1_{out} = Tg3_{in}$; $Tg1_{mid} = Tg3_{mid}$; $T\ amb = T\ room$; $\rho_{g1\ out} = \rho_{g3\ in}$

$C_{g1\ out} = C_{g3\ in}$; $k_{g1\ out} = k_{g3\ in}$; $hc_{g1\ out} = hc_{g3\ in}$; $hr_{g1\ out} = hr_{g3\ in}$

$q_{R\text{-}g1\ out} = q_{R\text{-}g3\ in}$; $q_{S\text{-}g1\ out} = q_{S\text{-}g3\ in}$

$hr_{g1\ out}$ is long-wave radiation with walls, ceiling and roof of the room. $q_{R\text{-}g3\ in}$ is casual gains of the room, and unlike the outer glazing case, can have values more than zero. $q_{S\text{-}g3\ in}$ is the short-wave radiation reflecting back from the interior surface of the room on glazing3.

E.2 Interior glazing of non-ventilated channels ($Tg1_{in}$ &$Tg2_{out}$)

For the case in which node I is located at the outer surface of glazing 2, exposed to the non-ventilated air channel, then the general equation 3.21 is modified to find T(g2-out, t+Δt):

(E.2)

$$\left[2\rho_{g2}(t+\Delta t)\,C_{g2}(t+\Delta t)+\frac{\Delta t\,k_{g2}(t+\Delta t)}{\Delta x^{2}}+\frac{\Delta t\,h_{c,g2\,out}(t+\Delta t)}{\Delta x}+\frac{\Delta t\sum_{s=1}^{n}h_{r_s,g2\,out}(t+\Delta t)}{\Delta x}\right]T(g2_{out},t+\Delta t)-$$

$$\left[\frac{\Delta t\,k_{g2}(t+\Delta t)}{\Delta x^{2}}\right]T(g2_{mid},t+\Delta t)-\left[\frac{\Delta t\,h_{c,g2\,out}(t+\Delta t)}{\Delta x}\right]T(g_{mo-vent},t+\Delta t)-$$

$$\frac{\Delta t\sum_{s=1}^{n}h_{r_s,g2\,out}(t+\Delta t)\,T(S,t+\Delta t)}{\Delta x}-\frac{\Delta t\left[q_{S-g2\,out}(t+\Delta t)\right]}{\Delta x\;A_{g2\,out}}=$$

$$\left[2\rho_{g2}(t)\,C_{g2}(t)-\frac{\Delta t\,k_{g2}(t+\Delta t)}{\Delta x^{2}}-\frac{\Delta t\,h_{c,g2\,out}(t)}{\Delta x}-\frac{2\Delta t\sum_{s=1}^{n}h_{r_s,g2\,out}(t)}{\Delta x}\right]T(g2_{out},t)+$$

$$\left[\frac{\Delta t\,k_{g2}(t)}{\Delta x^{2}}\right]T(g2_{mid},t)+\left[\frac{\Delta t\,h_{c,g2\,out}(t)}{\Delta x}\right]T(g_{mo-vent},t)+$$

$$\frac{\Delta t\sum_{s=1}^{n}h_{r_s,g2\,out}(t)\,T(S,t)}{\Delta x}+\frac{\Delta t\left[q_{S-g2\,out}(t)\right]}{\Delta x\;A_{g2\,out}}$$

where T(s) can be glazing 1 or an imaginary surface temperatures. A_g is the cross section area at node $T_{g2\ out}$. $hc_{g2\ out}$ is the convection coefficient between the outer surface of glazing2 and the non-ventilated channel (Appendix B), $hr_{s,\ g2\ out}$ is the long-wave

radiation coefficient with glazing 1 and imaginary surfaces (Appendix D). q_s is short-wave energy absorption (Appendix C). Δx is half of the distance between surface node and middle node.

The formulation to find T($g1_{in}$, $t+\Delta t$) can be written similar to above equation by replacing:

$Tg2_{out} = Tg1_{in}$; $Tg2_{mid} = Tg1_{mid}$; $C_{g2\,out} = C_{g1\,in}$; $\rho_{g2\,out} = \rho_{g1\,in}$

$hr_{g2\,out} = hr_{g1\,in}$; $k_{g2\,out} = k_{g1\,in}$; $hc_{g2\,out} = hc_{g1\,in}$

$hr_{g1\,out}$ is long wave-radiation with glazing2 and non-ventilated channel (Appendix D). Δx is the half distance between surface node and middle node.

E.3 Interior glazing of ventilated channels and blind ($Tg2_{in}$, $Tg3_{out}$, $Tbld_{in}$ & $Tbld_{out}$)

There are four surfaces of façade layers exposed to the ventilated air channel. Here node I is assumed to be located on each of this exposed surfaces to obtain the Crank-Nicolson formulation. If node I is assumed to be on the outer surface of glazing1, then T(g3out,t+Δt) is modification of general equation 3.21:

(E.3)

$$\left[2\rho_{g3}(t+\Delta t)\,C_{g3}(t+\Delta t)+\frac{\Delta t\,k_{g3}(t+\Delta t)}{\Delta x^{2}}+\frac{\Delta t\,h_{c,g3\,out}(t+\Delta t)}{\Delta x}+\frac{\Delta t\sum_{s=1}^{n}h_{r_S,g3\,out}(t+\Delta t)}{\Delta x}\right]T(g3_{out},t+\Delta t)-$$

$$\left[\frac{\Delta t\,k_{g3}(t+\Delta t)}{\Delta x^{2}}\right]T(g3_{mid},t+\Delta t)-\left[\frac{\Delta t\,h_{c,g3out}(t+\Delta t)}{\Delta x}\right]T(g\,p_{ent-in},t+\Delta t)-$$

$$\frac{\Delta t\sum_{s=1}^{n}h_{r_S,g3\,out}(t+\Delta t)\,T(S,t+\Delta t)}{\Delta x}-\frac{\Delta t\left[q_{S-g3\,out}(t+\Delta t)\right]}{\Delta x\;A_{g3\,out}}=$$

$$\left[2\rho_{g3}(t)\,C_{g3}(t)+\frac{\Delta t\,k_{g3}(t)}{\Delta x^{2}}+\frac{\Delta t\,h_{c,g3\,out}(t)}{\Delta x}+\frac{\Delta t\sum_{s=1}^{n}h_{r_S,g3\,out}(t)}{\Delta x}\right]T(g3_{out},t)-$$

$$\left[\frac{\Delta t\,k_{g3}(t)}{\Delta x^{2}}\right]T(g3_{mid},t)-\left[\frac{\Delta t\,h_{c,g3out}(t)}{\Delta x}\right]T(g\,p_{ent-in},t)-$$

$$\frac{\Delta t\sum_{s=1}^{n}h_{r_S,g3\,out}(t)\,T(S,t)}{\Delta x}-\frac{\Delta t\left[q_{S-g3\,out}(t)\right]}{\Delta x\;A_{g3\,out}}$$

where,

T(s) and $hr_{s,\ g3\ out}$ arethe surface temperature and long-wave radiation coefficient of the blind and imaginary surfaces. A_g is the cross section area at node $T_{g3\ out}$. $hc_{g3\ out}$ is the convection coefficient between outer surface of glazing1 and ventilated channel (Appendix B), $hr_{s,\ g2\ out}$ is the long-wave radiation coefficient with glazing1 and imaginary surfaces (Appendix D). Δx is half distance between surface node and middle node.

The formulation for $T(g2_{in} , t+\Delta t)$ can be written similar to the above equation by replacing:

$Tg3_{out} = Tg2_{in}$; $Tg3_{mid} = Tg2_{mid}$; $C_{g3\ out} = C_{g2\ in}$; $\rho_{g3\ out} = \rho_{g2\ in}$

$hr_{g3\ out} = hr_{g2in}$; $k_{g3\ out} = k_{g2\ in}$; $hc_{g3\ out} = hc_{g2\ in}$

For $T(bld_{in} , t+\Delta t)$ by replacing,

$Tg3_{out} = Tbld_{in}$; $Tg3_{mid} = Tbld_{mid}$; $C_{g3\ out} = C_{bld\ in}$; $\rho_{g3\ out} = \rho_{bld\ in}$

$hr_{g3\ out} = hr_{bld\ in}$; $k_{g3\ out} = k_{bld\ in}$; $hc_{g3\ out} = hc_{bld\ in}$

And for $T(bld_{out} , t+\Delta t)$,

$Tg3_{out} = Tbld_{out}$; $Tg3_{mid} = Tbld_{mid}$; $C_{g3\ out} = C_{bld\ out}$; $\rho_{g3\ out} = \rho_{bld\ out}$

$hr_{g3\ out} = hr_{bld\ out}$; $k_{g3\ out} = k_{bld\ out}$; $hc_{g3\ out} = hc_{bld\ out}$; $q_{S\text{-}g3\ out} = q_{S\text{-}bld\ out}$

E.4 Interior nodes of blind and glazings (Tgl_{mid}, $Tg2_{mid}$, $Tg3_{mid}$ & $Tbld_{mid}$)

If node I is located inside of façade layers (glazing 1-3 and blind) then general equation 3.19 needs to be applied. The formulation for temperature distribution of node I in the middle of blind $T(bld_{mid}, t+\Delta t)$ is:

(E.4)

$$\left[2\rho_{bld}(t+\Delta t)\,C_{bld}(t+\Delta t)+\frac{\Delta t\,k_{bld}(t+\Delta t)}{\Delta x^2}\right]T(b\,d_{midl},t+\Delta t)-$$
$$\left[\frac{\Delta t\,k_{bld}(t+\Delta t)}{\Delta x^2}\right]T(bld_{in},t+\Delta t)-\left[\frac{\Delta t\,k_{bld}(t+\Delta t)}{\Delta x^2}\right]T(bld_{out},t+\Delta t)-\frac{\Delta t\,q\,s_{bld\ mid}(t+\Delta t)}{\Delta x\,A_{bld\ mid}}=$$
$$\left[2\rho_{bld}(t)\,C_{bld}(t)-\frac{\Delta t\,k_{bld}(t)}{\Delta x^2}\right]T(bld_{mid},t)+\left[\frac{\Delta t\,k_{bld}(t)}{\Delta x^2}\right]T(bld_{in},t)+$$
$$\left[\frac{\Delta t\,k_{bld}(t)}{\Delta x^2}\right]T(bld_{out},t)+\frac{\Delta t\,q\,s_{bld}(t)}{\Delta x\,A_{bld\ mid}}$$

The formulation for $T(gl_{mid}, t+\Delta t)$ can be written similar to the above equation by replacing:

$Tbld_{mid} = Tgl_{mid}$; $Tbld_{in} = Tgl_{in}$; $Tbld_{out} = Tgl_{out}$; $\rho_{bld\ mid} = \rho_{gl\ mid}$

$C_{bld\ mid} = C_{gl\ mid}$; $k_{bld\ mid} = k_{gl\ mid}$; $q_{S\text{-}bld\ mid} = q_{S\text{-}gl\ mid}$

For $T(g2_{mid}, t+\Delta t)$ by replacing,

$Tbld_{mid} = Tg2_{mid}$; $Tbld_{in} = Tg2_{in}$; $Tbld_{out} = Tg2_{out}$; $\rho_{bld\ mid} = \rho_{g2\ mid}$

$C_{bld\ mid} = C_{g2\ mid}$; $k_{bld\ mid} = k_{g2\ mid}$; $q_{S\text{-}bld\ mid} = q_{S\text{-}g2\ mid}$

And for T($g3_{mid}$, t+Δt),

$Tbld_{mid} = Tg3_{mid}$; $Tbld_{in} = Tg3_{in}$; $Tbld_{out} = Tg3_{out}$; $\rho_{bld\ mid} = \rho_{g3\ mid}$

$C_{bld\ mid} = C_{g3\ mid}$; $k_{bld\ mid} = k_{g3\ mid}$; $q_{S\text{-}bld\ mid} = q_{S\text{-}g3\ mid}$

E.5 Air nodes of ventilated & non-ventilated channels ($Tgap_{no\text{-}vent}$, $Tgap_{vent\text{-}in}$ & $Tgap_{vent\text{-}out}$)

Now we consider node I located at the inner ventilated air channel between the blind and glazing 3. After applying general equation 9.23 for T($gap_{vent\text{-}in}$, t+Δt) we have,

(E.5)

$$\left[2\rho_{gapvent-in}(t+\Delta t)\,C_{gapvent-in}(t+\Delta t)+\frac{\Delta t\ h_{c,g3out}(t+\Delta t)}{\Delta x}+\frac{\Delta t\ h_{c,bld\,in}(t+\Delta t)}{\Delta x}\right]T(gap_{vent-in},t+\Delta t)-$$
$$\left[\frac{\Delta t\ h_{c,g3out}(t+\Delta t)}{\Delta x}\right]T(g3_{out},t+\Delta t)-\left[\frac{\Delta t\ h_{c,bld\,in}(t+\Delta t)}{\Delta x}\right]T(bd_{in},t+\Delta t)-$$
$$\frac{\Delta t\left(q_{V,gap\,vent-in}(t+\Delta t)\right)}{\Delta x}=$$

$$\left[2\rho_{gapvent-in}(t)\,C_{gapvent-in}(t)+\frac{\Delta t\ h_{c,g3out}(t)}{\Delta x}+\frac{\Delta t\ h_{c,bld\,in}(t)}{\Delta x}\right]T(gap_{vent-in},t)-$$
$$\left[\frac{\Delta t\ h_{c,g3out}(t)}{\Delta x}\right]T(g3_{out},t)-\left[\frac{\Delta t\ h_{c,bld\,in}(t)}{\Delta x}\right]T(bld_{in},t)-\frac{\Delta t\left(q_{V,gap\,vent-in}(t)\right)}{\Delta x}$$

where, $q_{vent\text{-}in}$ is advection heat transfer due to the temperature difference of inlet and outlet ventilation air. $h_{c,\ g3\ out}$ and $h_{c,\ bld\ in}$ are convection coefficients of the blind and glazing 3 with inner ventilated channel. Δx is the width of the inner ventilated channel.

The formulation for $T(gap_{\ vent\text{-}out}\ ,\ t+\Delta t\ )$ can be written similar to above equation by replacing:

$Tgap_{\ vent\text{-}in} = Tgap_{\ vent\text{-}out}$; $Tbld_{\ in} = Tbld_{\ out}$; $Tg3_{\ out} = Tg2_{in}$; $\rho_{gap\ vent\text{-}in} = \rho_{\ gap\ vent\text{-}out}$

$C_{gap\ vent\text{-}in} = C_{\ gap\ vent\text{-}out}$; $h_{c,bld\ in} = h_{c,bld\ out}$; $h_{c,g3\ out} = h_{c,g2\ in}$

For $T(gap_{\ no\text{-}vent}\ ,\ t+\Delta t\ )$ by replacing,

$Tgap_{\ vent\text{-}in} = Tgap_{\ no\text{-}vent}$; $Tbld_{\ in} = Tg1_{\ in}$; $Tg3_{\ out} = Tg2_{out}$; $\rho_{gap\ vent\text{-}in} = \rho_{\ gap\ no\text{-}vent}$

$C_{gap\ vent\text{-}in} = C_{\ gap\ no\text{-}vent}$; $h_{c,bld\ in} = h_{c,g1\ in}$; $h_{c,g3\ out} = h_{c,g2\ out}$

APPENDIX F

AIR CHANNEL CONFIGURATION

Characteristics of applied concrete thermal mass and aluminum blind are tabulated in table F.1. The aluminum slats' cross section, which is rectangular, has dimensions of 8cm×2mm, but the concrete slats come in three different dimensions: 8cm×2cm, 16cm×4cm and 16cm×8cm. The concrete slabs are 1.5cm, 3cm and 5cm thick.

The configuration and spacing between slats were considered so that the mass of the 1.5cm concrete slab is equivalent to mass of the 8cm×2cm concrete slats and the same between 3cm and 16cm×4cm and between 5cm and 16cm×8cm concrete slab. The difference is merely in the amount of surface area they expose to the air channel. Concrete slats have twice the surface exposed to the air channel compared with concrete slabs.

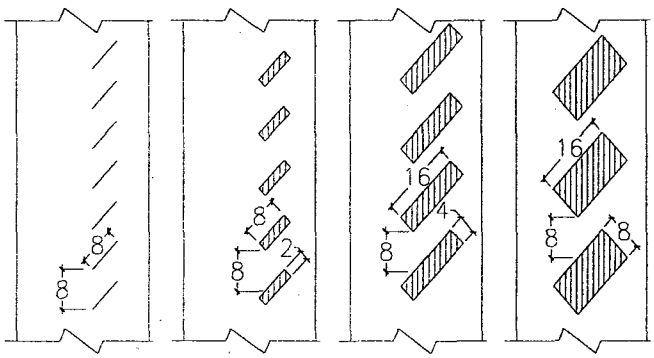

Al -2mm *TM- 8x4cm* *TM- 16x4cm* *TM- 16x8cm*

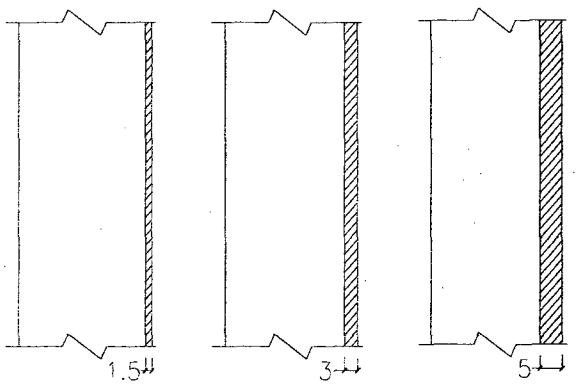

TMi- 1.5cm *TMi- 3cm* *TMi- 5cm*

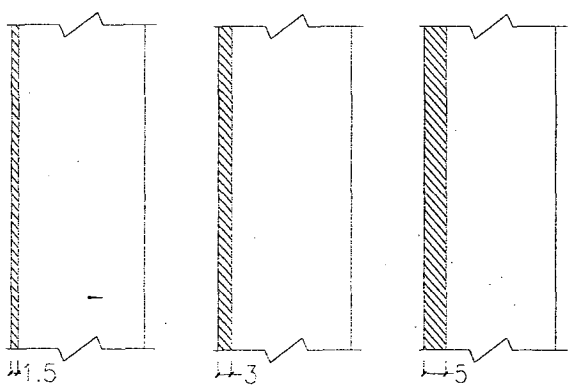

TMo- 1.5cm *TMo- 3cm* *TMo- 5cm*

Figure F.1: Different configurations of the air channel with aluminum and thermal mass blinds. Left side is outdoors. Hatched areas are thermal mass material. All attributions are listed in table F.1.

Slat Name	Slat Type	Slat Width/ Height (cm)	Slat Separation (cm)	Slat Thickness (cm)	Slat Angle (degree)	Total Volume (1/1000 $m^{3)}$	Total surface area exposed to Air Channel (m^2)
MECHANICALLY-VENTILATED DSF							
Al-2mm	Aluminum	8	8	0.2	45	8.19	8.39
TM-8x2cm	Thermal Mass	8	8	2	45	61.44	7.68
TM-16x4cm	Thermal Mass	16	8	4	45	122.88	7.68
TM-16x8cm	Thermal Mass	16	8	8	45	204.8	7.68
TM-1.5cm	Thermal Mass	256	-	1.5	90	61.44	4.096
TM-3cm	Thermal Mass	256	-	3	90	122.88	4.096
TM-5cm	Thermal Mass	256	-	5	90	204.8	4.096
NATURALLY-VENTILATED DSF							
Al- 2mm	Aluminum	8	8	0.2	45	2.88	2.952
TM-8x2cm	Thermal Mass	8	8	2	45	21.6	2.7
TM-16x4cm	Thermal Mass	16	8	4	45	43.2	2.7
TM-16x8cm	Thermal Mass	16	8	8	45	72	2.7
TM-1.5cm	Thermal Mass	160	-	1.5	90	21.6	1.44
TM-3cm	Thermal Mass	160	-	3	90	43.2	1.44
TM-5cm	Thermal Mass	160	-	5	90	72	1.44

Table F.1: Attribution of thermal mass and aluminum slats for naturally-ventilated simulation. All slats are located at a distance of 8cm from each other but they have different thicknesses. TM- 8x2, TM- 16x4 & TM- 16x8 have the same amount of thermal mass as TM- 1.5cm, TM- 3cm & TM- 5cm, respectively. However, the total surface area they exhibit to the air channel is different.

APPENDIX G

ENERGY FLOW COMPONENTS

To have a detailed analysis of different DSF types, heat gains through a DSF was defined as summation of temperature driven heat transfer through the inner side of the interior pane (Q''_i), transmitted solar radiation ($Q''_{Solar\ trans}$) and heat gains induced with ventilation air (Q''_{vent}). This makes it possible to have a detailed comparison between conventional DSF and combined concrete thermal-mass DSF thermal performance.

Writing an energy balance for the interior pane and the whole system to find Q''_i , $Q''_{Solar\ trans}$ and Q''_{vent} respectively,

$$Q''_{vent-in} + Q''_{solar} = Q''_{store} + Q''_{solar\ trans} + Q''_i + Q''_{vent-out} + Q''_o$$

$$Q''_i = Q''_{convection} + Q''_{long-wave\ rad}$$

Q''_{store} is the total thermal energy stored in glazing and the shading device and Q''_{vent} is enthalpic gains of ventilation air by passing through the cavity; their value are calculated from:

$$Q''_{store} = \frac{\dot{m}\, C_p\, (T_{current\ timestep} - T_{previous\ timestep})}{t_{timestep}}$$

$$Q''_{vent} = Q''_{vent-out} - Q''_{vent-in} = \dot{m}\, C_p\, (T_{outlet} - T_{inlet})$$

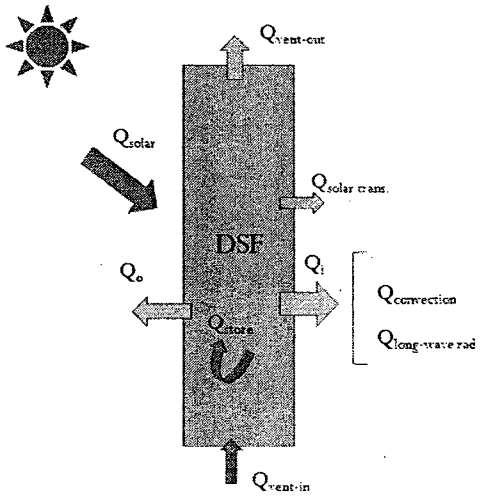

Figure G.1: Energy Balance for DSF. Red arrows present incoming fluxes and yellow arrows outgoing fluxes.

Q''_i is the transmission gains/losses through interior pane of DSF;

Q''_o is the transmission gains/losses through exterior pane of DSF;

$Q''_{solar\ trans.}$ is the amount of short-wave radiation passing directly through interior pane;

Q''_{solar} is the total amount of short-wave radiation incident on exterior pane;

$Q''_{vent\text{-}in}$ is the enthalpy of supply air;

Q''_{solar}, $Q''_{solar\ trans.}$ are measured from test-cell

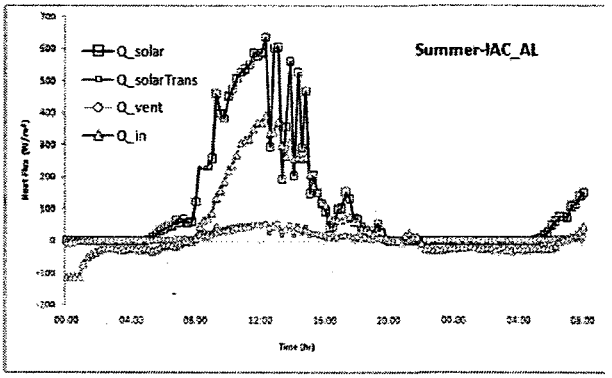
Summer-IAC_AL
Q_solar
Q_solarTrans
Q_vent
Q_in

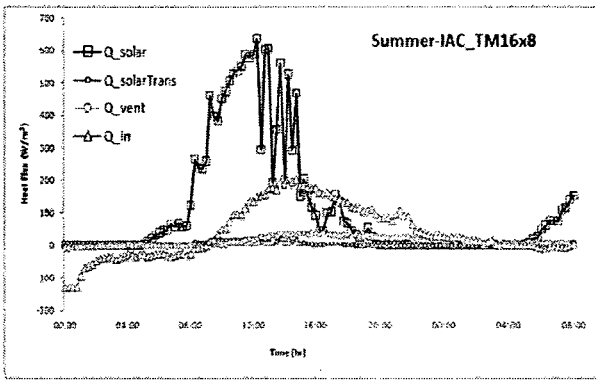
Summer-IAC_TM16x8
Q_solar
Q_solarTrans
Q_vent
Q_in

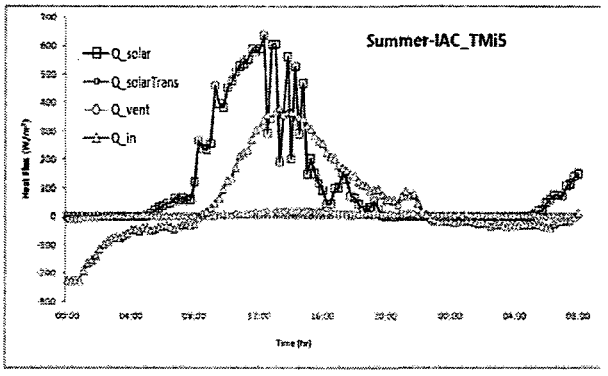
Summer-IAC_TMi5
Q_solar
Q_solarTrans
Q_vent
Q_in

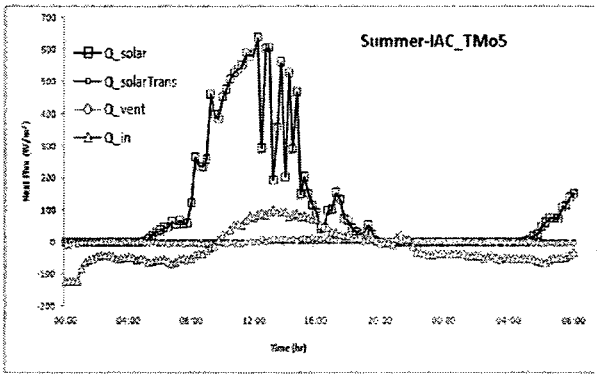
Summer-IAC_TMo5
Q_solar
Q_solarTrans
Q_vent
Q_in

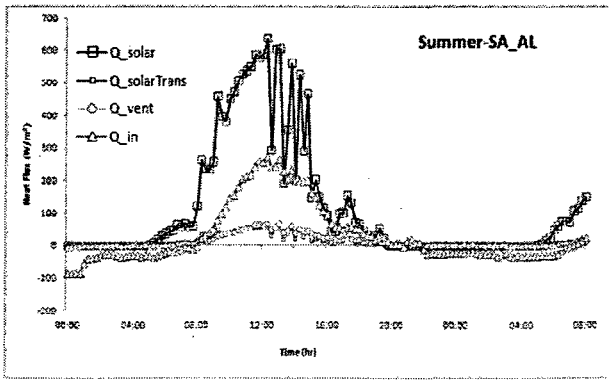
Summer-SA_AL
Q_solar
Q_solarTrans
Q_vent
Q_in

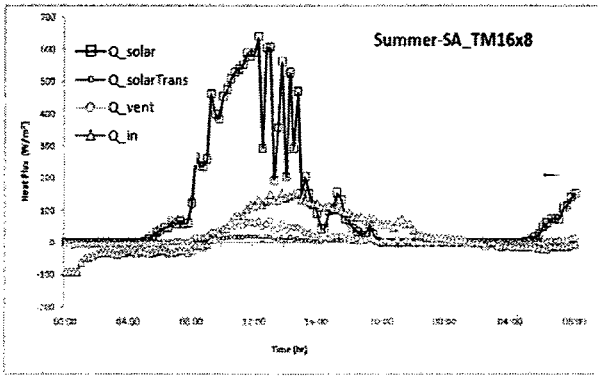
Summer-SA_TM16x8
Q_solar
Q_solarTrans
Q_vent
Q_in

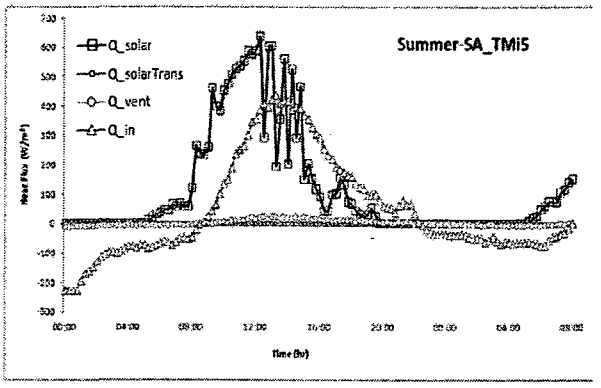

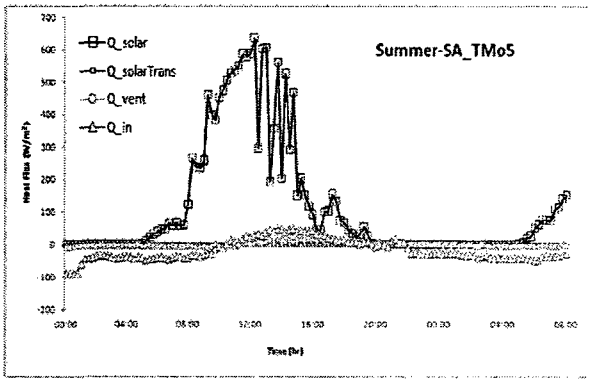

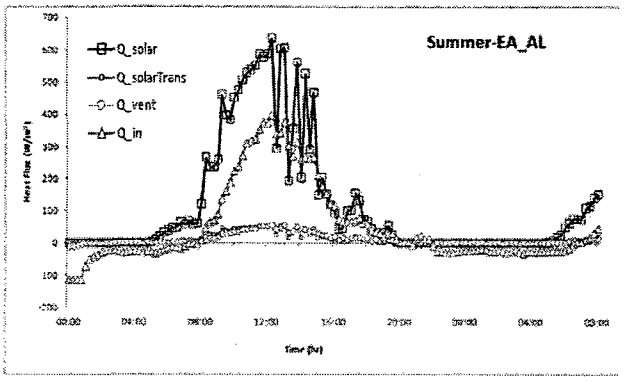

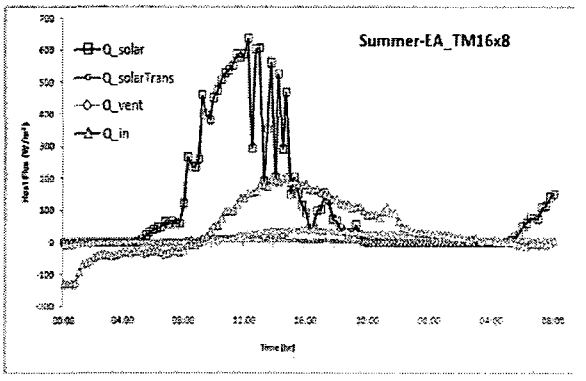

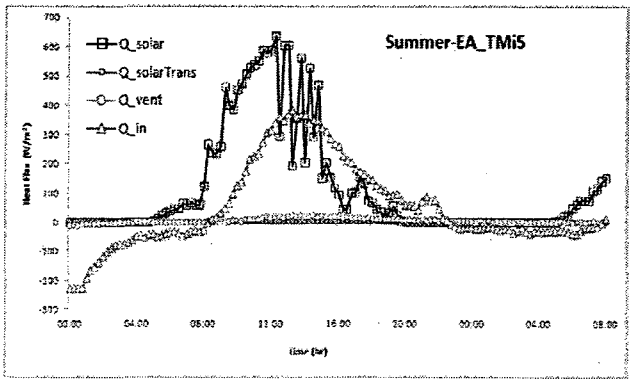

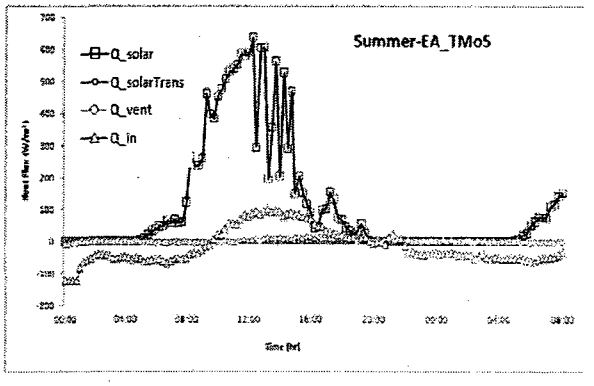

Figure G.2: Comparison of heat fluxes through inner layer of mechanically-ventilated DSF for different airflow paths (IAC, SA & EA) and DSF types (AL, TM, TMi & TMo) in summer

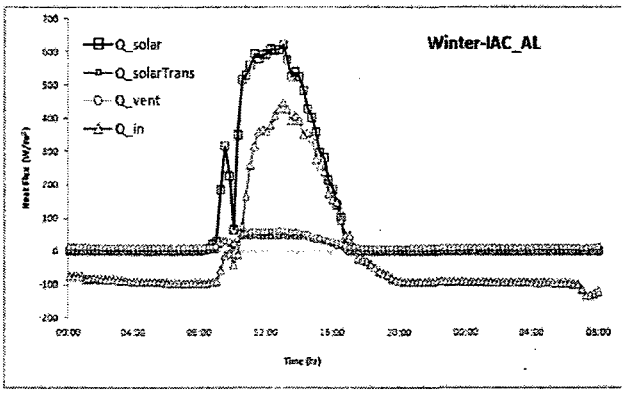
Winter-IAC_AL
Q_solar
Q_solarTrans
Q_vent
Q_in

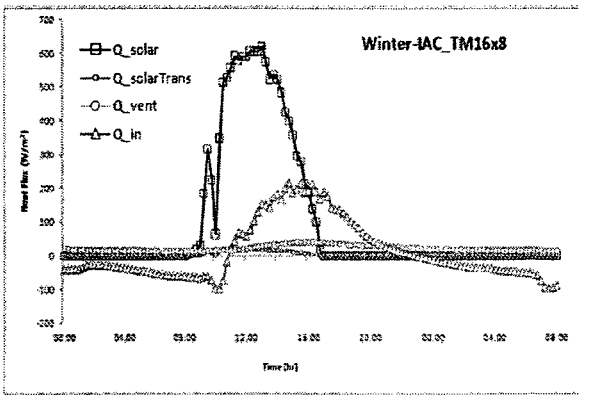
Winter-IAC_TM16x8
Q_solar
Q_solarTrans
Q_vent
Q_in

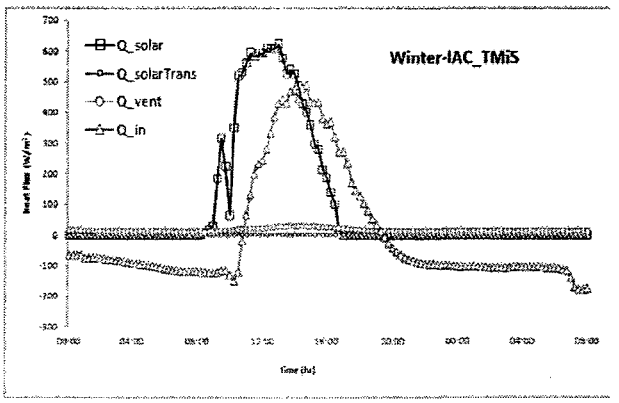
Winter-IAC_TM5
Q_solar
Q_solarTrans
Q_vent
Q_in

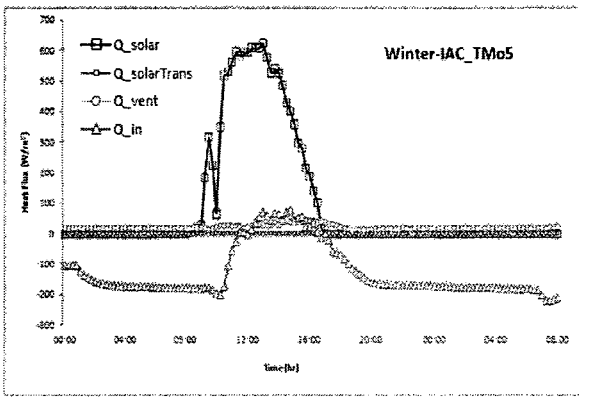
Winter-IAC_TMo5
Q_solar
Q_solarTrans
Q_vent
Q_in

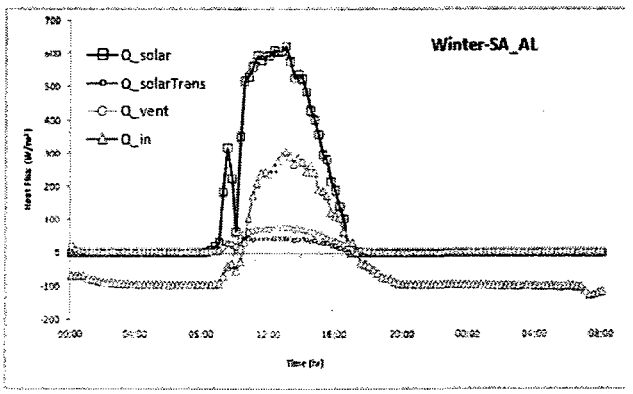
Winter-SA_AL
Q_solar
Q_solarTrans
Q_vent
Q_in

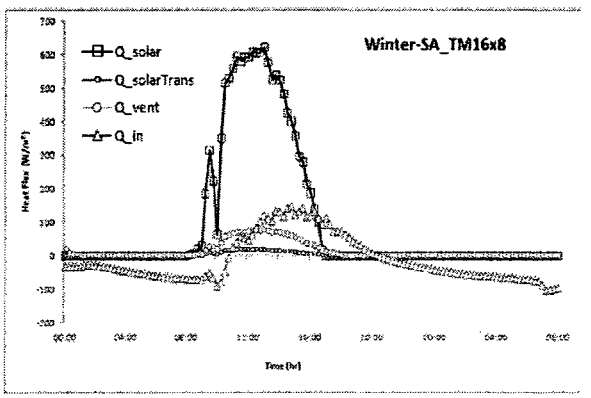
Winter-SA_TM16x8
Q_solar
Q_solarTrans
Q_vent
Q_in

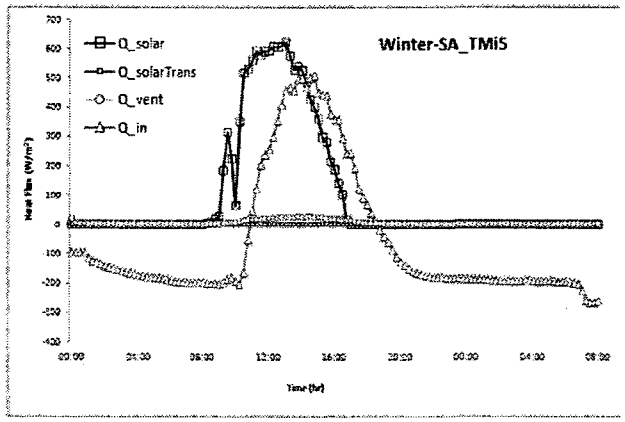

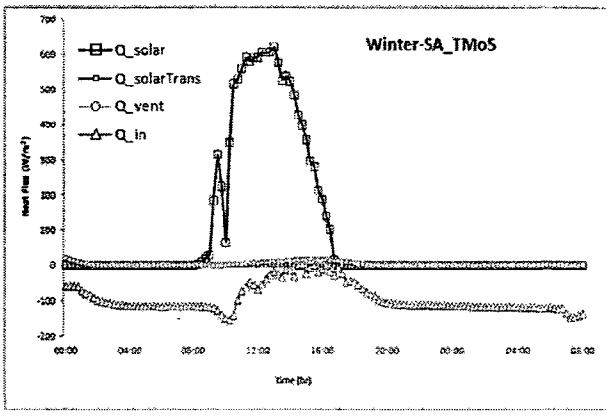

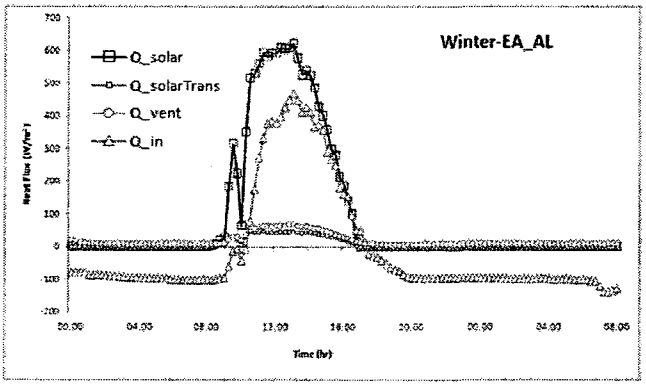

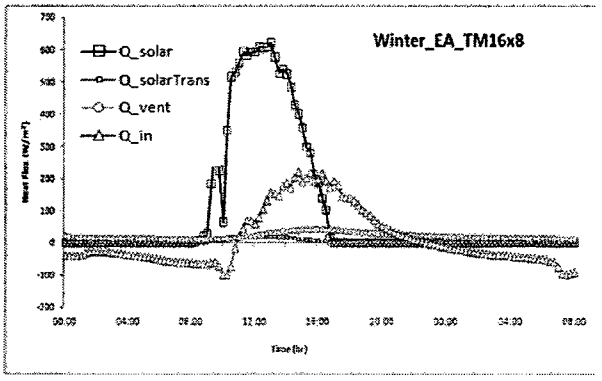

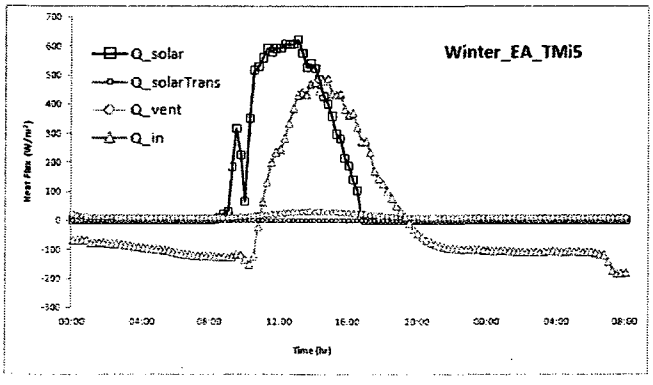

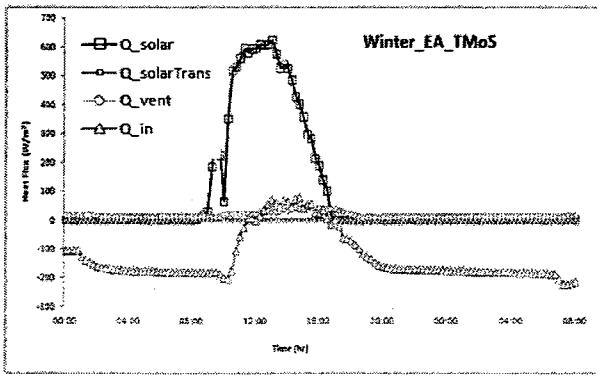

Figure G.3: Comparison of heat fluxes through inner layer of mechanically-ventilated DSF for different airflow paths (IAC, SA & EA) and DSF types (AL, TM, TMi & TMo) in winter

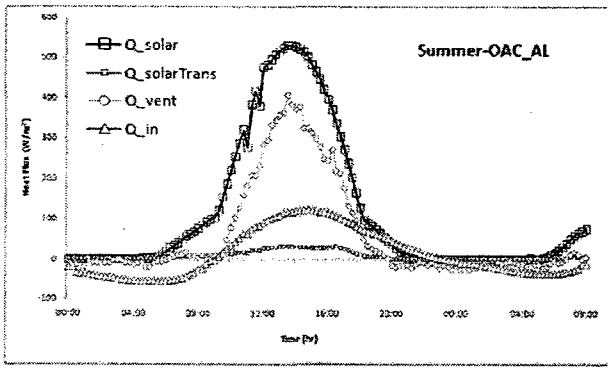

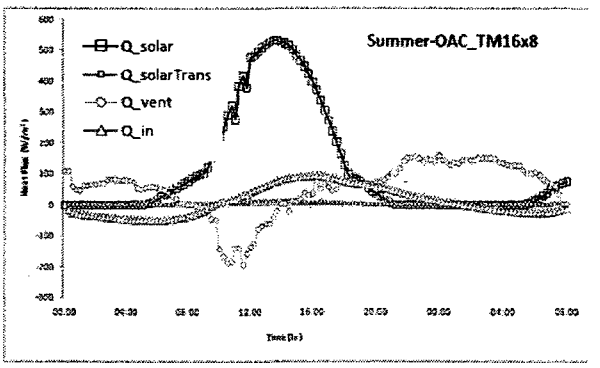

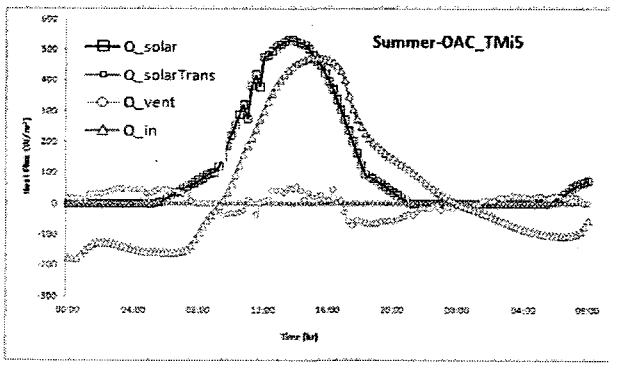

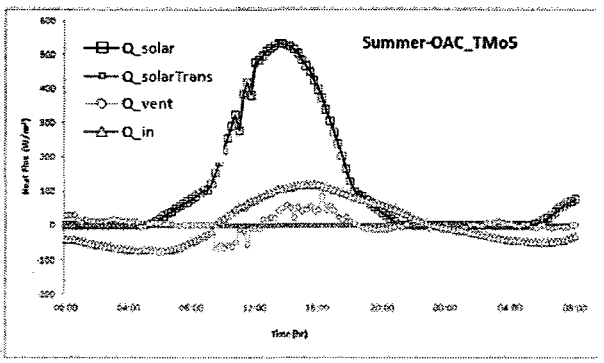

Figure G.4: Comparison of heat fluxes through inner layer of naturally-ventilated DSF for OAC airflow path and different DSF types (AL, TM, TMi & TMo) in summer

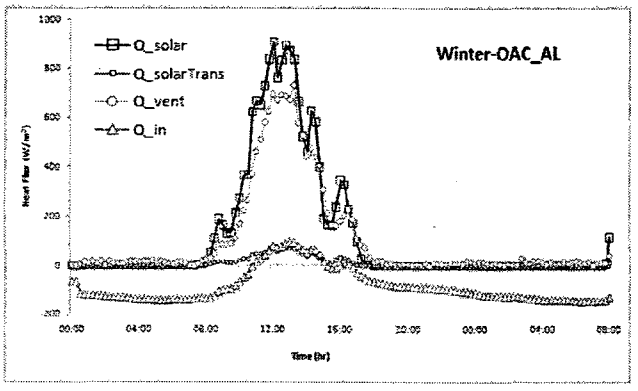

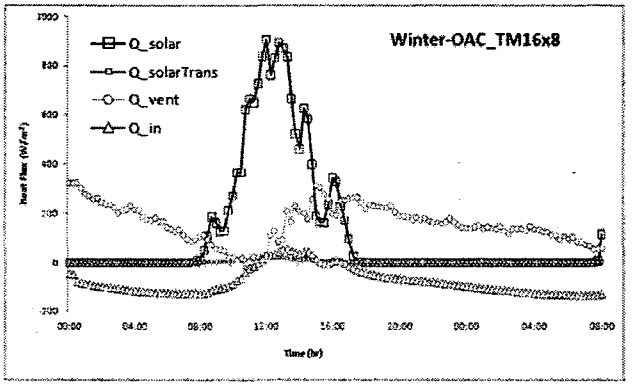

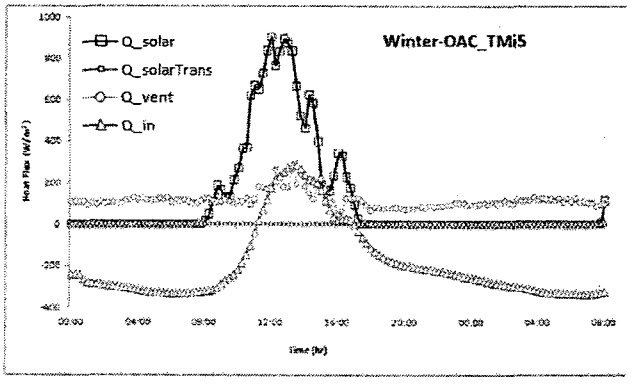

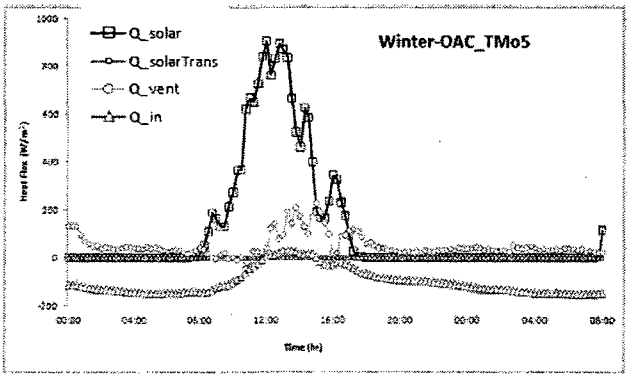

Figure G.5: Comparison of heat fluxes through inner layer of naturally-ventilated DSF for OAC airflow path and different DSF types (AL, TM, TMi & TMo) in winter

APPENDIX H

INFLUENTIAL FACTORS OF DSF THERMAL PERFORMANCE

Based on literature, the influential factors in thermal performance of a conventional naturally ventilated DSF can be grouped as follows:

- **Cavity depth:** the depth is variable from few inches up to 4-5 feet. The temperature decreases slightly in deeper DSFs (Balocco et al. 2004, Gratia et al. 2007, Zollner et al. 2002) ;however, many studies determined that this variable does not have a large effect on the overall thermal performance of the DSF (Pappas et al., 2008). Normally some other factors require a deeper cavity rather than thermal performance requirements, e.g. providing natural ventilation for attached rooms with operable windows, which needs more airflow rate through a deeper cavity, sheltering the shading device and structural elements and maintenance purposes.

- **Cavity width:** DSF exists both with cavities extending the whole width of a building and with cavities stratified into 1–2 m wide sections. The effect of cavity width on airflow has not been studied extensively, but it is likely that structural and aesthetic considerations would largely determine this design decision. It has been suggested, however, that creating narrow cavities will produce shafts that will allow fire and contaminants to propagate more quickly throughout the building (Pappas A. et al., 2008).

- **Cavity height and opening locations:** A taller cavity will produce more temperature difference between inlet and outlet air, a stronger buoyancy force and a greater airflow rate (Manz H., 2004). However, the fire hazard resulting from a large vertical cavity with no divisions might be prohibitive. Also, air contaminants and noise pollution could flow readily from floor to floor. If the cavity is divided at each floor, there are typically air inlets and outlets near the top and bottom of each section. For a full building height cavity, there could be a single bottom inlet and a single top outlet. This configuration creates the strongest buoyancy driven airflow due to the tall cavity height. Alternatively, there could be a number of inlets along the exterior façade with one main outlet at the cavity's peak. This will increase the airflow into the cavity, which is desirable in the case of operable windows (Pappas A. et al., 2008).

- **Opening ratio:** The cavity openings can be either quite simple and open to wind or complex with controlled blind slats and wind shields meant to reduce the effect of wind pressure on airflow through the cavity. If no wind shields exist, the airflow within the cavity will often be driven by wind pressure, forcing the air to flow predominantly in the downward direction (Pappas A. et al., 2008). A greater opening ratio can result in mass flow rate increase if wind effect and stack effect are assisting.

- **Cavity material:** Depending on the amount of transparency needed the interior skin of a DSF can be fully or partially made of glass. Temperature is always lower

in a DSF with a higher proportion of glazed surfaces in the interior façade than opaque walls due to less solar absorption (Gratia E. et al., 2007). Moreover the solar properties of glazing (absorptance, transmittance and reflectance) and applied coatings are influential. In some cases the total heat transferred into the building is more than five times the heat into the building with a different set of glass (Perez-Grande I. et al,, 2005). Not only materials affect thermal performance, but also it was shown that alterations to the sequence of a given set of layers in a DSF can easily change the total solar energy transmittance by a factor greater than 5 (Manz H., 2004).

- **Shading device:** The color and position of the shading device in the air cavity can save cooling consumption on a summer day. This saving can reach up almost to 14% and 3.5% respectively for optimum position and color choice (Gratia E. et al., 2006). Artmann N. et al. (2004) reported that the interior façade temperature increases and airflow rate decreases at a lower tilt angle. Regarding the effect of the position of the shading device, they concluded that for positions near one of the glazings high temperatures occur in the smaller cavity with glazing, while the air on the opposite side of the venetian blind shows a thermal layering with relatively cool temperature near inlet and higher temperature close to outlet.

- **Outdoor climate:** The configuration of a DSF and its control strategy are very influential on saving that can be obtained from climate to climate. Zerefos (2007) compares the heating and cooling loads between a double skin façade and a single

skin façade in different and contrasting climates. In sunny climates such as the Mediterranean due to U-value improvement and SHGC reduction achieved by DSF, double skin façades are considered to be preferable during the cooling season (29%-35% annual saving in Mediterranean). In fact, the more sunshine days the site has the less energy consumption DSF will have compared to a single skin façade. In contrast, in cold continental climates, such as Moscow, as well as temperatures, such as London, the difference in performance of double skin façade and single skin façade is generally reduced, especially during the heating season. DSF results in g-value reduction, which is undesirable in heating season. However, the U-value improvement and preheating effect outweigh and contribute to some saving. In Moscow this saving is 8.3% annually. Another study by Hamza N. (2008) concluded from simulation study that a reflective DSF can achieve better energy savings than a single skin with reflective glazing in hot climate.